


12-2015

# Prediction of Rupture in Abdominal Aortic Aneurysm

Qusay Alfaori

*University of Arkansas, Fayetteville*

Follow this and additional works at: <http://scholarworks.uark.edu/etd>

 Part of the [Biomechanics and Biotransport Commons](#), and the [Biomedical Devices and Instrumentation Commons](#)

---

## Recommended Citation

Alfaori, Qusay, "Prediction of Rupture in Abdominal Aortic Aneurysm" (2015). *Theses and Dissertations*. 2039.  
<http://scholarworks.uark.edu/etd/2039>

This Dissertation is brought to you for free and open access by ScholarWorks@UARK. It has been accepted for inclusion in Theses and Dissertations by an authorized administrator of ScholarWorks@UARK. For more information, please contact [scholar@uark.edu](mailto:scholar@uark.edu), [ccmiddle@uark.edu](mailto:ccmiddle@uark.edu).

Prediction of Rupture in Abdominal Aortic Aneurysm

A dissertation submitted in partial fulfillment  
of the requirements for the degree of  
Doctor of Philosophy in Engineering with a Concentration in Biomedical Engineering

by

Qusay Alfaori  
University of Arkansas  
Bachelor of Science in Biomedical Engineering, 2014  
University of Arkansas  
Master of Science in Biomedical Engineering, 2015

August 2017  
University of Arkansas

This dissertation is approved for recommendation to the Graduate Council.

---

Dr. Morten Jensen  
Dissertation Director

---

Dr. Ashok Saxena  
Dissertation Co-Director

---

Dr. Hanna K Jensen  
Committee Member

---

Dr. Woodrow Shew  
Committee Member

---

Dr. Robyn Goforth  
Committee Member

## Abstract

Studying the development of abdominal aortic aneurysm (AAA) through quantification of its growth kinetics and rupture criteria is important to decrease the risk of this life-threatening event. Uniaxial and biaxial testing of healthy and time-dependent Type-I collagen degraded aortic specimens from pigs was performed. Stress-strain suitable mathematical models describing the behavior of abdominal aortic tissue were utilized to derive specific tissue properties and parameters. Reduction in Type-I collagen fraction was observed using picosirius red staining method, bright field microscopy, and MATLAB. Finite Element Modeling (FEM) of healthy and time-dependent Type-I collagen degraded abdominal aortas were performed using ABAQUS finite element software. The experimental tissue parameters were inputted in ABAQUS as tissue material properties. The focus was on finding the values of ultimate tensile strength ( $\sigma_{\max}$ ), maximum strain at rupture ( $\epsilon_{\max}$ ), elastic modulus (E), and the critical strain ( $\epsilon_c$ ), which is identified as the point beyond which high rupture risk is present. These properties vary significantly between healthy tissue and time-dependent Type-I collagen degraded tissue. Significant differences were found in the biomechanical behavior of aortic tissue due to time-dependent Type-I collagen degradation. Tissue compliance increased; however, tissue strength decreased. Also, E,  $\sigma_{\max}$ ,  $\epsilon_{\max}$ , and  $\epsilon_c$  values were significantly higher for the healthy tissue group than for time-dependent Type-I collagen degraded tissue groups. Picosirius red images showed fragmented Type-I collagen fibers, and the observation was linked to the change in biomechanical behavior of the specimens. FEM of healthy and time-dependent Type-I collagen degradation models mimicked “aneurysmal” growth from an initial stage, a finding which will contribute to better assessment of patients’ specific AAA cases. In conclusion, the data indicate that Type-I collagen is important in maintaining abdominal aortic tissue’s structural integrity, and the growth kinetics and rupture risk

of AAA increase significantly in the time-dependent Type-I collagen degraded tissue. Thus, quantification of Type-I collagen, the most abundant collagen type in the tissue, along with the quantification of other types of collagen in the tissue, should be included as a rupture criteria for monitoring the growth in AAA and predicating rupture.

## **Acknowledgement**

I would like to express my appreciation and gratefulness to the following people, whose presence, support, guidance, encouragement, and advice were invaluable in this project.

My co-advisor Professor Ashok Saxena, a “thank you” is not enough to describe how grateful I am for your continuous motivation, encouragement, support, and guidance throughout my research. Your diligence and patience with guiding me through the ups and downs of this research has been much appreciated.

My co-advisor Dr. Morten Jensen, thank you for the patient guidance, enthusiastic encouragement and useful critiques of this research work. Your willingness to give time, knowledge, and effort so generously has been very much appreciated.

Dr. Hanna Jensen, thank you for your creativity, knowledge, and valuable and constructive suggestions during this research work.

Dr. Woodrow Shew, thank you for your knowledge, talent, words of encouragement, and motivation. You have always been so supportive and helpful.

Dr. Robyn Goforth, thank you for your essential help and invaluable advice in this research. I appreciate the knowledge, time, and effort you spent in explaining some of the biochemistry concepts needed for this work.

I would also like to extend my thanks to the faculty and staff of the Biomedical Engineering department for their help in offering me the resources needed in this work.

Finally, I wish to thank my parents and friends for their support and encouragement throughout my study.

## **Dedication**

*To my father and mother, thank you for all your love and support.  
Without you, I would not be where I am today.*

## Table of Contents

Chapter 1 - Introduction.....	Page 1
1.1. Background.....	Page 2
1.2. The Anatomy and Structure of the Aorta.....	Page 7
1.3. Rationale.....	Page 10
Chapter 2 - Literature Review.....	Page 12
2.1. Pathophysiology.....	Page 13
2.2. Imaging Techniques.....	Page 15
2.3. Rupture Risk Factors and Analysis.....	Page 17
2.4. Differences in Rupture Risk for Males vs. Females.....	Page 21
2.5. Geometry of Vessel Wall and Role of Intraluminal Thrombus.....	Page 24
2.6. Arterial Pressure and Distensibility.....	Page 42
2.7. Extracellular Matrix Protein Degradation in Abdominal Aortic Aneurysms.....	Page 47
2.8. Collagen Subtypes and Elastin.....	Page 48
2.9. Mechanical Testing.....	Page 50
2.10. Computational Methods.....	Page 53
2.11. Implications.....	Page 69
Chapter 3 - Hypothesis, Objectives, and Specific Aims.....	Page 71
3.1. Goals and Objectives.....	Page 72
3.2. Hypothesis.....	Page 72
3.3. Specific Aims.....	Page 73
Chapter 4 - Mechanical Testing and Constitutive Model.....	Page 75
4.1. Methods.....	Page 76
4.2. Strain Rate Constitutive Model.....	Page 77

4.3. Fung Constitutive Model.....	Page 78
4.4. Uniaxial Tests.....	Page 79
4.5. Biaxial Tests.....	Page 87
4.6. Discussion.....	Page 92
Chapter 5 - Imaging and Collagen Quantification.....	Page 101
5.1. Methods.....	Page 102
5.2. Collagen Microstructural Imaging.....	Page 104
5.3. Collagen Fibers Fraction.....	Page 105
5.4. Discussion.....	Page 106
Chapter 6 - Finite Element Modeling.....	Page 109
6.1. Methods.....	Page 110
6.2. Healthy Abdominal Aortic Model.....	Page 112
6.3. Time-Dependent Collagen Degradation Aortic Model.....	Page 114
6.4. Discussion.....	Page 116
Chapter 7 - Limitations.....	Page 121
Chapter 8 - Conclusion.....	Page 124
References.....	Page 128



## **List of Acronyms**

AAA: Abdominal Aortic Aneurysm

AA: Abdominal Aorta

ECM: Extracellular Matrix

CT: Computed Tomography

ILT: Intraluminal Thrombus

FEA: Finite Element Analysis

FEM: Finite Element Method

EVAR: Endovascular Aneurysm Repair

MMPs: Matrix Metalloproteinases

MRI: Magnetic Resonance Imaging

18-FDG PET: 18-Fluorodeoxyglucose Positron Emission Tomography

SUV: Standard Uptake Value

PWS: Peak Wall Stress

PWRI: Peak Wall Rupture Index

TI: Tortuosity Index

PWRR: Peak Wall Rupture Risk

CC: Coagulation Cascade

P3NP: Type-III Procollagen Aminoterminal Propeptides

RRI: Rupture Risk Index

RPI: Rupture Potential Index

MAP: Mean Arterial Pressure

CFD: Computational Fluid Dynamics

PSR: Picrosirius Red

PBS: Phosphate Buffered Saline

OCT: Optical Cutting Temperature

PH1: Phase 1

## List of Tables

Table 1.....	Page 6
Table 2.....	Page 20
Table 3.....	Page 23
Table 4.....	Page 84
Table 5.....	Page 84
Table 6.....	Page 89
Table 7.....	Page 95
Table 8.....	Page 106

## List of Figures

Figure 1.....	Page 2
Figure 2.....	Page 4
Figure 3.....	Page 8
Figure 4.....	Page 9
Figure 5.....	Page 10
Figure 6.....	Page 14
Figure 7.....	Page 16
Figure 8.....	Page 19
Figure 9.....	Page 20
Figure 10.....	Page 22
Figure 11.....	Page 25
Figure 12.....	Page 26
Figure 13.....	Page 27
Figure 14.....	Page 28
Figure 15.....	Page 29
Figure 16.....	Page 29
Figure 17.....	Page 30
Figure 18.....	Page 30
Figure 19.....	Page 32
Figure 20.....	Page 33
Figure 21.....	Page 33
Figure 22.....	Page 34
Figure 23.....	Page 35
Figure 24.....	Page 36
Figure 25.....	Page 38
Figure 26.....	Page 40
Figure 27.....	Page 41

Figure 28.....	Page 43
Figure 29.....	Page 43
Figure 30.....	Page 44
Figure 31.....	Page 46
Figure 32.....	Page 48
Figure 33.....	Page 51
Figure 34.....	Page 52
Figure 35.....	Page 54
Figure 36.....	Page 55
Figure 37.....	Page 57
Figure 38.....	Page 58
Figure 39.....	Page 59
Figure 40.....	Page 60
Figure 41.....	Page 60
Figure 42.....	Page 62
Figure 43.....	Page 63
Figure 44.....	Page 64
Figure 45.....	Page 65
Figure 46.....	Page 66
Figure 47.....	Page 67
Figure 48.....	Page 68
Figure 49.....	Page 74
Figure 50.....	Page 77
Figure 51.....	Page 79
Figure 52.....	Page 80
Figure 53.....	Page 80
Figure 54.....	Page 81
Figure 55.....	Page 82

Figure 56.....	Page 83
Figure 57.....	Page 83
Figure 58.....	Page 85
Figure 59.....	Page 85
Figure 60.....	Page 86
Figure 61.....	Page 86
Figure 62.....	Page 87
Figure 63.....	Page 88
Figure 64.....	Page 88
Figure 65.....	Page 89
Figure 66.....	Page 90
Figure 67.....	Page 90
Figure 68.....	Page 91
Figure 69.....	Page 91
Figure 70.....	Page 92
Figure 71.....	Page 99
Figure 72.....	Page 102
Figure 73.....	Page 103
Figure 74.....	Page 104
Figure 75.....	Page 105
Figure 76.....	Page 110
Figure 77.....	Page 111
Figure 78.....	Page 112
Figure 79.....	Page 112
Figure 80.....	Page 113
Figure 81.....	Page 113
Figure 82.....	Page 114

Figure 83.....Page 115  
Figure 84.....Page 116

**Chapter 1**  
**Introduction**

## 1.1. Background

The leading cause of death in the Western World is cardiovascular disease [18, 22-24]. In the US alone, about 81 million people suffer from at least one form of cardiovascular disease, leading to approximately 900,000 deaths annually [24]. In Europe, 40% of deaths among under 75-year-old population are from cardiovascular diseases [3, 23-25]. Aneurysms are a type of cardiovascular disease that are characterized by atypical expansions in blood vessels.

Abdominal Aortic Aneurysm (AAA) is an abnormal dilatation of the aorta, usually occurring in the infra-renal section, as shown in Figure 1 [24, 26]. Infra-renal means under the branches of the renal arteries. A patient is said to have Abdominal Aortic Aneurysm (AAA) when the abdominal aortic diameter is increased by 50% of the healthy diameter [27]. Every year, 500,000 new patients are diagnosed with AAA throughout the world, 150,000 in the United States [3]. During routine physical examination, about 30% of asymptomatic AAAs are discovered [28].

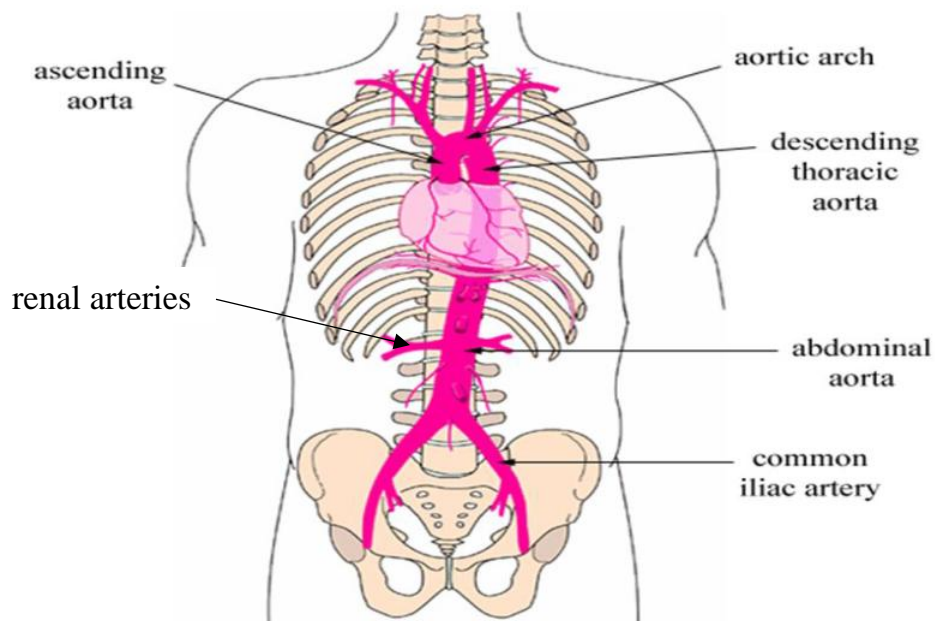


*Figure 1 The aorta and its four main sections. Adapted from [http://www.cts.usc.edu/zglossary-aorta.html]*



AAA is present in approximately 2-4% of the elderly population, ages 60 years and above. If AAA is left untreated, it will continue to expand until rupture [3, 18]. When AAA rupture occurs, 30-50% of patients die before arriving at a hospital, total rupture mortality is >90%, and even in patients for whom surgical treatment is performed, mortality remains at a high rate of 50-70% [24]. Every year in the US, approximately 15,000-20,000 people die from AAA, the 10<sup>th</sup> leading cause of death among men 55 years of age and older [3]. In 2011, 45,000 AAA repair procedures were carried out in the US, and 1400 deaths resulted from such procedures [28]. AAA is the 13<sup>th</sup> most common cause of death in the US with a mortality rate of 90% upon rupture [12, 16, 18].

Main AAA risk factors include atherosclerosis, high blood pressure, smoking, and genetics. Smoking induces high blood pressure and atherosclerosis, which results in stiffening of arteries in the long run [2, 5, 26, 29]. AAA expansion can also be influenced by many inflammatory factors, such as shortened elastin half-life due to an increase in local production of matrix-degrading enzymes, degradation of collagen, apoptosis of smooth muscle cells, and adherence of mural thrombi.

Collagen and elastin are the main structural proteins that make up the extracellular matrix (ECM). Collagen provides the aortic wall with strength, while elastin allows it to return to original shape after deformation. Thus, elastolysis is thought to cause focal widening of an AAA, and collagen failure is thought to cause AAA rupture [16, 26].

AAA formation is thought to be due to the degeneration of the extracellular matrix and is associated with a decrease in wall strength [16]. The aortic wall becomes weakened when elastin and collagen are degraded and will eventually rupture [20, 26, 30]. When wall stress exceeds wall strength at a certain site in the wall of the aneurysm, rupture will occur [16, 20, 31].

AAA is diagnosed with the aid of medical imaging techniques such as ultrasonography, computed tomography (CT) scanning, or MRI scanning. Due to technological advancements in medical imaging, AAA diagnosis is improving worldwide, especially in the west. However, AAA is often asymptomatic, which makes it difficult for the patients to seek help and treatment.

Although 60-year-old men are prime candidates for AAA screening, individuals with family history are at a higher risk of developing AAA at an earlier age. Thus, they are recommended for AAA screening by the age of 50 [24]. Figure 2 below shows a healthy abdominal aorta and an aneurysmal aorta.

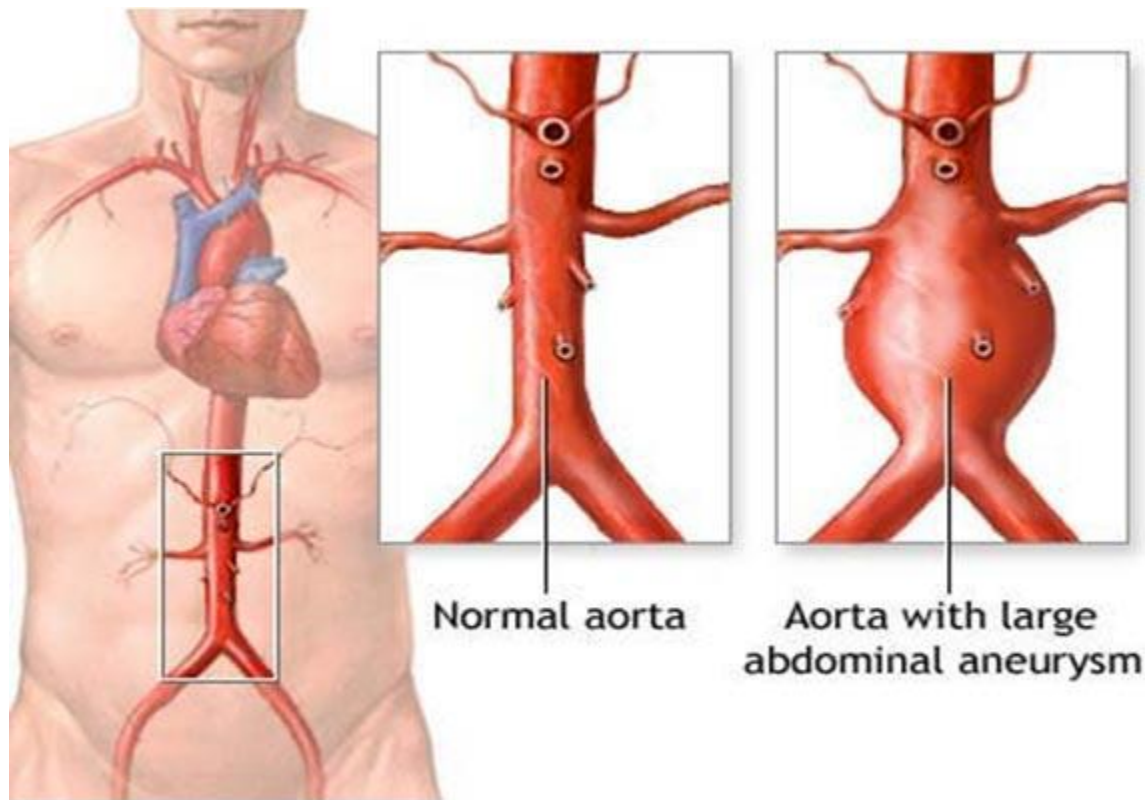


*Figure 2 healthy aorta (on the left) and an aneurysmal aorta (on the right)*  
[[www.nlm.nih.gov](http://www.nlm.nih.gov)]

Currently, the likelihood of rupture is estimated based on the maximum diameter of the aneurysm [11]. When the maximum diameter is 5.5 cm or greater, risk to rupture is thought to be significantly high and will require repair [29]. A healthy aorta has a diameter of 2.5-3 cm and can retain the original shape after deformation. However, aneurysmal aortas have diameters greater than 3 cm and fail to retain their original shape when deformed. The expansion rate of aneurysms is usually 0.2-0.4 cm per year, but, if the expansion rate of the aneurysm is greater than 1 cm per year, physician intervention is highly recommended [10].

The maximum diameter criterion has been proven to be suboptimal by multiple autopsy studies. One study reported that 12.8% of AAAs having a diameter of less than 5cm ruptured, while only 40% of AAAs with a diameter greater than 5cm went on to rupture [16]. The 5.5cm criterion--based on the Law of Laplace--which states that for a perfect cylinder or sphere, as radius increases (with or without an increase in pressure), tension in the aortic wall increases. However, the geometries of abdominal aortas (AA) are much more complex than a simple cylinder and display a high level of tortuosity. This tortuosity causes complex stress distributions that vary throughout the length of the AA and could result in higher or lower stresses at different points along the AAA than those predicted by the Law of Laplace [16]. Also, geometries vary from patient to patient, furthering the need for a new predictor value other than maximal diameter [16]. Table 1 shows the percentage of ruptured aortas based on maximum diameter [18].

*Table 1 shows the relationship of size to rupture in 473 nonresected AAA and percent of ruptured aneurysms for different maximum diameter sizes of AAA [18].*

<b>SIZE (CM)</b>	<b>N RUPTURED</b>	<b>N RUPTURED</b>	<b>TOTAL</b>	<b>% RUPTURED</b>
<b>≤ 5.0</b>	34	231	265	12.8
<b>&gt; 5.0</b>	78	116	194	40.0
<b>NO SIZE RECORDED</b>	6	8	14	43.0
<b>TOTAL</b>	118	355	473	24.9

Detection of AAA and an assessment of rupture risk of the AAA are both important because the patient's life is potentially at risk. Even though some patients have aneurysms that are slightly larger than the normal aorta in diameter, frequent monitoring of such cases is highly recommended in order to assess growth of the aneurysm and to treat it in time to avoid catastrophic rupture.

Over the past 15 years, other factors considered relevant to rupture risk assessment are wall stress distribution, wall strength, and formation of intraluminal thrombus (ILT) on the intima layer of the AAA wall [8, 10, 22, 24]. The ILT forms due to fluid dynamics-chemical reaction coupled flow. Engineering tools such as finite element analysis (FEA) are now frequently used to model hypothetical and patient-specific constructed aneurysms. Based on work done using FEA, factors such as expansion rate, degree of symmetry, and geometrical parameters of AAA can be used as additional factors for assessing potential risk of rupture [22, 24].

In the case of AAA with significant rupture risk, repair is imminent. If the patient undergoes a repair, there are two primary options: open surgery and endovascular aneurysm repair (EVAR). In an open surgery, the surgeon cuts through the abdomen and places a stent in the aneurysm to bypass the blood flow [12, 22]. Open repair of an AAA is a costly, invasive procedure that requires an extended hospital stay and is associated with prolonged postoperative pain as well as the risk of various complications [16, 24].

Further, many elderly patients with AAA are at higher risk when undergoing surgery due to comorbid conditions [16, 24]. For these reasons, an accurate means of predicting rupture risk would enhance the clinical effectiveness of AAA surgery [16, 18, 22, 24]. In EVAR, a guided catheter is inserted through the iliac or femoral arteries and is used to guide the stent to the site of the aneurysm. EVAR is a non-invasive procedure that dramatically reduces the risk of infection and, consequently, has a much lower post-surgery mortality rate. Therefore, EVAR is a highly preferred option for AAA treatment [12, 22]. The development of a new prognostic tool is essential in treatment of AAA patients and will have a positive impact on many lives.

## **1.2. The Anatomy and Structure of the Aorta**

The aorta is the largest blood vessel (artery) in the body. It starts from the left ventricle of the heart and extends to the abdomen, where it branches to the femoral and iliac arteries, also known as the bifurcation fork, as shown in Figure 1 above. The aorta is divided into four sections as follows: ascending aorta, aortic arch, thoracic aorta, and abdominal aorta. The aorta is composed of three main layers, from inside to outside, the intima, the media, and the adventitia. The anatomy of the aortic wall is shown in Figure 3.

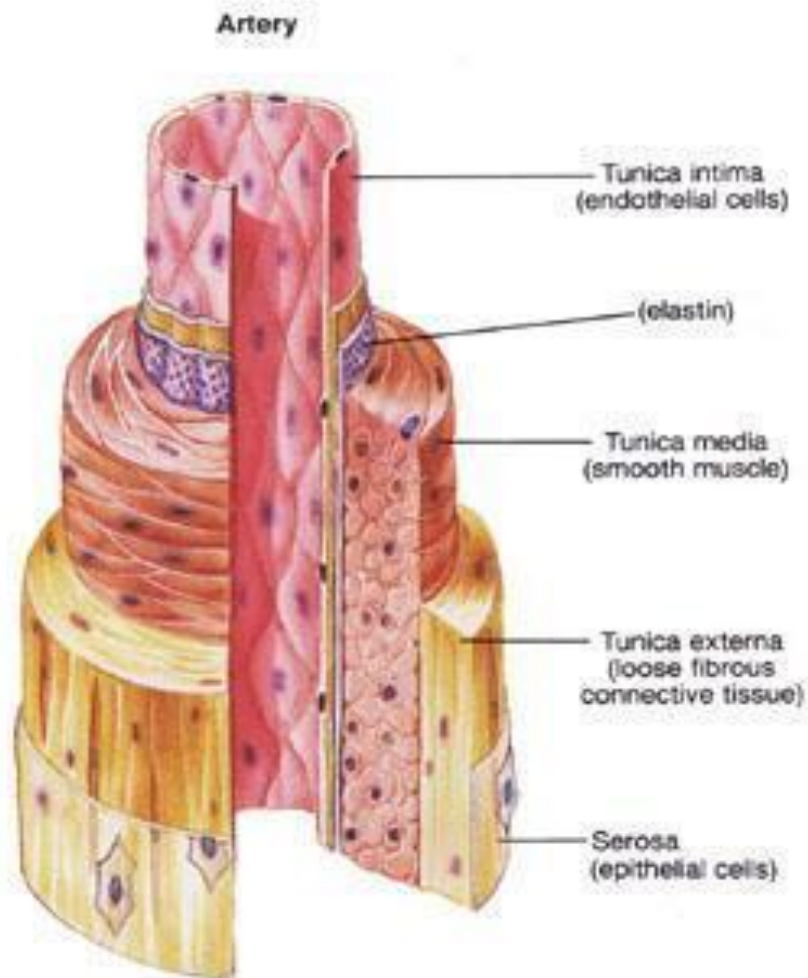


*Figure 3 The three main layers of the aortic wall are intima, media, and adventitia (externa and Serosa) [<http://www.stiffarteries.com/arterial-stiffness.php>].*

As one descends down the aorta, a gradient of tissue mechanical properties exists that depends on the content of smooth muscle and two main proteins that make up some of the building blocks and the microstructure of the aortic wall. The two main proteins of interest are collagen and elastin. Collagen gives the aortic wall strength and elastin the ability to recoil [22, 26, 31]. Elastin is mainly responsible for the elasticity of the tissue, which is defined as the ability to return to its original shape after being deformed [22, 31]. Changes in elastin and collagen content will result in alterations to the aortic wall properties.

The development of AAA is complex and not fully understood, but it is known that degradation of the aortic wall causes an aneurysm to form due to changes in wall properties, which in turn causes the aortic wall to become weaker [22, 32]. Wall degradation is a biological process, which can be affected by many factors such as hypertension, atherosclerosis, smoking, chronic obstruction pulmonary disease, gender, age, and family genetic history [3]. Smoking in particular is considered harmful because it directly weakens the walls of the aorta by worsening atherosclerosis and hypertension [22, 32].

According to Raghavan et al. the stress-strain relationship of aortic tissue behaves as a non-linear exponential curve [20]. In the non-linear behavior, elastin is continuously involved in supporting the tissue, and collagen fibers start to support the tissue as higher stress is applied, as shown in Figure 4 [20, 22]. The collagen fiber structure in the aortic tissue is a complex matrix, as shown in Figure 5.

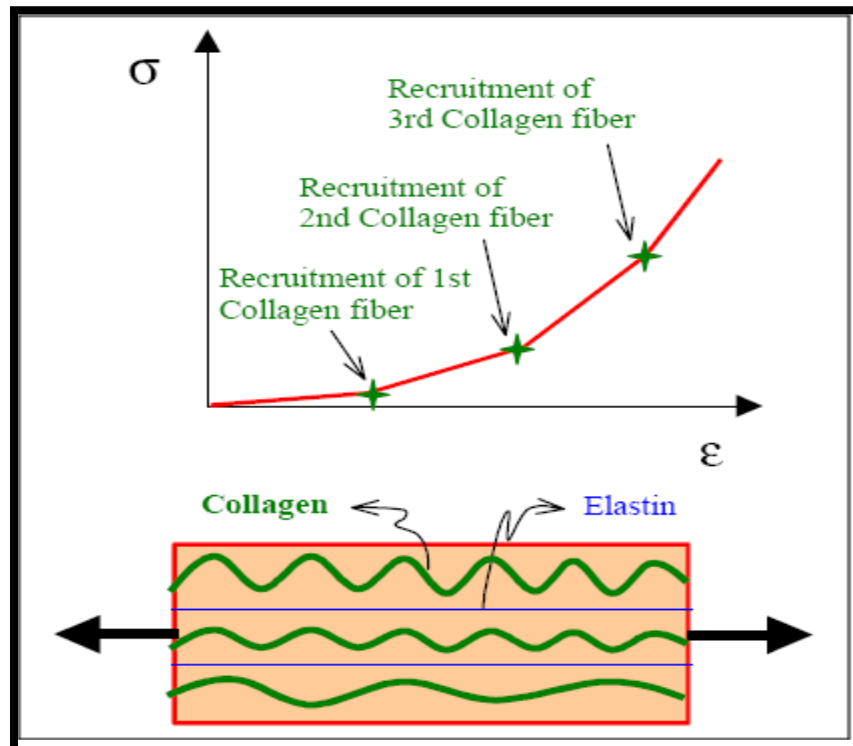
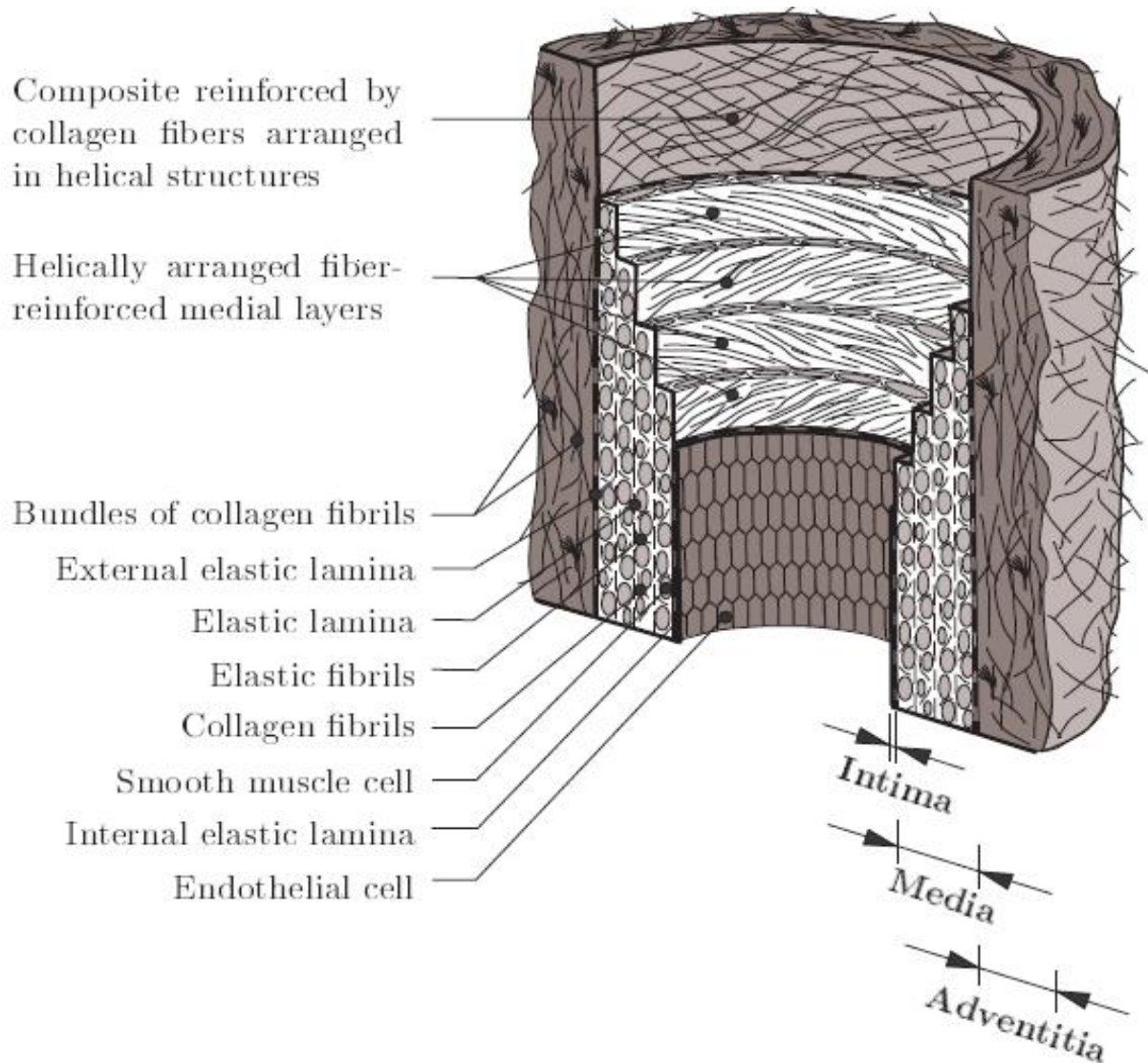


Figure 4 Non-linear stress strain behavior of aortic tissue and the role of elastin and collagen in supporting the stress [1].



*Figure 5 The three main layers of the aortic wall and the composition within each layer. Adapted from Holzapfel et al. 2000.*

### 1.3. Rationale

The Cardiovascular Biomechanics Laboratory at the University of Arkansas performed biomechanical tests on porcine aortic tissue samples in order to study their stress-strain properties. Porcine aortas have similar properties to human aortas [5]. Control tissue from animals will have healthy content of elastin and collagen. Experimental tissue obtained from animals requires enzymatic degradation to closely mimic aneurysmal conditions in the human body [5, 10, 20].



Enzymatic degradation is performed with the use of elastases and collagenases that degrade elastin and collagen proteins in the tissue. The use of degradation enzymes decreases the elastic modulus (stiffness) of the tissue [10, 20, 26]. Elastin and collagen degradation hinders normal functionality of aortic tissue [10, 20]. Since aortic tissues operates under high blood pressures, it is essential they maintain their biomechanical characteristics for optimal function.

Stress-strain uniaxial and biaxial tests were performed on healthy and Type-I collagen degraded specimens under physiological conditions to observe and quantify the change in tissue elasticity. The tissue will involve an innovative approach to using a fundamental strain model.

Type-I collagen fibers were observed using microscopic imaging techniques in order to relate changes in the biomechanical properties to physical microstructural properties. Finite element modeling (FEM) software mimicked the growth of an aneurysm in a Type-I collagen time-dependent degradation aortic model based on changes in tissue properties obtained from the uniaxial and biaxial experimental results, specifically, tissue elasticity. The goal is to relate changes in tissue properties with a time factor that will be modeled through the use of FEM software [4, 18].

**Chapter 2**  
**Literature Review**

## 2.1. Pathophysiology and Risk Factors

Once the aortic wall degrades to a critical point and is not able to withstand pressure applied by the luminal blood flow, it is at a risk for rupture, and the patient's life is at significant risk. AAA patients are typically asymptomatic; thus, rupture can occur at any time without any warning [11, 22].

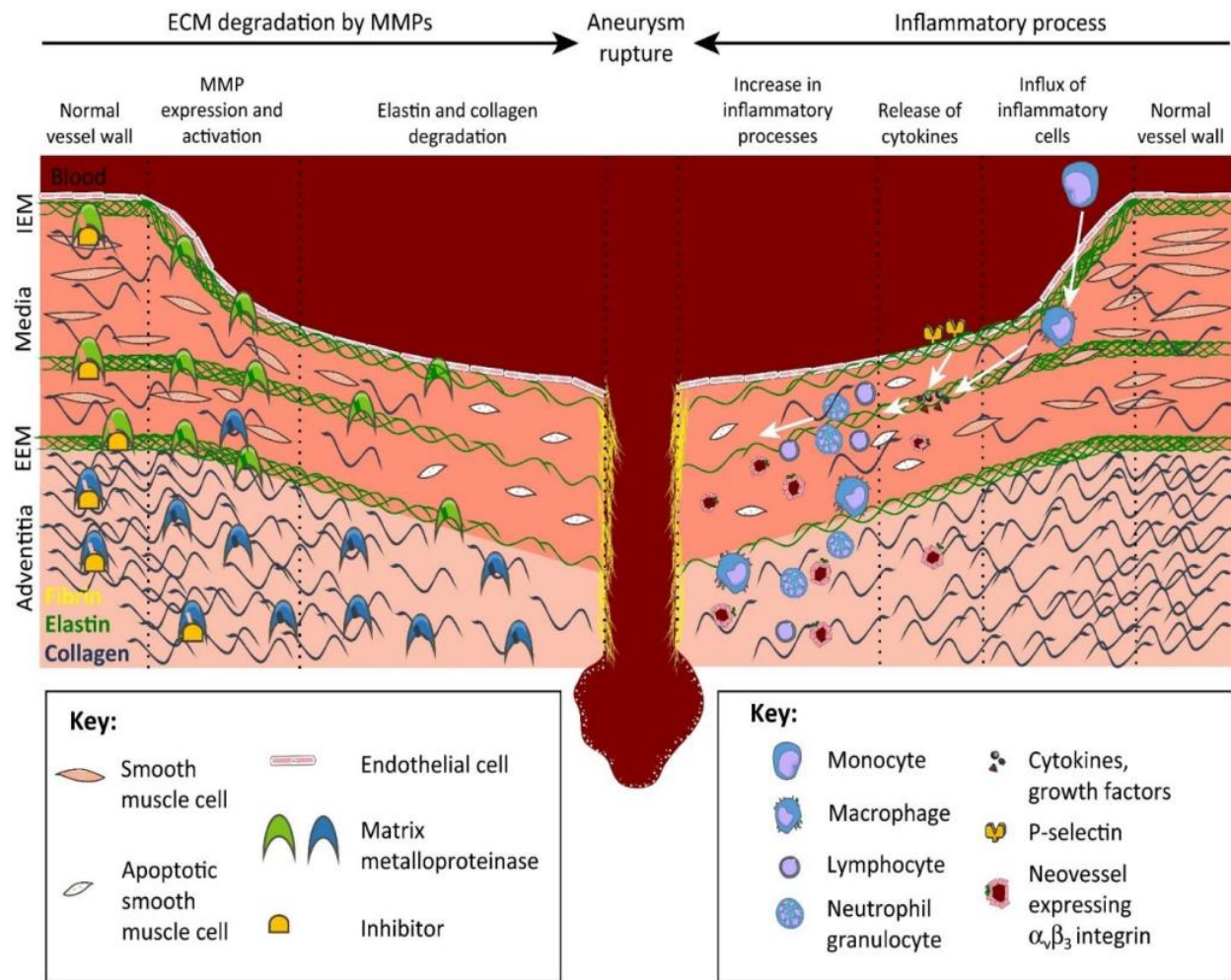
AAA and atherosclerosis are two different diseases [33]. However, they share two significant risk factors: smoking and male gender. Hypertension and increase in cholesterol indicate an elevated risk for atherosclerosis, but they are less associated with AAA [33].

The Pharmaceutical Aneurysm Stabilization trial reported a strong negative correlation with aneurysm growth rate and diabetes. One study found no correlation between AAA rupture and diabetes. However, when these studies were closely considered, it appeared that a variance in processes between AAA rupture and growth rate existed [33].

Extensive degradation of elastin is common in all AAAs. However, it has been shown that elastolysis occurs only in early stages of AAA formation, when the aneurysm is still small and at a low risk of rupture [33]. Perfusion of an aorta with elastase does not result in aneurysmal formation and indicates that elastin has a very minor role in load-bearing and rupture. Thus, efforts should be made to preserve the remaining collagen network [33].

Based on the current understanding of AAA disease, Lindeman et al. discussed the role of pro-inflammatory and anti-proteolytic drugs on AAA. Statins and angiotensin-converting-enzyme inhibitors, which decrease inflammation and protease activity, were tested in clinical trials in hopes of slowing or even halting AAA progression [33]. However, such drugs did not result in a positive change in aneurysmal progression and in some cases negatively affected patients with the disease. While clinical data was limited, the study could point to another mechanism of AAA growth yet

to be discovered or could be the result of a variance between pro and anti-inflammatory signals [33]. Figure 6 below shows the pathophysiology associated with the development and gradual progression of AAA [14]. Two distinct but related critical processes shown in Figure 6 are the degradation of extracellular matrix (ECM) proteins and inflammation. Initiation and progression



Trends in Molecular Medicine

Figure 6 The left half of the figure shows the molecular components involved in degradation of the ECM, such as matrix metalloproteinases (MMPs). The right half of the figure shows the action of proinflammatory cells--the macrophages, neutrophils, and lymphocytes--and how they move into the various layers of the tissue [14].

of an aneurysm is thought to result from imbalance between MMPs and their inhibitors, such as  $\alpha_2$ -macroglobulin [14]. The combined action of ECM degradation and inflammation causes the

aortic diameter to increase, which weakens the aortic wall and, eventually rupture of the aortic vessel wall becomes imminent, carrying a high mortality rate [14].

Smoking remains the strongest modifiable risk factor that promotes AAA growth rate and rupture [34]. Gender, age, and family history are also strong indicators [34]. Kuivaniemi et al. found that approximately 10% of AAAs exhibited a family linkage, with a 25% prevalence between brothers [35]. Another study investigating the predominance of family history reported that female family members displayed twice the level of prevalence for AAA [35]. A study of familial twins further reported that variable expression was 70% genetic, and 30% environmental factors [35].

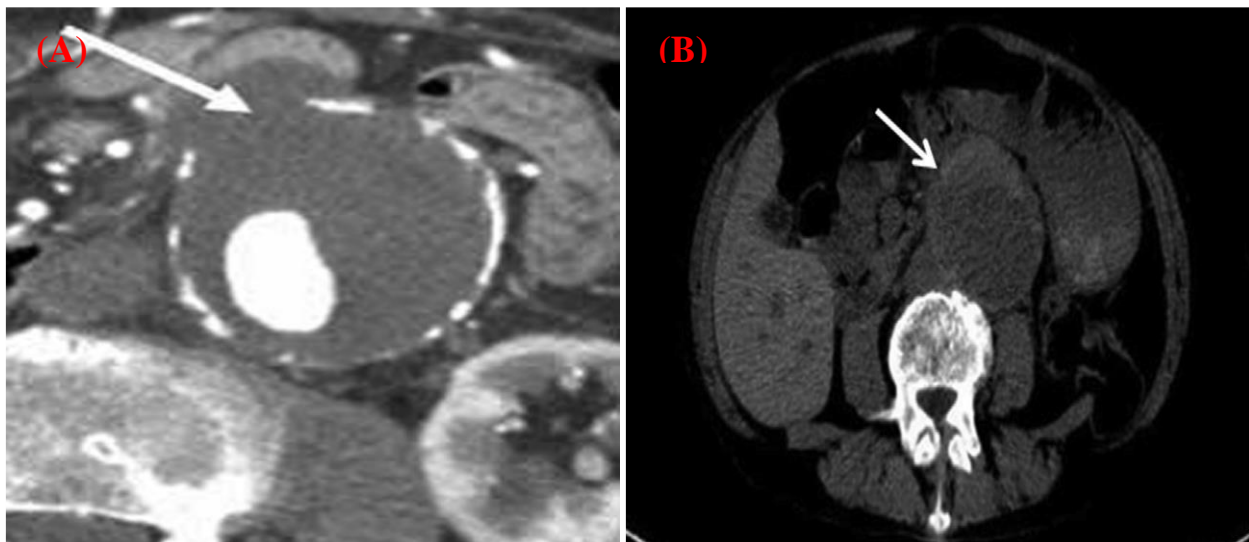
## **2.2. Imaging Techniques**

Ultrasound is most commonly used for AAA diagnosis and follow-up due to its safety and cost-effectiveness. Unfortunately, inter (2-10mm) and intra (2-7mm) observer variability are high when using this method [34]. CT and MRI provide more accurate measurements for AAAs but are resource-intensive. Ultrasound measurements also consistently underreport AA diameter [36]. Thus, ultrasound is generally used for large-scale screenings, while CT and MRI are utilized in the management of known AAAs [34]. Also, ultrasounds is capable of measuring pulse wave propagation, another potential rupture risk indicator. Pulse wave propagation is defined as the time a pressure wave takes to travel along a specific artery segment. Stiffer walls will have a faster pulse wave velocity [36]. CT and MRI can provide more detailed AAA geometry/anatomy information before surgical intervention, as well as wall calcification and density [36].

An intriguing new way of examining AAA rupture risk is through the use of 18-fluorodeoxyglucose positron emission tomography (18-FDG PET). AAAs exhibit an increased level of metabolic activity, which varies based on the number of T-lymphocytes, macrophages,

and other cells that express matrix metalloproteinases (MMPs) [13]. A higher metabolic activity results in an elevated uptake of glucose that could be indicative of increased ECM protein degeneration, resulting in a greater rupture risk. The amount of glucose uptake can be measured semi-quantitatively as the standard uptake value (SUV). SUV levels were reported to be twice as high in symptomatic AAAs compared to asymptomatic ones [13]. Although Wanhainen et al. stated that 18-FDG PET could not identify asymptomatic aortas, an inverse correlation was found between SUV and AAA expansion [34, 36]. In addition, MRI, with iron oxide as a contrast agent, were shown to be a viable imaging method of identifying AAAs [34].

Khan et al. discussed how the presence of a “crescent sign” on CT and MRI imaging could likely be indicative of aneurysmal rupture [13]. Crescent signs represent hematomas and are observed to be an area of high attenuation within the ILT or aortic wall on CT and MRI images [13]. One study reported that 21% of ruptured AAAs had a crescent sign, while none were observed on non-ruptured AAAs, as shown in Figure 7 [13].



### 2.3. Aortic Rupture Risk Predictors and Analysis

*Figure 7 (A) Contrast-enhanced abdominal CT image where the arrow is pointing at a discontinuity in the circumferential calcification of the aorta, indicating an anatomical area of potential rupture. (B) Unenhanced abdominal CT image where the arrow is pointing at the crescent sign, a potential sign of AAA rupture [13].*

There are several known predictors of impending AAA rupture: maximum transverse diameter of the aorta, cyclic strain measured via ultra-sound imaging, intraluminal thrombosis (ILT) volume, expansion rate of aortic diameter, and applied wall stress [11]. Some studies have hypothesized that peak wall stress is a better predictor of rupture than maximum transverse diameter [11, 37].

Maximum AAA diameter is the primary indicating factor for risk of rupture. However, there are concerns regarding the reproducibility of AAA measurements, as well as the ability of AAA diameter to consistently and accurately predict rupture [37]. Thus, intensive research has gone into finding other rupture risk indicators for physicians to supplement the AAA diameter criterion. Gasser et al. performed a large scale study involving 203 non-ruptured and 40 ruptured aortas [22]. Finite element models were used to pair peak wall stress (PWS) and peak wall rupture index (PWRI) with aortic diameter. They found that PWS increased linearly and PWRI increased exponentially. Based on this finding, Gasser et al. formulated a RRI that by subtracting a patient's specific diameter from the averaged diameter of patients with an equivalent PWRI. The change in diameter PWRI was found to be 14 mm greater in ruptured compared to non-ruptured cases, which is statistically significant [22]. This index is noteworthy as it allows for a size independent evaluation of risk based on simply measuring the patient's maximal diameter [22]. This study could be improved by using patient specific elastic properties instead of the mean population data. However, patient specific geometry was shown to be more important for stress estimations [16, 22, 38].

Sonesson et al. investigated the ability of aortic wall stiffness to act as an indicator of rupture risk potential [39]. They defined stiffness as,  $\beta = \ln(P_{\text{systolic}}/P_{\text{diastolic}})/[(D_{\text{systolic}} - D_{\text{diastolic}})/D_{\text{diastolic}}]$ . Also, they reported no significant difference in stiffness between ruptured

and non-ruptured AAAs. Sonesson et al. hypothesized that changes in elastin content alter mechanical properties of aortic walls, while changes in collagen content have minimal effect [39]. Performed tensile testing on porcine aortas exposed to collagenase indicated a significant increase in wall compliance that positively correlated with an increase to time of collagenase exposure. Wilson et al. also performed a study in hopes of determining the ability of aortic stiffness to act as a clinical risk factor for AAA rupture [37]. They found that patients whose AAA either ruptured or required surgical intervention exhibited a significant increase in aortic wall compliance, whereas patients whose aorta held up over time displayed a stiffer and less compliant wall [37]. These results prompted Wilson et al. to hypothesize that there were two types of AAAs, one in which an increase in diameter is accompanied with an increase in stiffness, and one in which stiffness is not increased [37].

Expansion rate has also been proposed as a possible indicator of rupture risk [37]. However, growth patterns for a specific AAA differ significantly through the disease's progression. For this reason, many authors state that future growth rates should not be extrapolated from past growth rate data [37]. AAA volume to be a superior predictive factor to maximal diameter because volume has a higher level of reproducibility [37]. In addition, oftentimes aneurysms grow and exhibit changes in morphology without a corresponding change in maximum diameter [37]. Further research should be conducted to determine a threshold level of AAA volume for surgical intervention.

A lower measurement of AAA wall distensibility compared to healthy AA walls has been shown [40]. The shape of an AAA may provide valuable information regarding the prediction of rupture [13]. There are two broadly categorized shapes of AAA: fusiform and saccular, with fusiform thought to have a higher propensity for rupture, as shown Figure 8 [13].



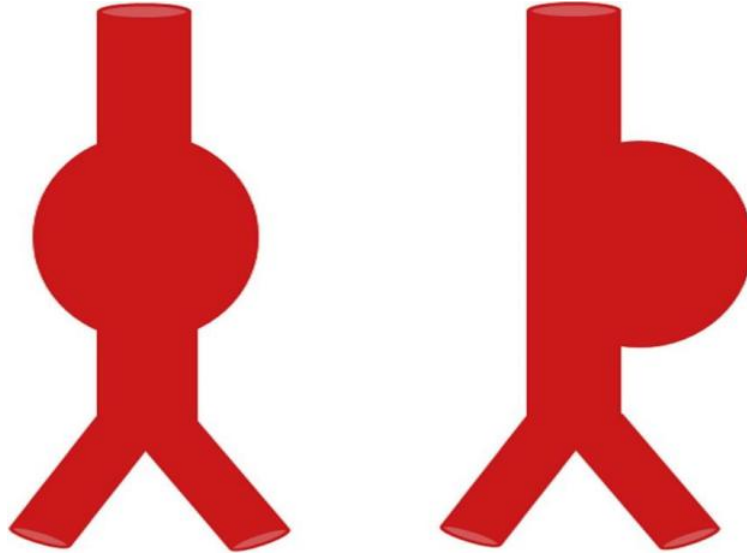


*Figure 8 Fusiform on the left, saccular on the right [7].*

A tortuosity index (TI), based on CT images, was developed to further assess the risk of rupture based on aortic morphology [13]. A TI of less than 1 indicates 1 major deviation from the central axis, whereas a TI of greater than 1 indicates multiple deviations from the central axis [13]. One study showed that before rupture, TI increased by 29% where mean diameter increased by only 3% [13].

Shang et al. reported that the assumption of a varying aortic wall thickness resulted in significantly different (PWS) measurements [6]. The estimated PWS correlated positively with aneurysmal expansion rate (Figure 9) [6]. Martufi et al. also discussed how wall thickness is non-uniform in AAAs [41]. The question as to whether thickness significantly varies between ruptured and non-ruptured AAAs remains to be answered. Martufi et al. discussed how thicker walls may indicate a higher level of wall inflammation, resulting in a higher rupture risk; thinner walls exhibit a higher level of stress concentration, also increasing rupture risk [29, 41]. Based on these findings, variable wall thickness should be included in future FEMs [6].

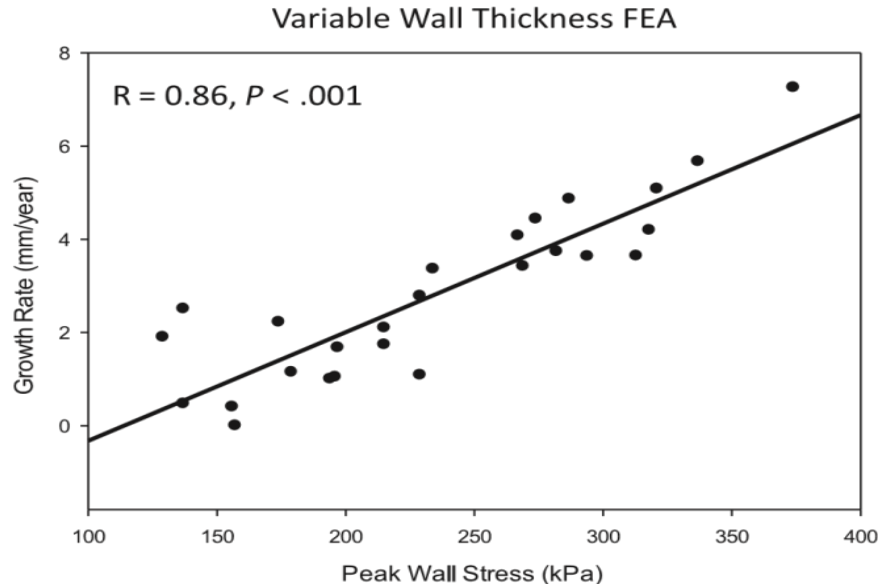


Figure 9 PWS with variable thickness vs expansion rate [6].

Li. et al. investigated the relationship between hemodynamic flow and aortic vessel geometry with risk of rupture [42]. They utilized a fluid-structure interaction model to determine whether hemodynamic flow patterns significantly influence wall stress distributions [42]. Large aortic neck angles resulted in higher wall stress. Future research into hemodynamic flows should be pursued to further understand and quantify complex stress distributions [42]. Table 2 summarizes the current clinical imaging modalities and most utilized risk-assessment practices.

Table 2 Summary of Imaging modalities and assessment capability

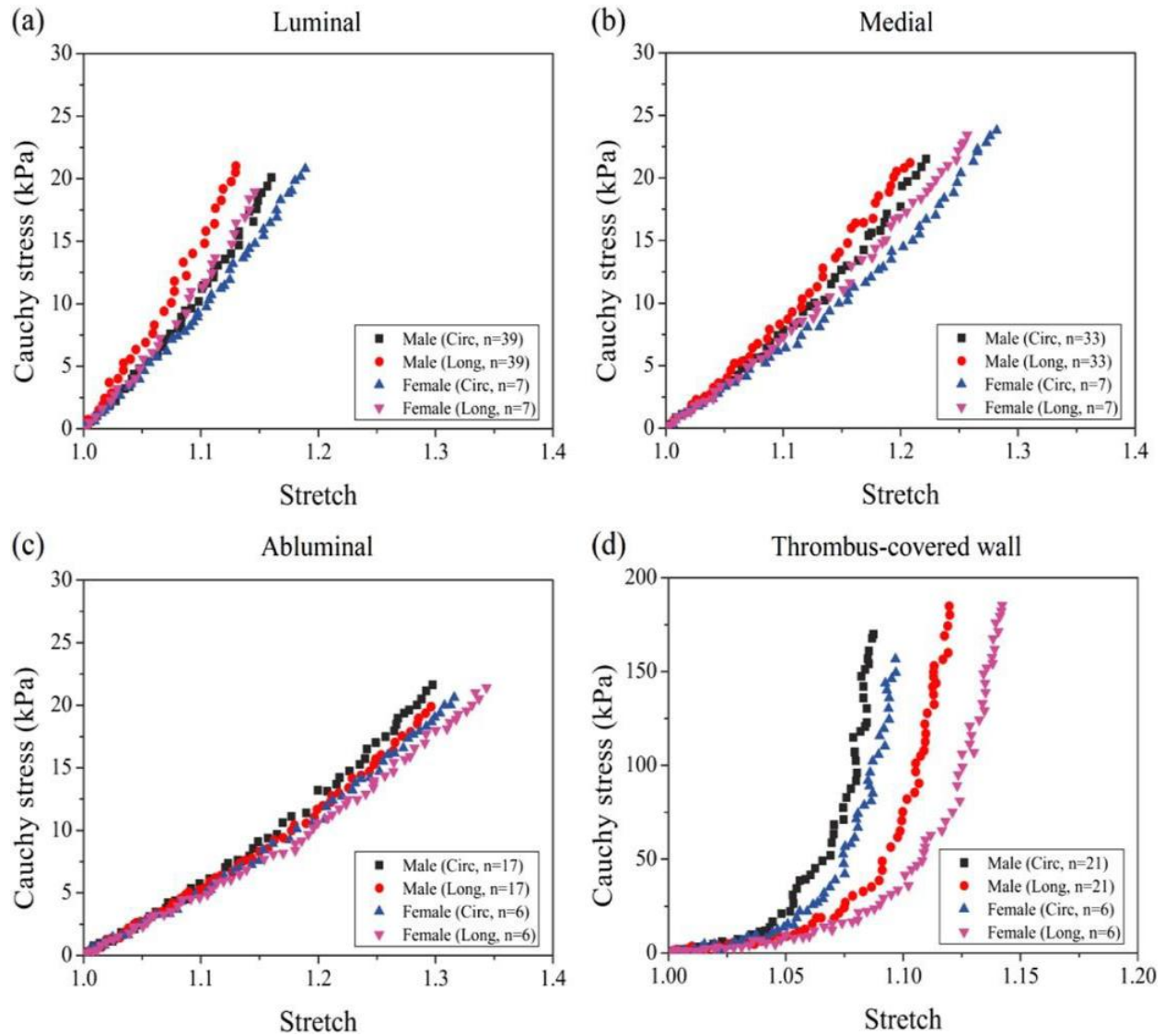
Imaging Modality	Measurable	Result
Ultrasound	Diameter	Diagnostic criterion/ High observer availability
	Stiffness	Using pulse wave propagation, the time a pressure wave takes to travel along an artery segment measures the stiffness.
	Cyclic strain	The strain of the pulsing blood vessel

Table 2 (Cont.)

<b>Imaging Modality</b>	<b>Measurable</b>	<b>Result</b>
CT scan/ MRI scan	Diameter, volume of AAA, tortuosity, calcification, ILT volume, wall thickness, and distensibility.	Provide information about the biological state of the tissue and areas of potential rupture
18-FDG PET scan	Metabolic activity which varies based on the number of T-lymphocytes, macrophages, and other cells that express matrix metalloproteinases (MMPs)	Increased metabolic activity and glucose uptake appears to correlate with AAA growth

#### **2.4. Differences in Rupture Risk for Males vs. Females**

Female abdominal aortic aneurysms generally grow faster and have a weaker aortic wall [7]. Larson et al. compared PWS and peak wall rupture risk (PWRR) between fifteen diameter and age matched males and females [43]. No statistically significant differences were reported for PWS, PWRR, or mean ILT volume, although PWRR was higher among females. The lack of statistical significance was perhaps due to the small sample size [7]. The study applied male biomechanical wall properties to female AAAs, which eliminated the slight difference in PWRR between men and women. Larsson et al. hypothesized that based on these results, AAA geometry alone does not account for the difference in rupture risk [43]. In contrast, biomechanical properties likely have an impact on rupture risk [7]. Tong et al. performed a large scale study in which various properties and clinical factors of 90 AAA samples were compared with respect to gender (78 male, 12 female) [19]. The data reported a weaker aneurysmal wall in females as well as a weaker ILT in the longitudinal direction (Figure 10).



*Figure 10 Mechanical responses of male and female ILTs and underlying aneurysmal wall in the circumferential and longitudinal directions [19].*

Additionally, it was observed that 82% of females had thrombi classified as old (phase 3 and 4), compared to only 43% of males. Weaker underlying aortic walls are characteristic of older thrombi [32]. Thus, the difference in mechanical properties of the aortic wall between males and females could be caused by aging thrombi in women. Males were also shown to have a statistically significant larger amount of dry weight collagen and a statistically significant lower amount of dry weight elastin [44]. Gasser et al. performed diameter conversion where PWRI indicated that a

50mm diameter in females had an equivalent rupture risk to that of a 63mm diameter in males [38].

*Table 3 PWS, PWRR, and ILT volume in men and women [43].*

<i>Biomechanical properties</i>	<i>Gender</i>		<i>P value</i>
	<i>Men</i>	<i>Women</i>	
PWS (kPa, mean)	198 (111-266)	184 (120-282)	.42
PWRR (mean)	0.43 (0.24-0.66)	0.54 (0.28-0.85)	.06
ILT (mm <sup>3</sup> , mean)	45,008 (2371-114,679)	42,070 (714-83,361)	.81

*ILT, INTRALUMINAL THROMBUS; PWRR, PEAK WALL RUPTURE RISK; PWS, PEAK WALL STRESS.*

## 2.5. Geometry of Vessel Wall and Role of Intraluminal Thrombus

When wall stress exceeds wall strength, AAA rupture occurs. Stress and strength estimates of the abdominal aortic wall prove valuable because they play a role in rupture prediction. It was originally assumed that the AA could be modeled as a perfect cylinder. However, more recent studies have shown that the AA displays a high level of tortuosity, which results in uneven and difficult stress distribution predictions. Furthermore, geometries vary significantly from patient to patient [16]. Vorp and Vande Geest used a continuum-based constitutive model in a finite element analysis on a geometrically patient-specific basis that showed a large range of peak stresses (29 to 45 N/cm<sup>2</sup>) in a single AAA [16]. Differences in wall stresses are mainly due to differences in surface geometry. The differences were introduced by varying AA material parameters from their “biologically reasonable” minimums and maximums in repeated finite element analysis on a hypothetical AAA. The variations in material parameters resulted in little difference of stress observed, meaning AAA geometry is the key determining factor of stress distribution [45].

Other studies have shown that wall thickness is not uniform in an AAA and should be taken into account in order to more accurately predict wall stress [16]. Ex vivo tensile testing reported a 50% decrease in wall strength for diseased aortas [16]. However, as of 2005, there was no known method for non-invasively measuring wall strength. ILTs are found in most AAAs, so their mechanical properties should also be considered when estimating wall stress and strength. Testing has shown that the presence of an ILT acts to shield the aortic wall by up to 30% [16]. As the ILT grows, the diameter through which blood flows decreases, which increases blood flow speed and decreases pressure exerted on the ILT. However, the presence of an ILT also lowers aortic wall strength, and larger volume ILTs result in a greater weakening effect on AA wall strength, as reported in Figure 11.

## Association of Wall Strength with ILT Thickness

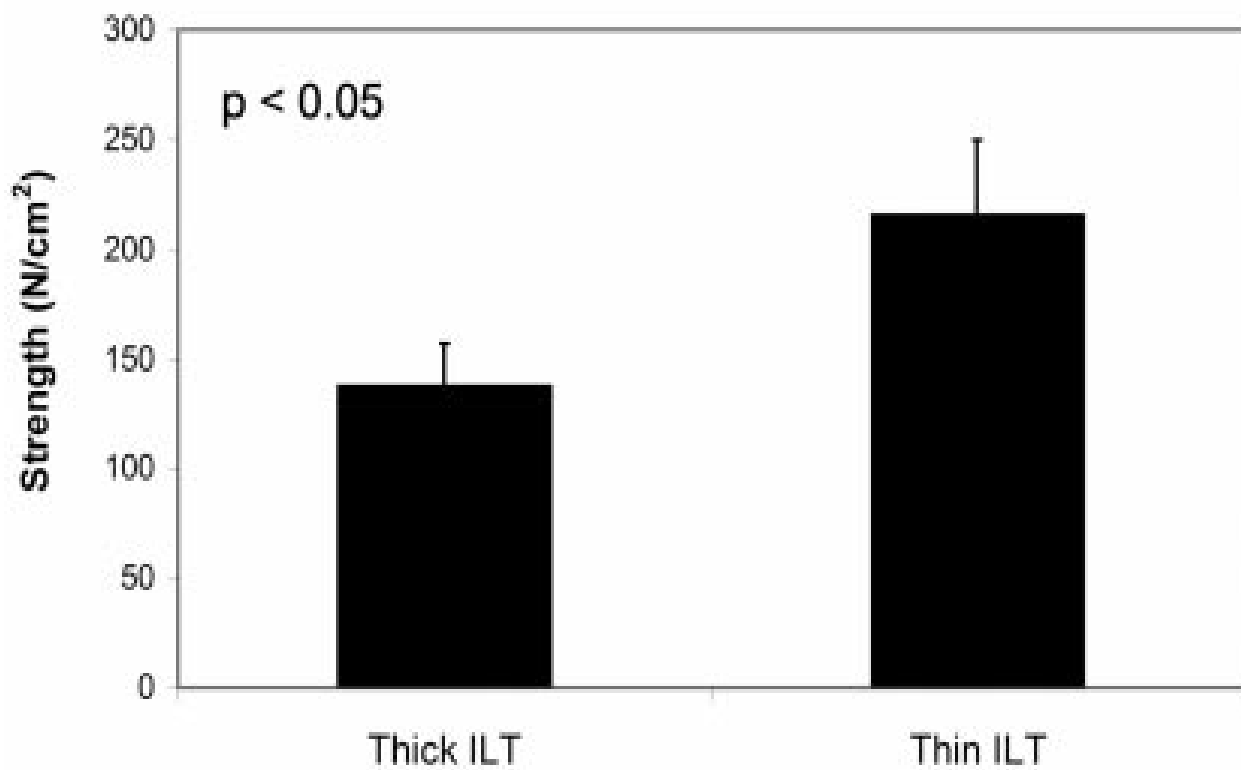
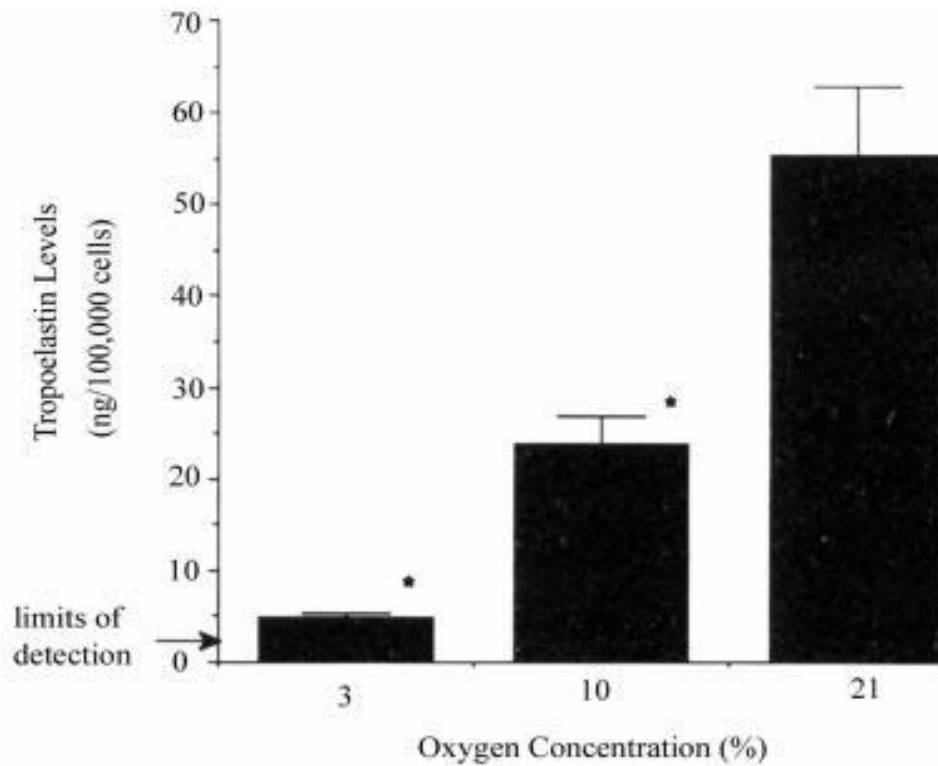


Figure 11 The relationship between Intraluminal thrombus (ILT) thickness and aortic wall strength [16].

The ILT's mechanical behavior can be described as non-linear elastic, inhomogeneous, and isotropic [45]. Ultrasound-based experiments have shown that the ILT is incompressible, which further supports the idea that it acts to reduce stress exerted on the aortic wall [45].

Studies supported the hypothesis that relates to abdominal aortic wall weakening and ECM protein degradation [16, 26]. Two different mechanisms have been suggested to explain abdominal aortic wall weakening and ECM protein degradation: Stress-mediated and hypoxia [16]. In the stress-mediated state, an inverse relationship between diameter and elastin concentration has been reported [16]. "Saccular outpouchings" observed in the AA wall indicated elevated stress and exhibited a decrease in collagen and elastin content [16]. Furthermore, it has been shown that

mechanical forces alter the ECM expression in a variety of cells [16]. Hypoxia experiments have indicated that depriving arterial smooth muscle cells of oxygen can result in decreased expression of collagen and tropoelastin. Decreased expression of tropoelastin is shown in Figure 12 [16].



*Figure 12 Oxygen concentration effect on Tropoelastin levels [16].*

Hypoxic regions along the AA wall occur due to the buildup of ILT. Thicker ILTs cause a greater level of hypoxia [16]. Thus, it is crucial to study the breakdown mechanisms of ECM proteins, such as collagen, in order to improve AAA growth comprehension, to observe how rupture may take place, and to predict when rupture may occur.

An increase in the production of proteolytic enzymes such as collagenase is thought to play an important role in the formation and rupture of abdominal aortic aneurysms. Whether stress-mediated or hypoxia-mediated, an increase in expression of various matrix metalloproteinases



results in degeneration of structural proteins in the ECM [45]. As collagen is one such structural protein, and as its exposure to collagenase results in a weaker and more compliant tissue, it follows that increased exposure of abdominal aortas to collagenase will result in a weaker aortic wall. Thus, such aortas would have a significantly greater risk of rupture.

Biasetti et al. proposed a model to study the fluid-chemical integration in order to observe its role in the formation of ILT in AAA [8]. To mimic a fusiform aneurysmal geometry, they created a 2-D axis symmetric AAA model. The aneurysm had a small luminal diameter (4.4 cm), a clinically relevant size to affect blood flow (Figure 13) [8].

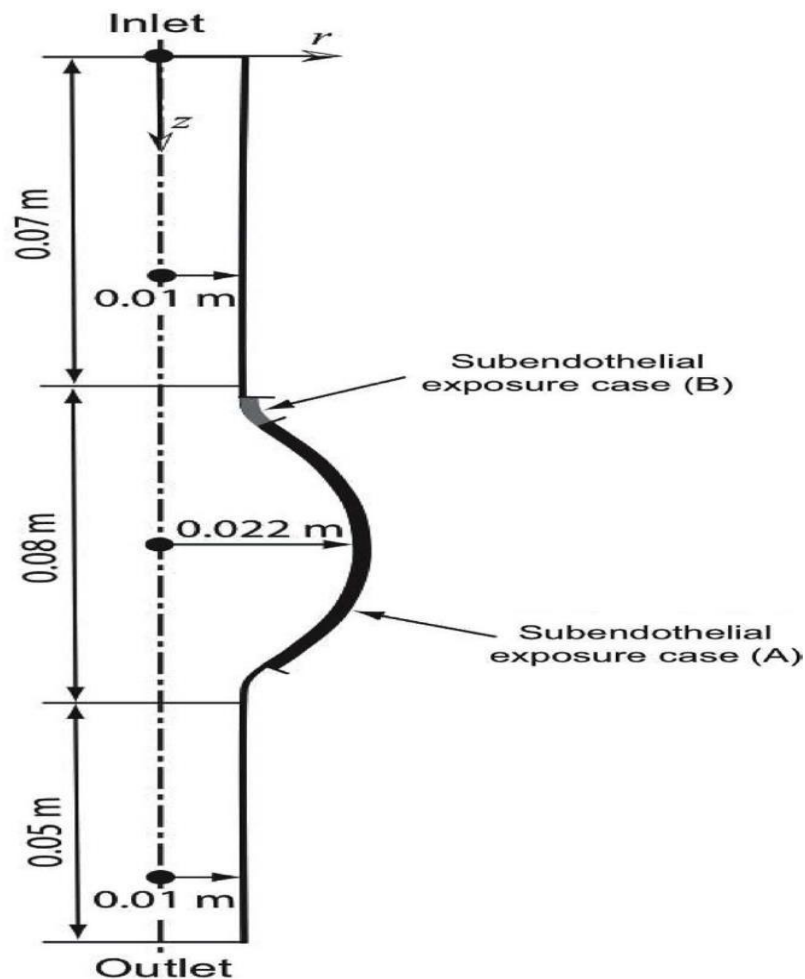


Figure 13 shows an axisymmetric fusiform AAA. Case A is a large exposure of subendothelial layer, and case B is a small exposure of subendothelial layer [8].

ILT is considered in this model as a thin-layer covering the wall of the aneurysm. Looking at Figure 13, case A considers a large exposed area of endothelial cells, where case B considers a much smaller area [8]. The purpose of considering the two cases is to observe the effects of different sizes of sub-endothelial exposure in ILT formation and, ultimately, blood flow. In addition, coagulation cascade that causes thrombin formation was considered in this model. The extravascular tissue factor (TF) is present under the sub-endothelial layer. TF binds to blood-borne factor VIIa upon exposure of sub-endothelial layer to the blood. TF binding with blood-borne factor VIIa initiates the coagulation cascade. The coagulation cascade employs a group of factor

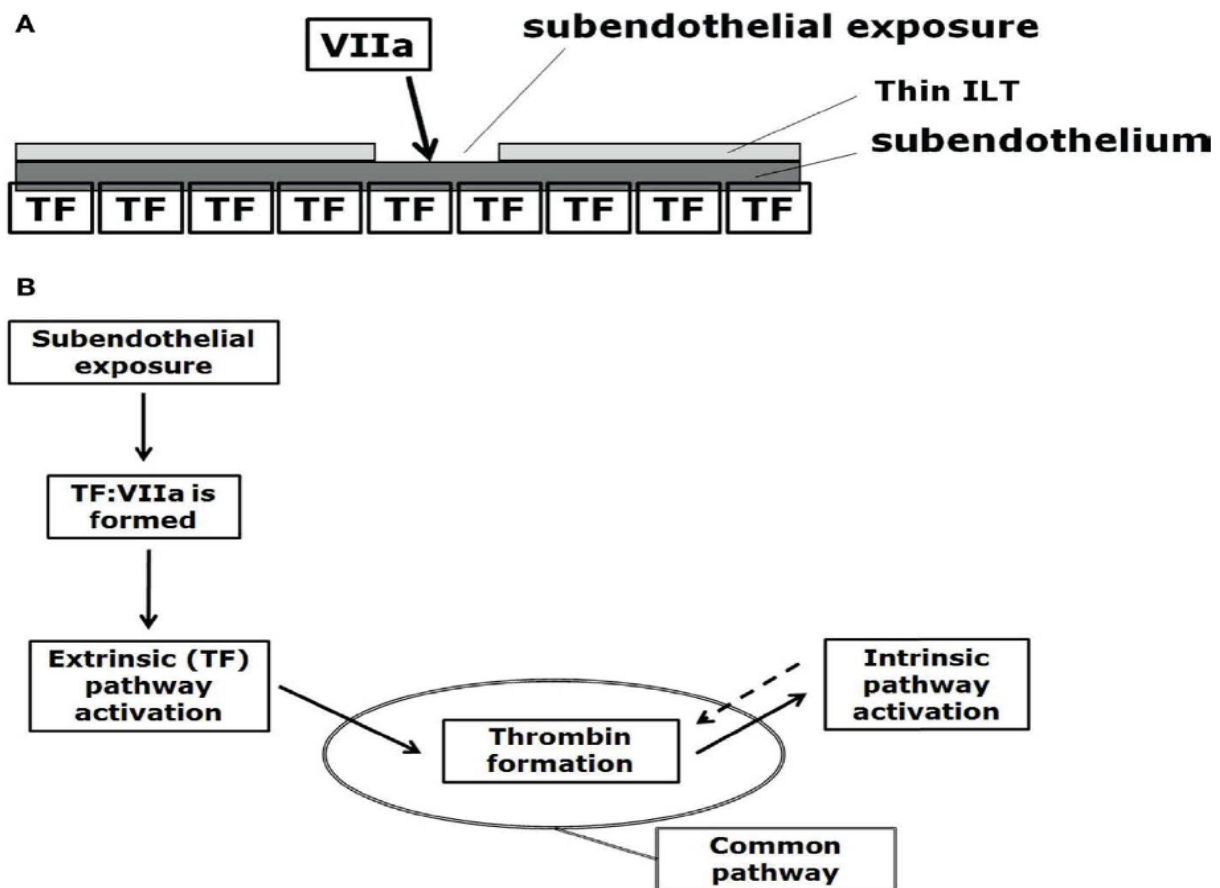


Figure 14 demonstrates A, when the subendothelial layer is exposed and TF binds to blood-borne factor VIIa to initiate the coagulation cascade, and B, where the steps of the coagulation cascade are shown for thrombin formation [8].

enzymes that activate one another and ultimately aid in the formation of active thrombin [8].

Figures 15-18 show the results of the coagulation cascade (CC), VS dynamics coupled with flow field, spatially averaged wall shear stress, and thrombin distribution models, respectively:

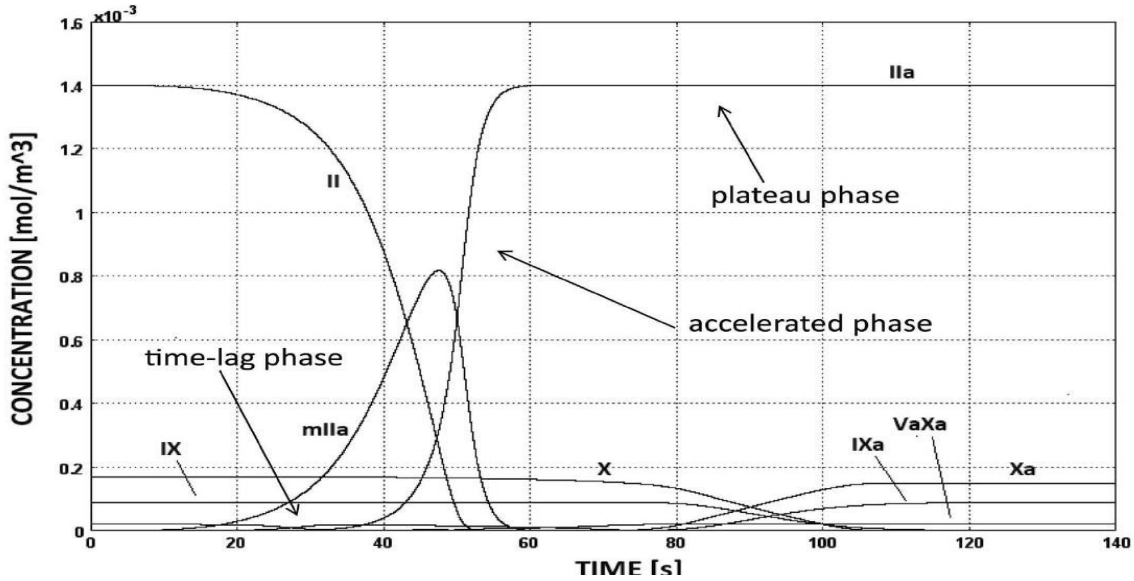


Figure 16 shows the concentration of some the enzymes as blood flows and a chemical reaction takes place with the AAA wall. The three distinct phases of thrombin formation are time-lag, accelerated, and plateau phases, as shown [8].

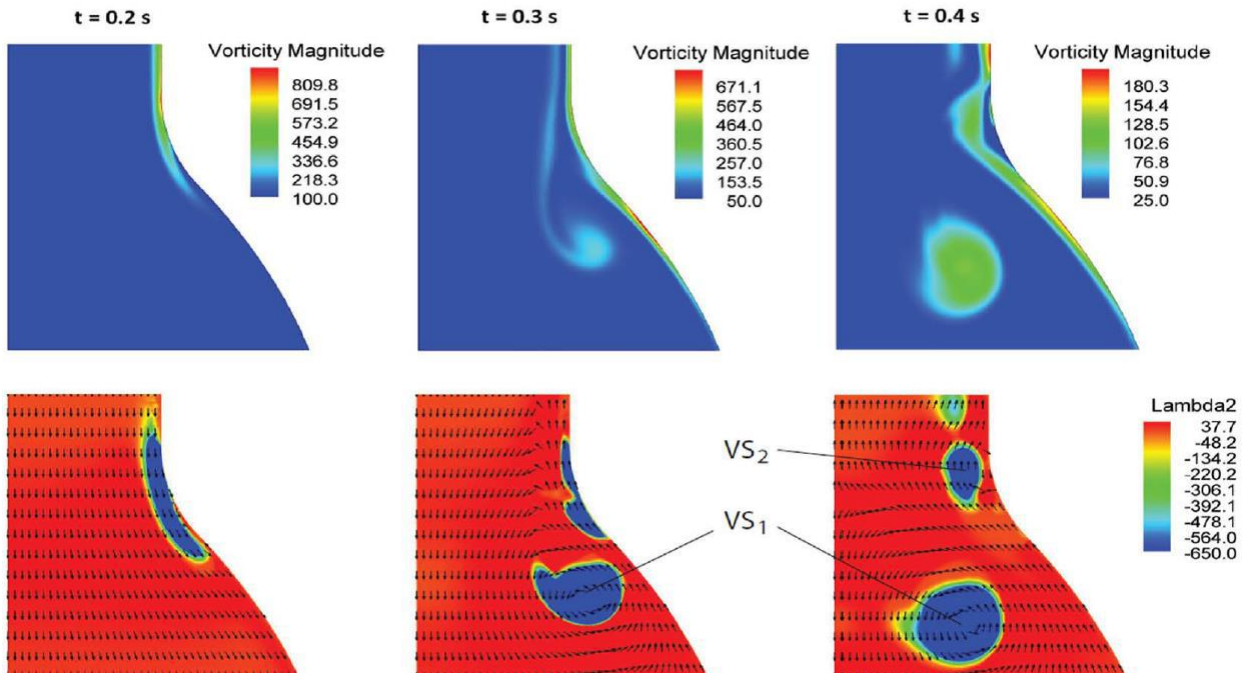


Figure 15 shows, for three different time points of the cardiac cycle, the vorticity magnitude ( $s^{-1}$ ) in the first row, and VSs values using the Lamda2 method ( $s^{-2}$ ) in the second row [8].

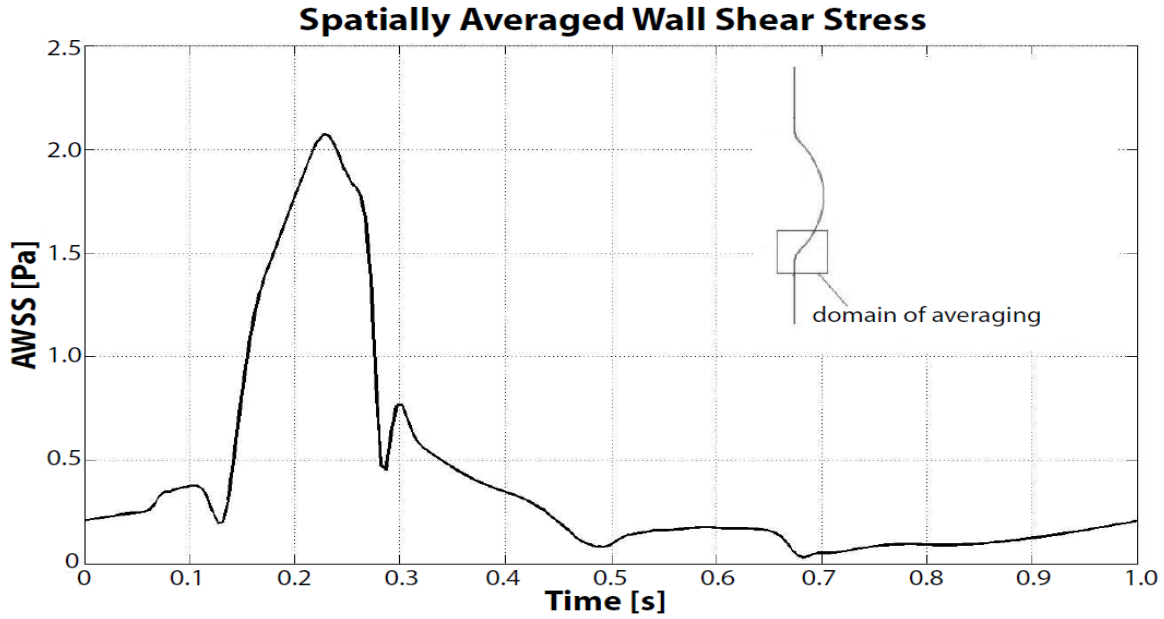


Figure 17 shows the spatially averaged wall shear stress (AWSS) vs time during contraction phase (systolic) of cardiac cycle. It is shown that AWSS increased by about 4-fold during VSs impingement ( $t=0.15$  s to 0.4 s) with respect to relaxation phase (diastolic) of cardiac cycle [8].

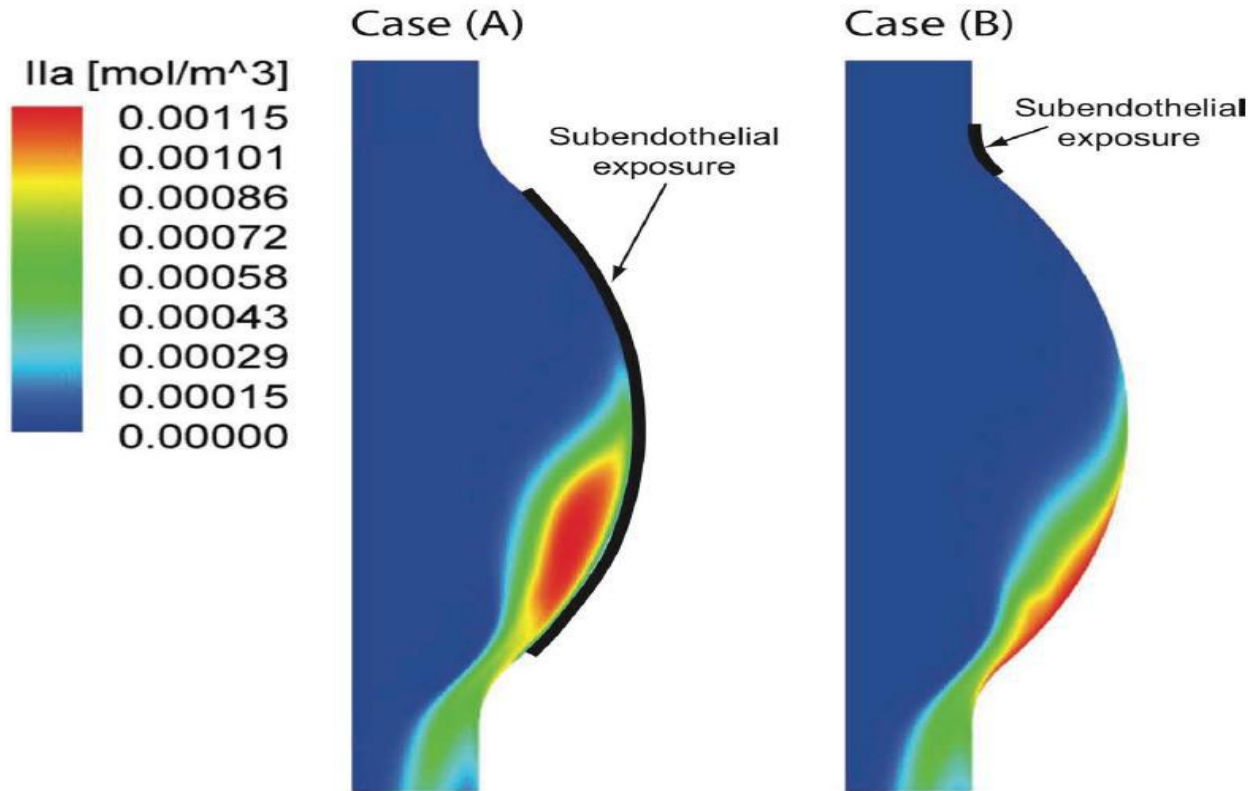


Figure 18 demonstrates thrombin formation for case A, large subendothelial exposure, and case B, small subendothelial exposure [8].

Thrombin formation in the lumen of the aorta is triggered when the interior wall of the aorta is degraded, and the subendothelial layer is exposed to enzymatic factors IX and X in the blood [8]. The production of thrombin is slow at first, then rapidly increases when the intrinsic pathway is activated, and, finally reaches a plateau, as illustrated in Figure 15. It can be concluded that large damaged areas of the AAA will result in large endothelial layer exposure to the flowing blood, affecting blood flow, and ultimately increasing the rate of thrombin formation [8].

The presence of thrombin alters the trajectory of fluid flow in the aneurysmal cavity, which generates complex flow fields, also known as coherent vertical structures VSs [8]. VSs resemble turbulent fluid flow in a way, as shown in Figure 16. When intense VSs interact with the layer of the thrombic mass, shear stress spikes, as shown in Figure 17. An increase in shear wall stress against the thrombus can result in the release of small emboli into the blood stream. The emboli will circulate in the body and can potentially cause strokes. When more surface area of the subendothelial layer is exposed to the blood, more thrombin formation occurs. The turbulent nature of blood flow in the aneurysmal region causes thrombin to form in the distal part of the aneurysm. For cases A and B, as shown in Figure 18, thrombin formation took place in the distal region of the AAA, with case A producing more than case B [8].

This model coupled fluid domains with chemical domains, which can aid in discovering the unknown mechanisms and the risks associated with increased formation of ILT in AAA. In addition, the effect of ILT on wall stress is noteworthy. Some studies have shown that ILT formation is a natural positive response to protect against aneurysmal rupture [10].

According to Mower et al., ILT presence on the aneurysmal wall can be helpful in providing some resistance against tissue failure or rupture [10]. ILT can reduce the applied stress at that location on the aneurysmal wall. Mower et al. used FEM to examine the effect of ILT on AAA wall stress. Their FEM had the following assumptions: axisymmetric structure, elastic deformation, homogeneous microstructure, isotropic material behavior, and no external forces or pressure effects. The FEM consisted of three concentric layers, as shown in Figure 19. ILT was introduced in the aneurysmal cavity [10].

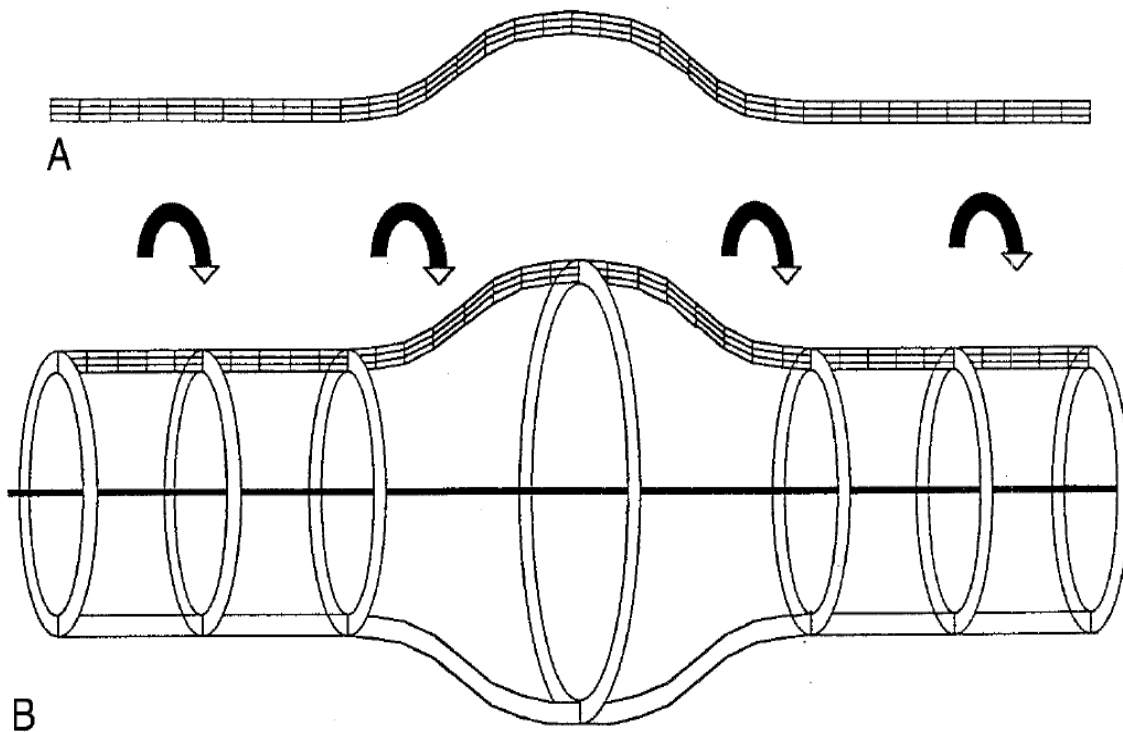


*Figure 19 an axisymmetric finite element grid of a small aneurysm is shown in A. Rotation of the grid in A about an axis of symmetry generates the 3D structure shown in B [10].*

ILT effects on maximum wall stress were observed with variations of three parameters, as shown in Figures 20 to 22: relative thrombus depth (or thickness of ILT), thrombus elastic modulus, and AAA wall elastic modulus for ILT elastic modulus of 0.02 MPa and 0.20 MPa [10].

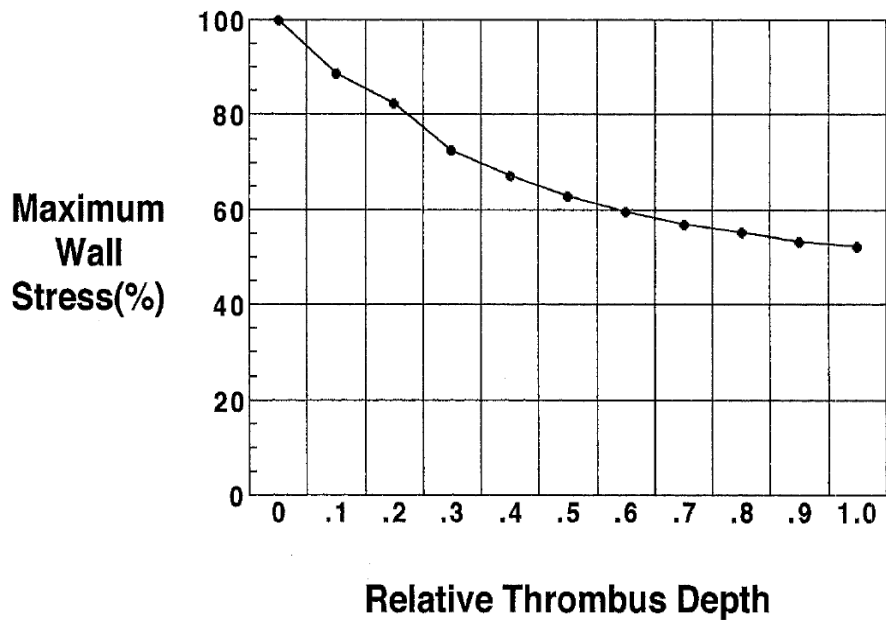


Figure 20 the size of the ILT helps in decreasing the maximum wall stress on the AAA's wall. Maximum wall stress is expressed as percentage of stresses in the aneurysm with no ILT and thrombus depth is a fraction of the diameter [10].

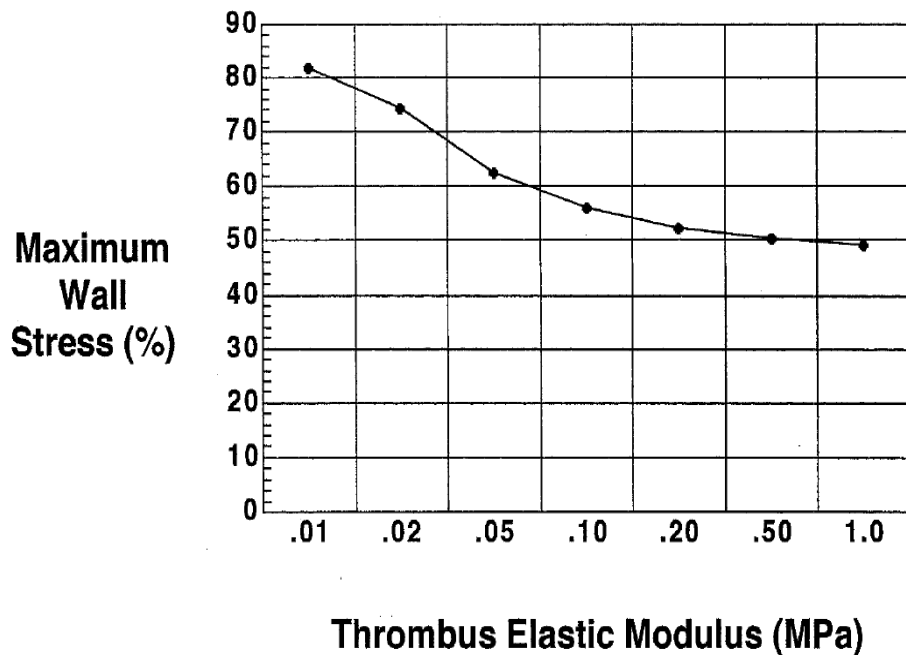
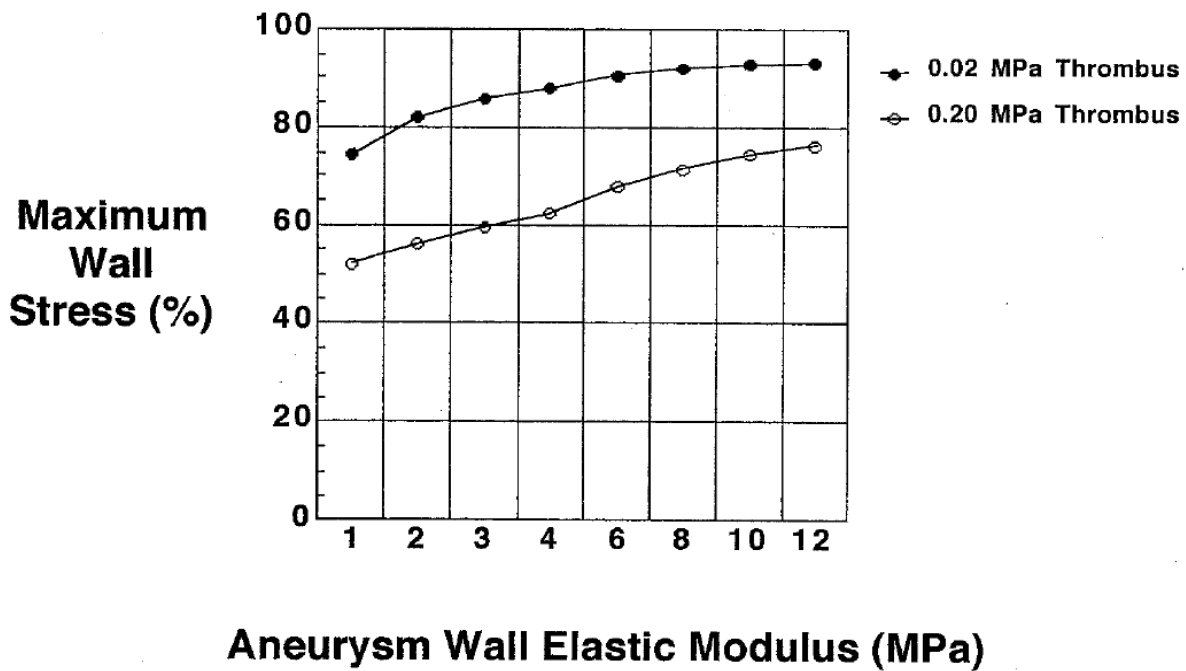


Figure 21 A decrease in maximum wall stress was observed as the elastic modulus (strength) of ILT increases. Maximum wall stress was expressed as percentage of stresses in the aneurysm with no ILT [10].



*Figure 22 as the AAA's wall became stiffer, ILT was not able to absorb much of the stress, unless ILT had a high Elastic modulus. Maximum wall stress was expressed as percentage of stresses in the aneurysm with no ILT [10].*

Figures 20-22 showed that the presence of ILT resulted in reducing the maximum wall stress applied on the AA wall by at least 30% for all three parameters [10]. Thus, it can be concluded that the presence of ILT can support the wall of AAA to some extent. Mower et al. suggested that ILT formation is a natural response to protect against aneurysmal rupture, because ILT absorbs wall stress [10]. Also, they suggested that a larger ILT provides more protection as long as the size of the ILT is small relative to the aneurysmal volume, and the protection decreases as the ILT size approaches the size of the aneurysmal cavity. However, the effect of ILT on blood flow and shear stress must not be ignored. The presence of ILT with a significant mass alters the nature of blood flow from laminar to turbulent flow. The presence of turbulent flow can cause elevated shear wall stress and ILT formation rate to increase [8].



Vorp and Geest demonstrated a patient-specific biomechanics approach to understand the process and to predict rupture in AAA patients [3, 7]. They focused on the derivation of constitutive relationships via in-vivo mechanical testing and ex-vivo tensile testing. In-vivo imaging testing is non-invasive and done via CT scans and ultrasound techniques. Such techniques are the most common to detect AAAs via modeling of the aneurysm using FEM. Also, they help in detecting ILT via recording measurements of compliance. However, in-vivo imaging testing is not sufficient to derive the constitutive models for patient-specific, local wall stress analysis. Rather, ex-vivo tensile testing is typically performed in order to derive constitutive equations. Vorp and Geest considered anisotropic properties for human abdominal aorta in their model [3, 7]. Their work was the first to propose an anisotropic constitutive relation for AAA [3, 7]. The effect of the presence of ILT on wall stress and the thickness effect of ILT on wall strength, wall stress, and RPI for patient-specific AAA are shown in Figures 23-24.

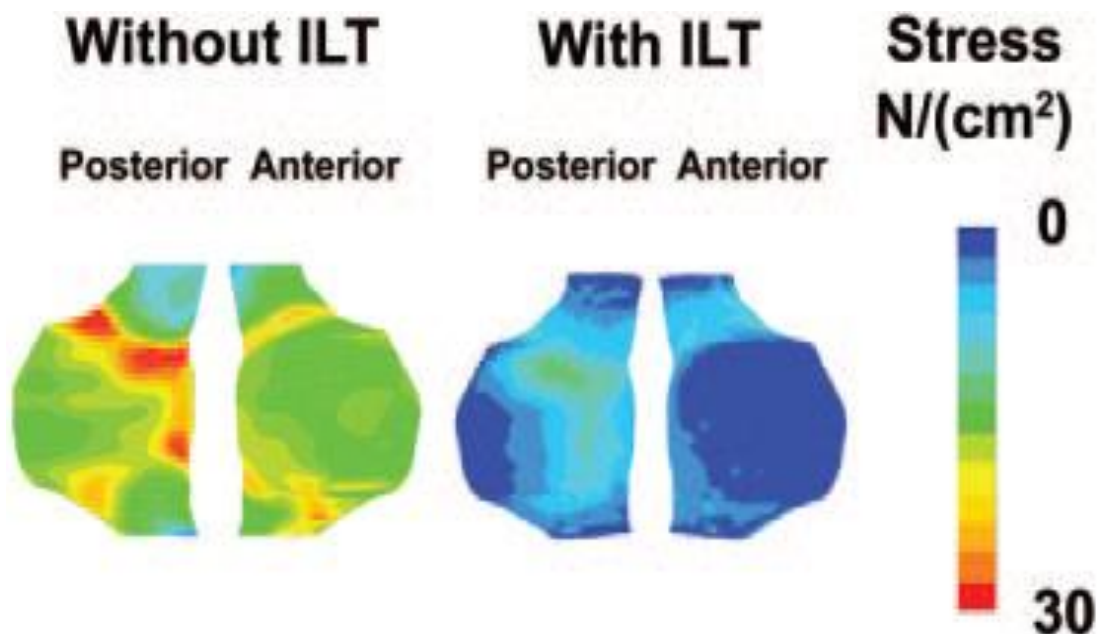


*Figure 23. The effect on ILT on wall stress implies that ILT helps in reducing wall stress on AAA's wall [3].*

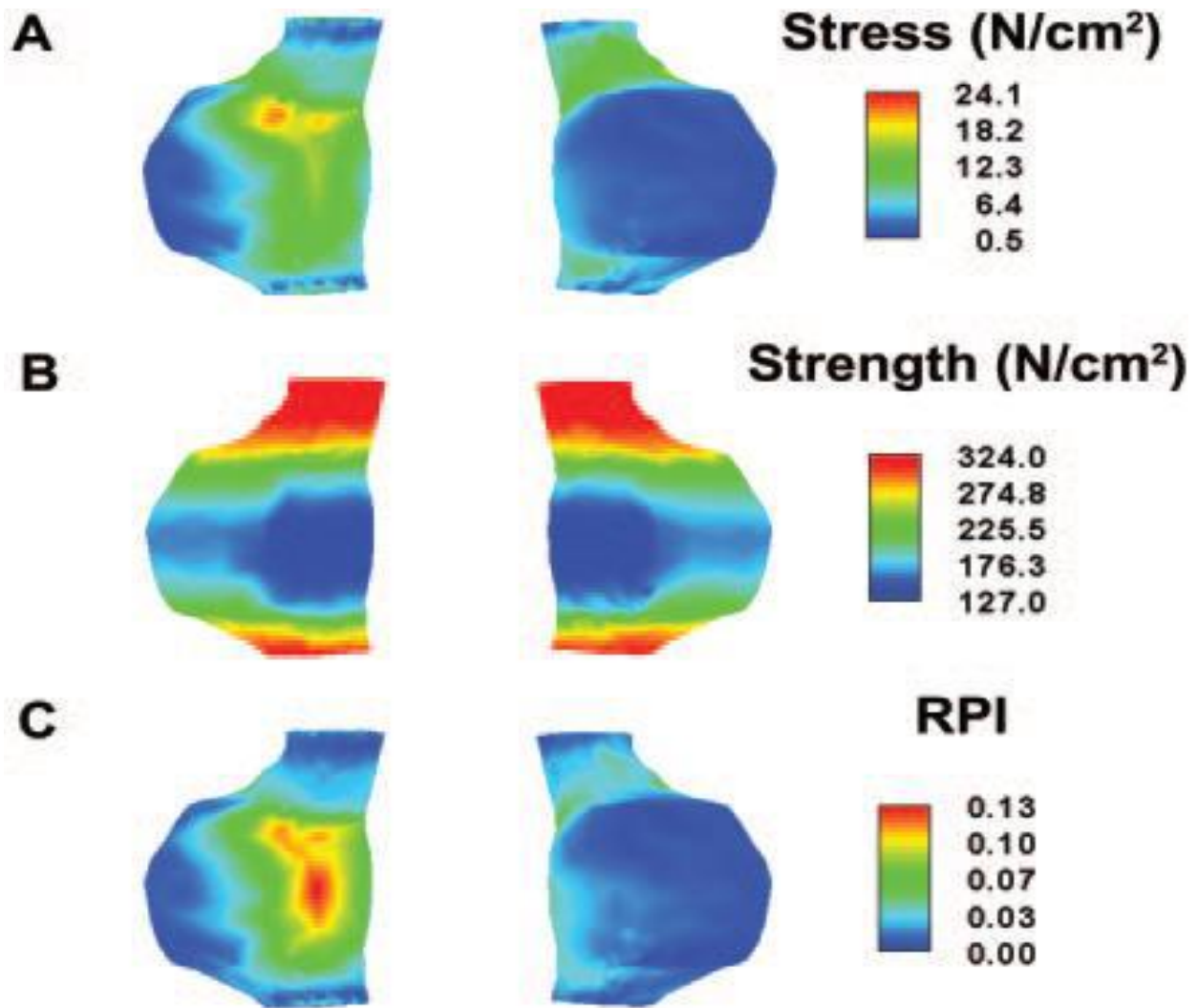


*Figure 24 Wall stress (A), strength (B), and RPI (C) for a patient-specific AAA [3].*

Vorp and Geest suggested that the presence of ILT in finite element analysis of AAA was essential for accurate computations, because ILT played a vital role in reducing wall stress, as shown in Figure 23 [3]. Thicker size of ILT decreased wall tensile strength, but thinner ILT increased wall tensile strength, as shown in Figure 24.

Equation 5 was used to calculate the wall strength noninvasively based on the patient's age, sex, smoking status, family genetic history of AAA, and size of AAA [3].

$$\begin{aligned} \text{Strength} = & 141.26 - 17.16 * \text{ILT} + 3.39 * \text{Age} - 257.30 * \text{Nord} - 69.5 * \text{Hist} \\ & + \epsilon \end{aligned} \tag{2.1}$$

where strength is in N/cm<sup>2</sup>, ILT thickness (cm), age (in years), and size of AAA (cm) are represented in Equation 5 [3]. The equation above was applied for a patient-specific AAA and the results were demonstrated in Figure 24B. There is a need for biomechanical, noninvasive techniques that measure wall stress, wall strength, and potential rupture site. The development of such techniques will aid in evolving a prognostic tool for clinicians to use.

Wilson et al. provided an in-depth review of the intraluminal thrombus, which is present in most AAAs [46]. Wilson et al. hypothesized that ILT formation was likely in part due to a disturbance in hemodynamic blood flow. AAAs contain areas of high and low shear stress regions. Wilson et al. stated that high shear stress regions might result in blood platelet activation, while regions of low shear stress provided a place for platelets to aggregate [46]. Boyd et al. also investigated blood flow characteristics and wall shear stress at the point of aneurysmal rupture. They found that rupture was associated with low levels of wall shear stress. These low levels of wall shear stress correlated with areas of low blood flow velocity and recirculation, shown in Figure 25. Additionally, these areas of rupture were further characterized by a greater amount of ILT relative to the rest of the aorta, indicating that this recirculating flow pattern and resultant low shear stress contributes to ILT formation [12].

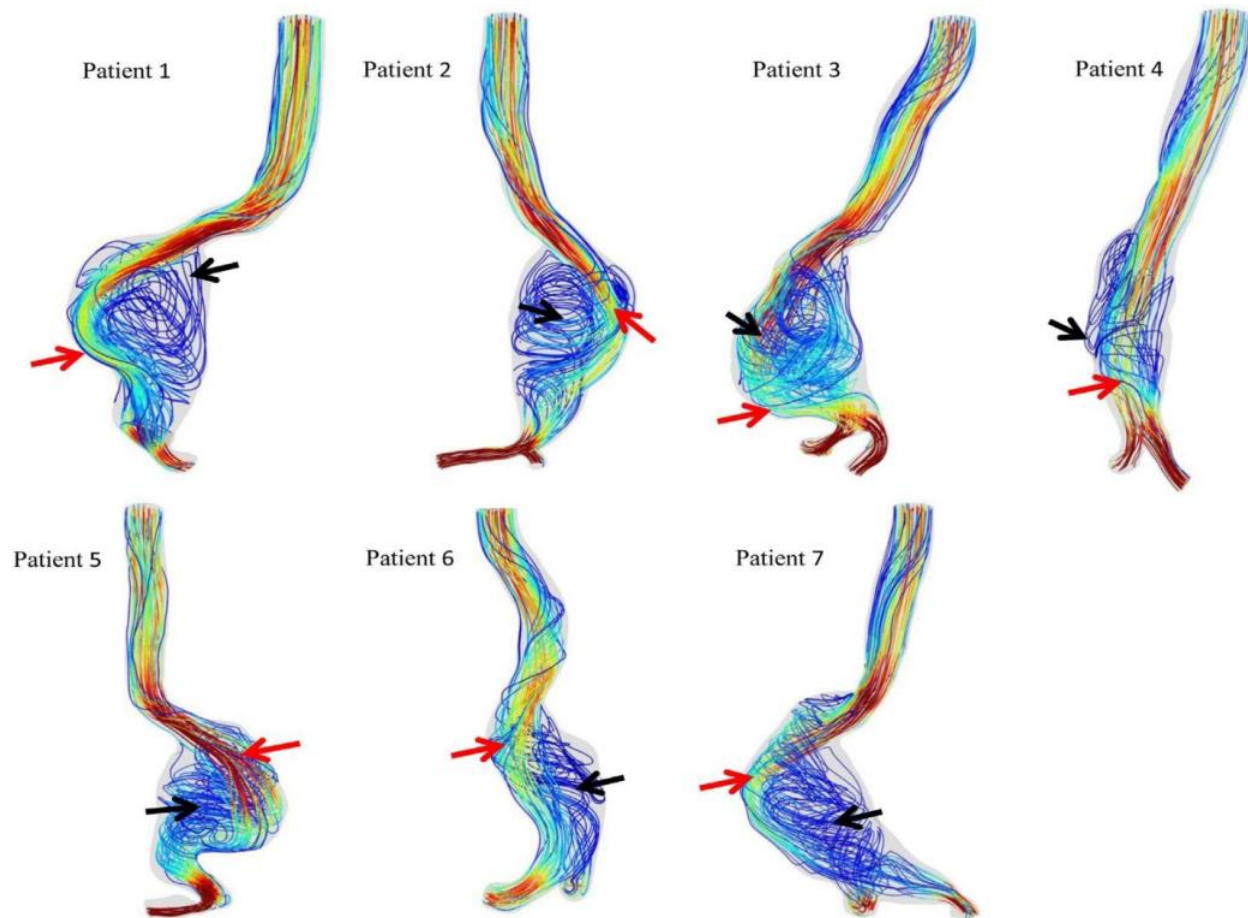


*Figure 25 Black arrows indicate the location of rupture, whereas red arrows indicate the location of dominant flow impingement of aortic wall. Low levels of velocity are represented as blue, high levels of velocity are red [12].*

These findings supported the hypothesis that areas of low shear stress allow blood platelets to aggregate and promote the formation of an ILT. ILTs are normally composed of blood platelets, fibrin mesh, plasminogen erythrocytes, and a few leukocytes [46]. As the disease progresses, erythrocytes lyse and fibrin fibers form. This may contribute to ILT stiffening over time [46]. There are three distinct layers found in most ILTs: the luminal layer, which is composed mostly of fibrin, the medial layer, which appears as a yellowish-white due to the lysing of erythrocytes, and the abluminal layer, which appears as brown due to the degraded matrix [46]. The luminal

layer is responsible for most mechanical properties of the thrombus. It is isotropic, nonlinear, hyperelastic, and stiffer than the other layers [46]. Wilson et al. discussed two distinct types of ILTs: discrete transition and continuous transition. Discrete transition ILTs have three distinct layers, whereas continuous transition ILTs lack distinct boundaries [46].

Wilson et al. held that ILT could promote the AAA inflammatory process through the entrapment, synthesis, storage, and release of different molecules, such as proteolytic enzymes [46]. Wilson et al. reported that thromboses tended to be thinner on average in situations where AAA rupture occurs [46]. They hypothesized that the cause of rupture to be related to the increased proximity of the active luminal layer to the aneurysmal wall [46]. Tanios et al. also found a correlation between ILT and AAA rupture, but in contrast, a decrease in collagen content for patients with thicker intraluminal thromboses resulted in an increased rupture risk [44]. They hypothesized increased level of hypoxia in the aortic wall result in an elevated levels of MMP [44].

Tong et al. investigated changes in ILT histology with respect to age [17]. They identified four phases with distinct characteristics. The first phase (very fresh) was composed of mostly erythrocytes with a small fibrin network, as well as a few leukocytes. The second phase (young) exhibited a growing fibrin network comprised of thinner fibers along with a decreasing percentage of erythrocytes compared to the first phase. The third phase (intermediate) displayed a lack of proteins present, with disrupted erythrocytes and a larger number of thick fibrin bundles. The fourth phase's fibrin network (old) was disrupted, and its small residual proteins were more condensed, as shown in Figure 26 [17].

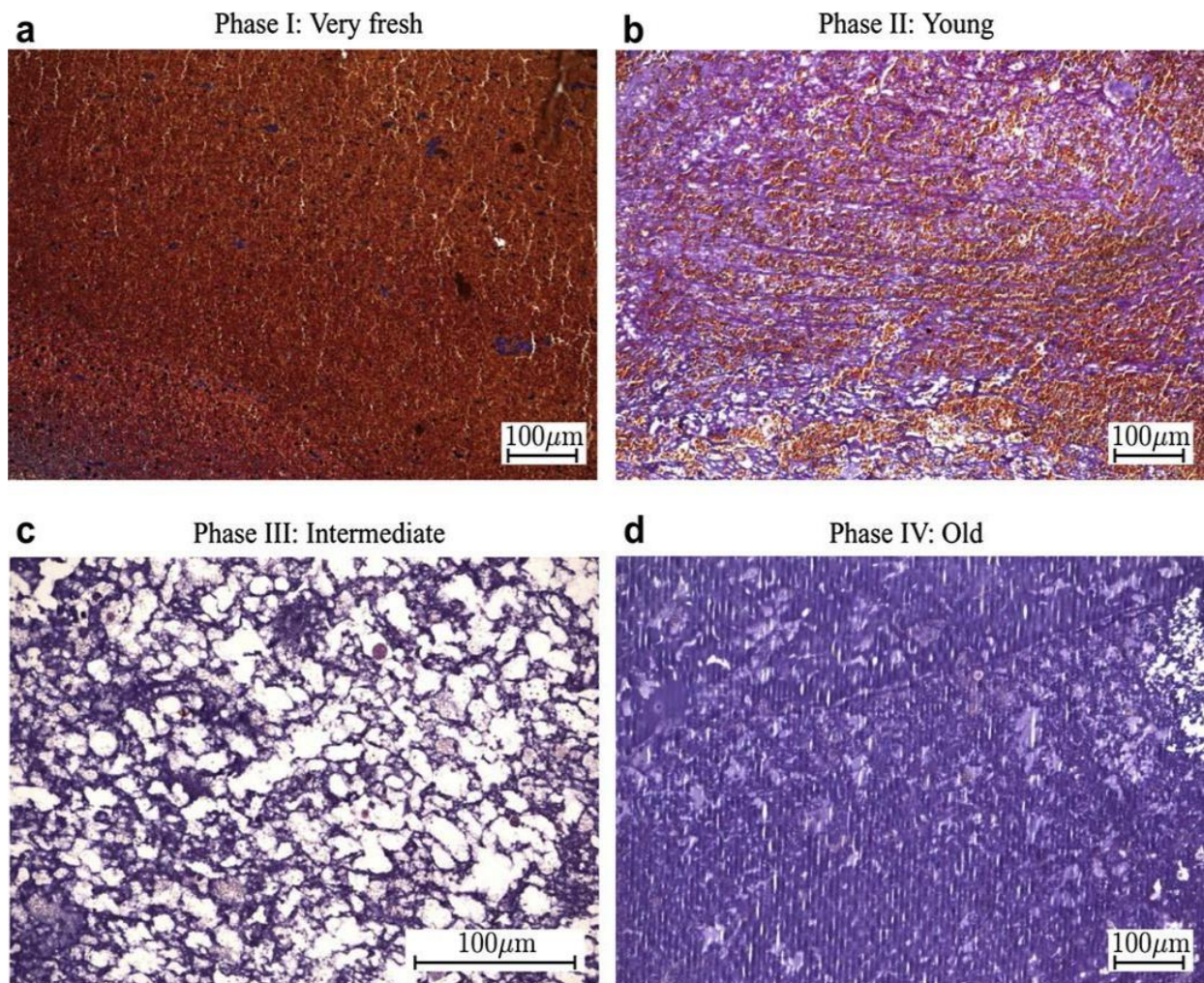


*Figure 26 The four phases of ILT progression [17].*

Tong et al. also performed tensile testing on luminal, medial, and abluminal layers of the ILT, as well as on the underlying aortic wall [17]. Other studies reported isotropy for the luminal layer; however, Tong et al.'s tensile testing indicated that many luminal layers actually displayed significant levels of anisotropy, with a stiffer response in the longitudinal direction. Tong et al. showed that medial and abluminal layers had isotropic behavior [17]. Furthermore, stiffness, luminal anisotropy, and ILT thickness all increased with age. Similarly, with ILT aging, the study also confirmed that the aortic wall exhibited more anisotropy, with a weaker response in the longitudinal direction. Thus, ILT age could potentially be an indicator of rupture risk [17].

The role of the ILT as it relates to stress distribution on the aortic wall remains controversial. Wilson et al. stated that the effects of ILT stress on the aortic wall depend on the attachment of the ILT to the aortic wall, as well as the compressibility of the ILT tissue. If the ILT is completely attached to the aortic wall, then stress reduction will occur. However, partial attachment of the ILT can actually increase stress in certain areas. Not all ILTs are compressible, and compressibility may change over time [46].

Metaxa et al. investigated ILT effect on distensibility measurements of the aortic wall [11]. As mentioned above, ILT attachment, porosity, and compressibility have been shown to affect stress exerted on the aortic wall. Luminal pulse pressure action on the aortic wall with an ILT was measured along with deformation. They used FEA to model that same aneurysm without an ILT and determined the pressure required to cause the same change in volume as the aneurysm with an ILT present. After performing this test, they found that neglecting ILT highly under-estimated wall distensibility values. Distensibility percent error was found to have a linear relationship with ILT volume, as shown in Figure 27 [11].

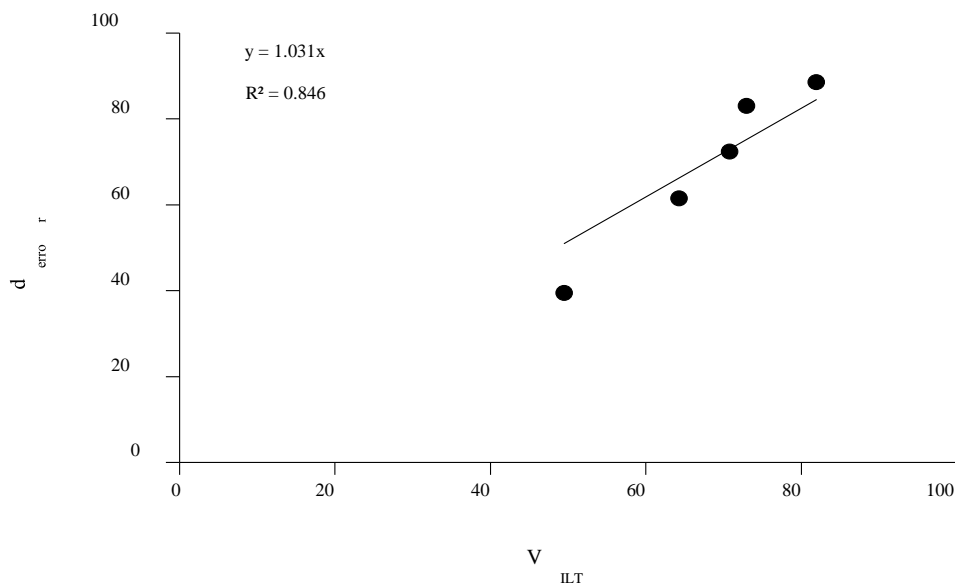


Figure 27 Volume of ILT vs. distensibility error measurement [11].

This work corroborates other studies that support the stress shielding effect of ILTs, such as that of Molacek et al., who reported that ILTs reduce pulse wave propagation [40].

## **2.6. Arterial Pressure and Distensibility**

Gasser et al. tested the ability of four different finite element models (W, PW, WT, and PWT) to predict rupture in AAAs by computing peak wall stress and peak wall rupture risk [16]. The W model assumed no intraluminal thrombus (ILT) and a constant 2 mm thick aortic wall. The PW model also assumed no ILT, but adjusted the wall thickness based on mean arterial pressure. The WT model assumed an ILT and a varying wall thickness between 1.13 and 1.5 mm. The PWT model also assumed an ILT, but adjusted wall thickness based on mean arterial pressure [16]. Models, which accounted for the presence of an ILT, were able to improve prediction accuracy of rupture among diameter matched AAAs. However, these models could not predict rupture in every patient case, and a high standard deviation of peak wall rupture risk was observed, indicative, perhaps, of rupture mechanisms not considered in the finite element (FE) models [16]. Also, this study found that peak wall stress and peak wall rupture risk increased with ILT volume. This indicates that the wall-weakening properties of an ILT overpower its stress shielding properties [16].

Wilson et al. attempted to determine the relationship between elastolytic markers, serum Type-III procollagen aminoterminal propeptides (P3NP), and aortic wall distensibility. Figures 28 and 29 show that as levels of serum-elastin-peptides and elastase-alpha-antitrypsin increased (markers of elastolysis), tissue distensibility decreased [15].



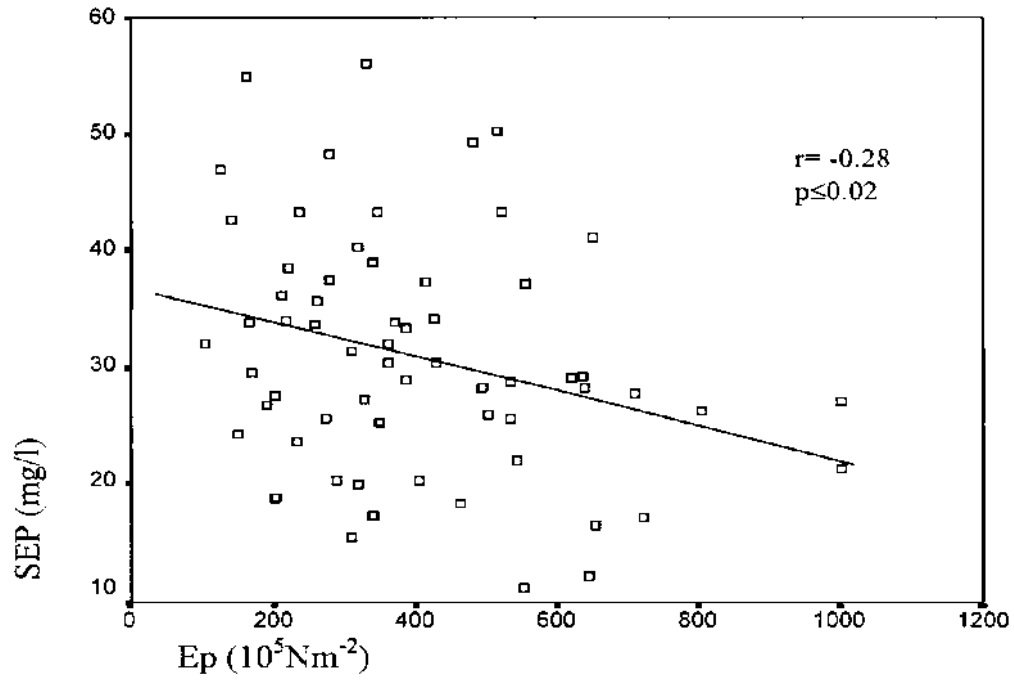


Figure 28 Distensibility as a function of serum-elastin-peptides [15].

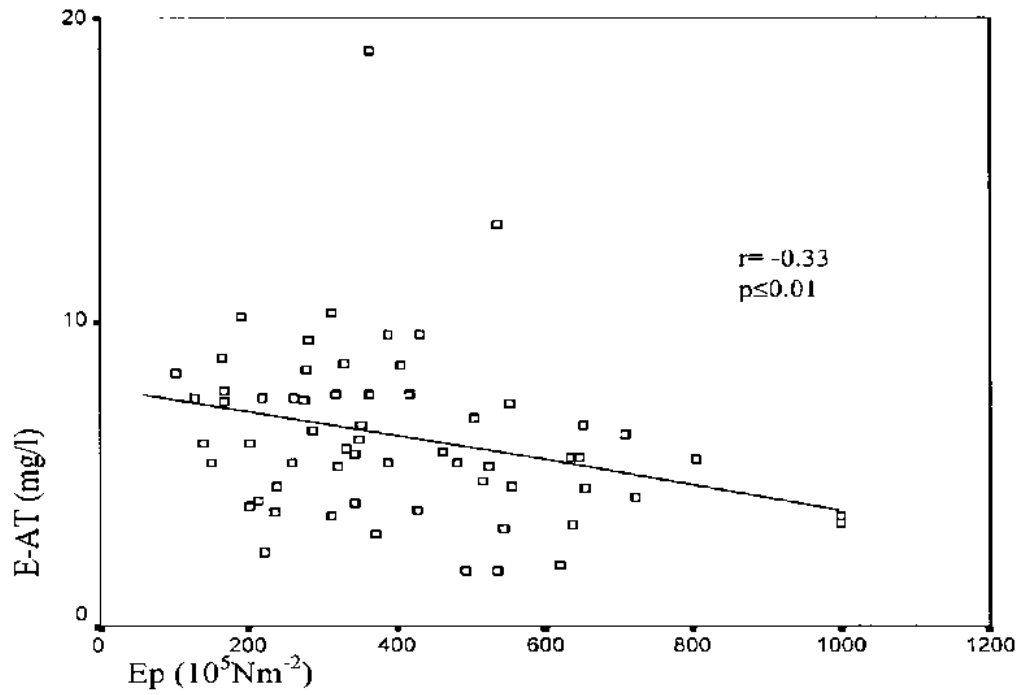
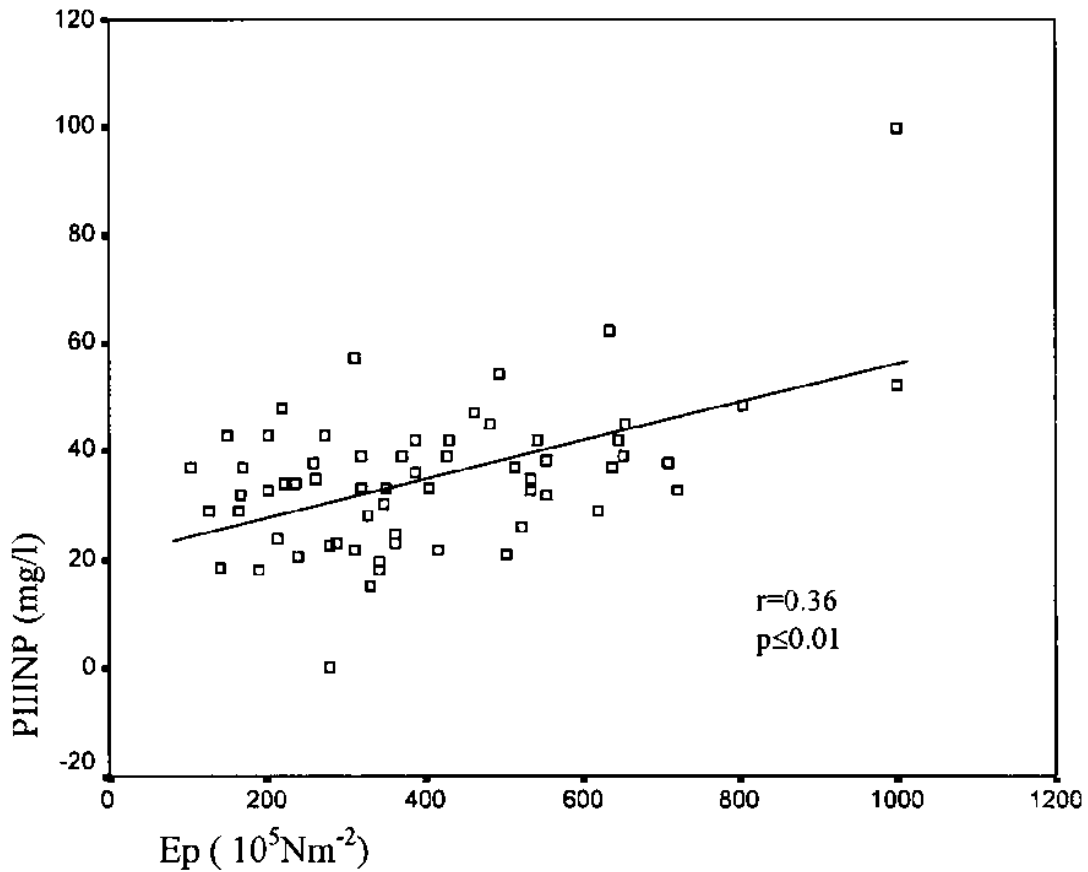


Figure 29 Distensibility as a function of elastase-alpha-antitrypsin [15].

Figures 28 and 29 illustrated that increased levels of serum-elastin-peptides and elastase-alpha-antitrypsin could be indicative of a more distensible AAA. Figure 30 shows that as levels of P3NP increase, distensibility decreases.



*Figure 30 Distensibility as a function of P3NP[15].*

As P3NP is indicative of collagen neosynthesis, it is feasible to assume that higher levels of P3NP would result in a lower level of distensibility. Other studies have found a positive correlation between P3NP levels and AAA expansion and rupture. Wilson et al. hypothesized that, in those cases, the new collagen may be structurally comprised, which would explain the apparent contradiction [15]. The key contribution of this study is that it revealed how increase in distensibility may be indicative of extracellular matrix (ECM) protein degradation [15].

Wilson et al. later carried out a large scale study involving 210 subjects in hopes of determining the effectiveness of AAA wall distensibility as an independent predictor value of rupture risk [21]. Systolic pressure, diastolic pressure, maximum AA diameter, distensibility, and beta stiffness were recorded at a baseline visit, as well as at a follow up visit, for patients with AAA [21]. Results showed that a 10% increase in distensibility corresponded with a 28% increase in rupture risk, whereas a 10% increase in maximal diameter corresponded with a 36% increase in rupture risk [21]. Thus, change in tissue distensibility is comparable to the currently used maximal diameter as a criterion for rupture risk. In addition, increased risk of rupture was associated with gender, specifically females, or with a high diastolic pressure [21]. However, no device existed that would allow the accurate measurement of tissue distensibility in a clinical setting.

A distinct macrophage population has been shown to be present in various vascular diseases [47]. Rao et al. endeavored to provide insight into the formation and structure of the ILT, which is found in most AAAs, (The ILT is divided into three layers: the abluminal, medial, and luminal.) They accomplished this by utilizing histologic staining and immunofluorescent labeling for various markers of macrophages, alpha-smooth muscle actin, CD34, CCD105, fetal liver kinase-A, and collagen Types I and III [47].

They found that the vast majority of nucleated cells were located near the surface of the luminal region of the ILT. This area is referred to as the nuclear stratus. The abluminal and medial layer consisted mostly of fibrin [47]. Histologic staining revealed the presence of collagen in the luminal region of the ILT. Collagen was organized in a laminar arrangement on the shoulder of the ILT and appeared to be less organized and mature in the midsection [47].

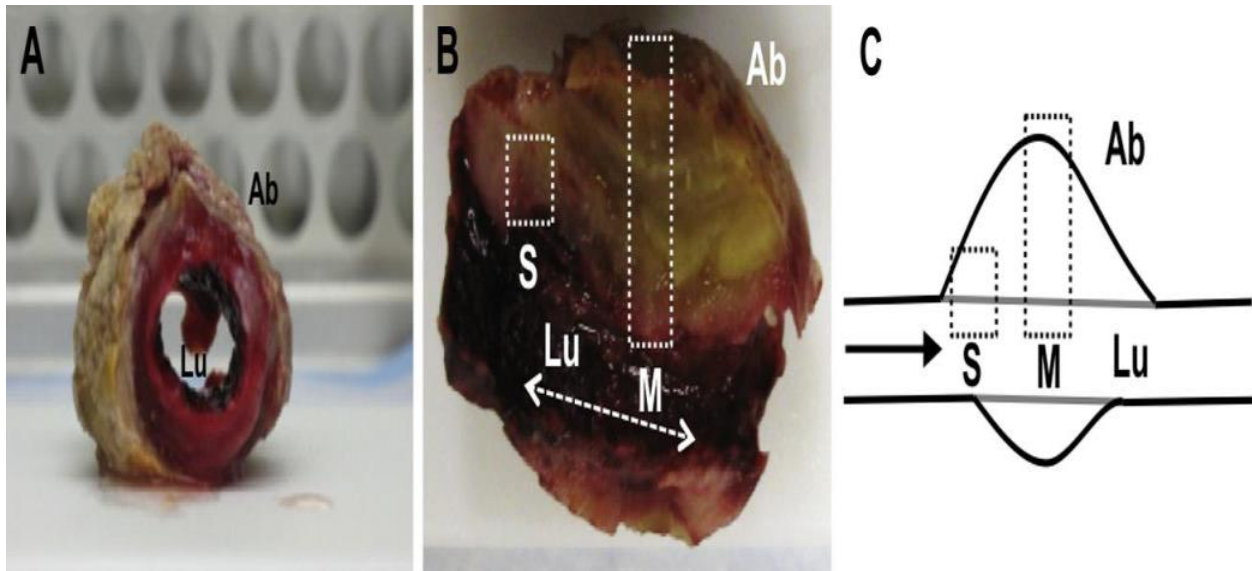


Figure 31 “A and B, Cross sections show the gross morphologic appearance of the shoulder (S), luminal aspect (Lu), abluminal aspect (Ab) and midsection (M) of the intraluminal thrombus (ILT) at time of surgery. Note the layered structure. Samples were cut in two and then further dissected for microscopic investigation. C, a schematic view is shown of the ILT aspects depicted in panel B. The boxes represent the areas sampled” [1, 21].

Further, immunofluorescent labeling revealed the presence of activated macrophages in the luminal region of the ILT. These macrophages expressed a unique phenotype that does not proliferate, suggesting that they occurred through differentiation [47]. Rao et al. hypothesized that these macrophages contributed to ILT formation through the synthesis of collagen, while promoting AA wall degradation through the production of inflammatory mediators and proteases [47].

It has been reported that ILT hemorrhage occurs in 21% of ruptured AAAs compared to 0% of non-ruptured AAAs [1]. Wilson et al. explained this by stating that the hemorrhage of the ILT could significantly increase the aortic wall to exposure of inflammatory biomolecules, resulting in a higher risk of rupture.

## **2.7. Extracellular Matrix Protein Degradation in Abdominal Aortic Aneurysms**

Tanios et al. attempted to draw correlations between the mechanical properties of aneurysmal tissue and its extracellular matrix protein content. After cyclical, sinusoidal, and destructive mechanical testing, Types I and III collagen, as well as total protein content, were found to be increased in areas having higher stress and strain values. These in vivo results are indicative of the biologically adaptive ability of an abdominal aorta to increase collagen synthesis in response to elevated stress [24]. However, Hope et al. reported that this increase in collagen protein content is mainly due to an increase in collagen crosslinks, producing collagen that is, in some cases, structurally compromised [35]. Further testing revealed that higher levels of Type-I collagen, total collagen, and proteoglycans resulted in a higher failure tension for the aortic wall [24]. Mechanical testing from Tanios et al. included a negative correlation between elastin content and aortic diameter, along with an overall decrease in proteoglycan content for AAAs [24]. While collagen content and the amount of collagen degradation are crucial in determining aortic wall strength, Martufi et al. argued that the ultimate factors indicating wall strength are collagen fiber spatial orientation and undulation [29]. Attempts to quantify protein degeneration via quantitative measurement of circulating biomarkers exist. However, these biomarkers are considered nonspecific and may have an etiology from factors other than AAA [35].

Erhart et al. calculated Rupture Risk Index (RRI) using finite element analysis for 15 asymptomatic male AAAs. Areas with the highest and lowest RRI were sampled during surgery, and wall histology was analyzed. Results for individual patients indicated higher levels of smooth muscle cells and elastic fibers in areas of low RRI, while cholesterol and calcified plaque increased in areas of high RRI [48]. However, no correlation was found between high RRI areas and histological degeneration between patients [48].

## 2.8. Collagen Subtypes and Elastin's Content and Orientation

A lack of Type-III collagen has been reported in various aneurysms. Furthermore, a discrepancy was reported in experimental data as to whether overall collagen content increases, decreases, or stays the same in AAAs [9]. Rizzo et al. compared the amounts of Type-I collagen, Type-III collagen, and elastin found in AAAs to healthy AAs [9]. They found that elastin concentration decreased from 11% to 1% in AAAs, while collagen content increased from 24% to 37%. Furthermore, the total amount of collagen plus elastin concentration was nearly equal for healthy AAs, as well as AAAs, as shown in Figure 32 [9].

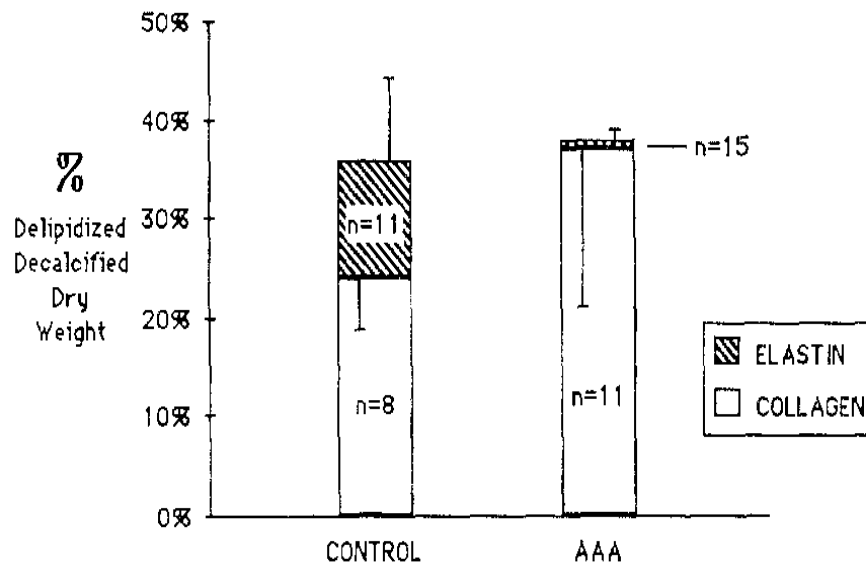


*Figure 32 Total amount of collagen plus elastin concentration in healthy and aneurysmal abdominal aortas [9].*

Rizzo et al. found that calculated circumferential elastin levels decreased by 76%, while calculated circumferential collagen increased by 400% [9]. They hypothesized that this increase in collagen synthesis is a reactionary mechanism brought about in response to lower elastin levels, as well as increased stress, due to the focal widening of the aorta. Additionally, elastin observed

was fragmented and structurally deficient [9]. Histological analysis revealed that, on average, there was no change in the thickness of the aortic wall [9].

Urabe et al. attempted to quantitatively describe collagen strength in young patients with healthy aortas, in elderly patients with healthy aortas, and in patients with AAAs [49]. Collagen fiber orientation was measured, which is thought to be an accurate indicator of collagen fiber strength [49]. Their findings revealed that in all three populations collagen orientation was maintained, but they discovered that collagen fibers were less organized in the infrarenal aorta [49]. This supports the idea that alterations in collagen structure may be related to AAA formation [49]. Imaging of AAA specimens by Urabe et al. revealed that the thickness of collagen fibers increased, along with collagen fiber scarcity [49]. Urabe et al. found no difference in collagen fiber orientation when analyzed by 2D- Fast Fourier Transform among healthy, aged, and diseased abdominal aortas [49]. However, SEM imaging did reveal an apparent increase in collagen fiber disorganization in the aneurysmal wall [49].

Carmo et al. investigated the change in collagen and elastin content, as well as their number of crosslinks in AAAs compared to healthy AAs [50]. As aforementioned, a discrepancy exists in regards to collagen content observed in AAAs, while a consistent report of a decrease in elastin content has been found. The crosslinks of elastin are desmosine and isodesmosine, and a 90% decrease was observed [50]. A change in elastin protein content was also reported at a 90% decrease. 4-hydroxy and 5-hydroxyls (markers for collagen) indicated a 50% and 60% decrease in collagen content, respectively [50]. However, the crosslinks pyridinoline and deoxypyridinoline increased by 350% and 100%, respectively [50]. The increase in crosslinks coupled with a decrease in collagen content occurred due to the continuing formation of crosslinks by aged collagen, which could be prominent in AAAs [50].

## **2.9. Mechanical Testing**

As aforementioned, collagen and elastin are the main structural proteins present in the abdominal aortic wall. Gundiah et al. investigated the mechanical properties of these proteins by degrading collagen and elastin [5]. Porcine aortic specimens were immersed in collagenase for periods of 1 and 6 hours. Specimens were also immersed in elastase for periods of 1 and 4 hours [5]. Ex vivo equibiaxial testing was performed to determine tissue properties compared to control samples. Results from the mechanical testing of the 4-hour treated elastase were discarded as the treatment resulted in the movement of markers caused by a buffer solution below the marker surface [5]. Measurements of the aortic wall revealed that specimens treated with collagenase were thinner than their control counterparts, while specimens treated with elastase were thicker [5].

Mechanical testing revealed that longitudinal segments were stiffer than circumferential segments among control samples. However, this difference in compliance was reduced among the collagenase treated samples [5]. In addition, collagenase treated samples also had an increased linearity on their stress-strain curves [5]. On the other hand, specimens treated with lastase for 1 hour showed a large decrease in compliance. Gundiah et al. found that the 1-hour treatments were sufficient to cause significant changes in tissue properties. Their results are shown in Figures 33 and 34.



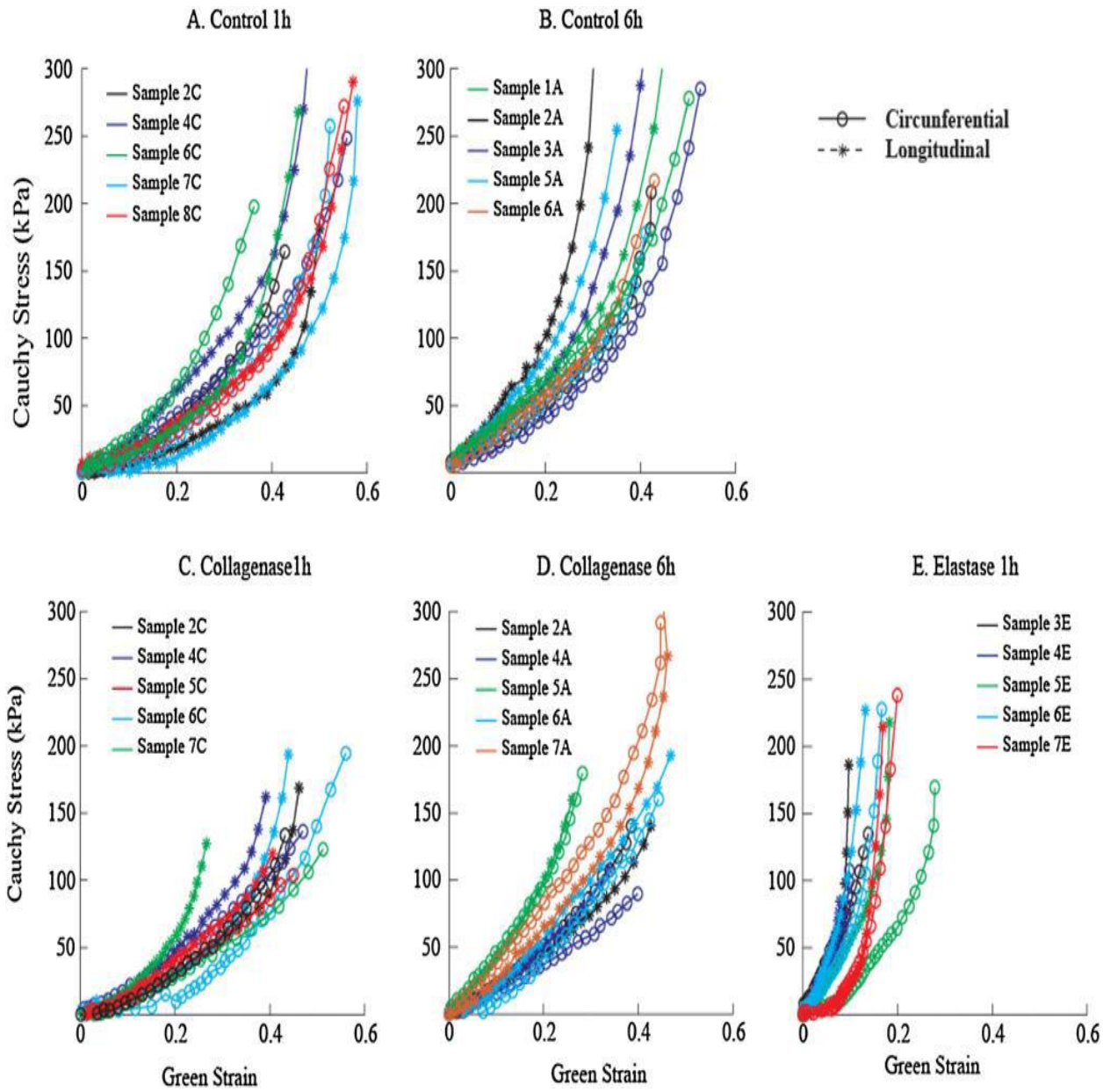


Figure 33 Biaxial mechanical testing of elastin and collagen degraded aortic specimens for circumferential and longitudinal orientations [5].

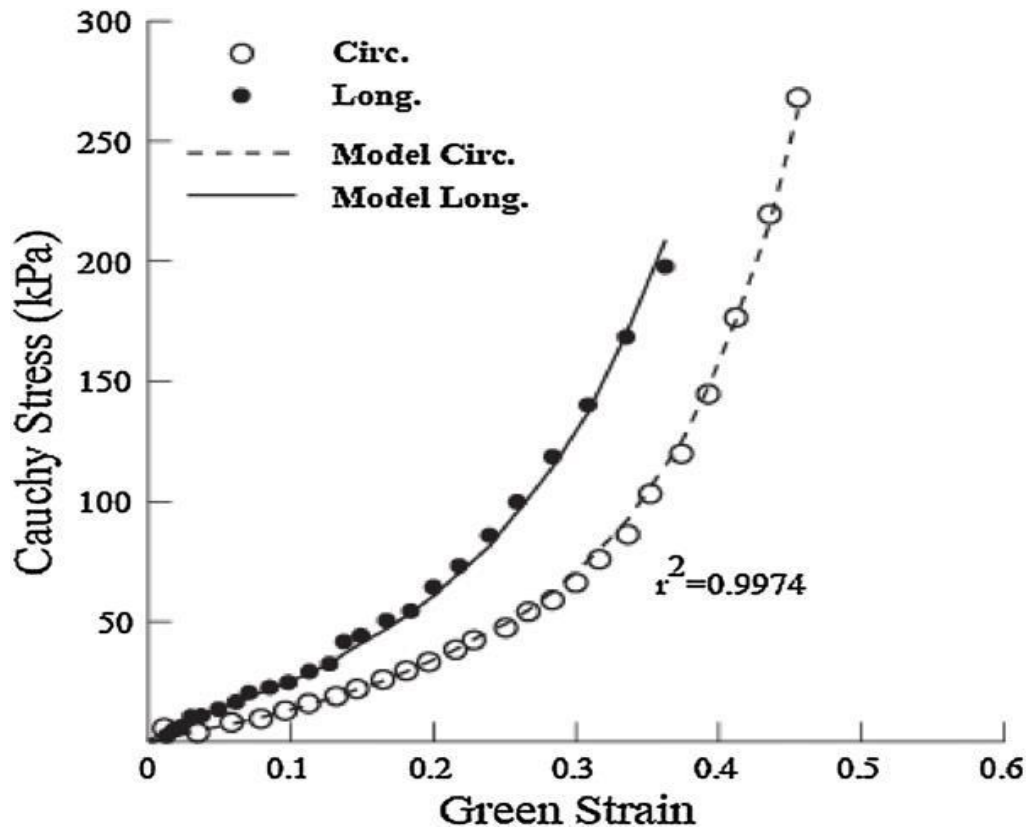


Figure 34 The difference in stiffness between longitudinal and circumferential segments for the control group of AA [5].

Furthermore, Gundiah et al. found that the 1-hour treatment is long enough to cause a significant change in AA wall mechanical properties. Histological treatments revealed that collagen is fragmented in 1- and 6-hour collagenase treated specimens, and that collagen fiber density dropped substantially with the 6-hour treatment [5]. Elastin appeared to be disorganized in the 1- and 4-hour elastase treated specimens. Also, the 4-hour elastase treatment resulted in collagen fiber increase. In summation, treatment of tissue with elastase increased stiffness in the longitudinal and circumferential directions. However, treatment of specimens with collagenase resulted in a decrease in tissue stiffness [5]. Collagen not only provides tissue with strength, but is also an important causal factor for tissue's non-linear behavior and anisotropy [5]. Furthermore, after 6 hours of collagenase treatment, collagen fiber density decreased significantly compared to the control specimen [5].

## 2.10. Computational Methods

Peak wall stress can be estimated using Finite Element Method (FEM), a computational method frequently used to calculate peak wall stress in patient-specific cases. To date, many FEMs have been created under the assumptions of varying aortic properties [4, 8, 10, 11, 16]. Some assume elastic or viscoelastic tissue behavior, isotropic or anisotropic properties, uniform or non-uniform wall thickness, and with or without considering ILT effects [7].

Geest et al. used FEM to evaluate ruptured and electively repaired AAAs [7]. CT scan images of the AAAs reconstructed the geometry of the AAA. The new model included wall stress and strength distribution. The ratio of wall stress to wall strength was used to introduce the term rupture potential index (RPI). Consequently, RPI can be used as a quantitative measurement of the potential for rupture. As RPI approaches 1, rupture becomes imminent [7].

Gasser et al. evaluated FEM as a predictive tool for assessment of AAA rupture potential and used A4research diagnostic software to reconstruct and segment the geometry of AAA from CT scans [16]. Four FEMs were tested. First, the W model assumed a constant wall thickness of 2.0 mm and no ILT. Second, the PW model assumed varying wall thickness that changed proportionally with mean arterial pressure (MAP).  $MAP = P_d + (1/3)*(P_s - P_d)$ , where  $P_s$  and  $P_d$  are systolic and diastolic pressures, respectively. Third, the WT model assumed ILT volume and varying wall thickness ranging from 1.13 to 1.5 mm. Fourth, the PWT assumed identical conditions as the WT model with wall thickness adjustments according to MAP. They concluded that the presence of ILT in the model significantly affected the tissue biomechanics and rupture risk assessment. In addition, the inclusion of ILT and variable wall thickness improves the accuracy of prediction from biomechanical simulations. Across available date, none of the models used could explain rupture in all AAAs [16].

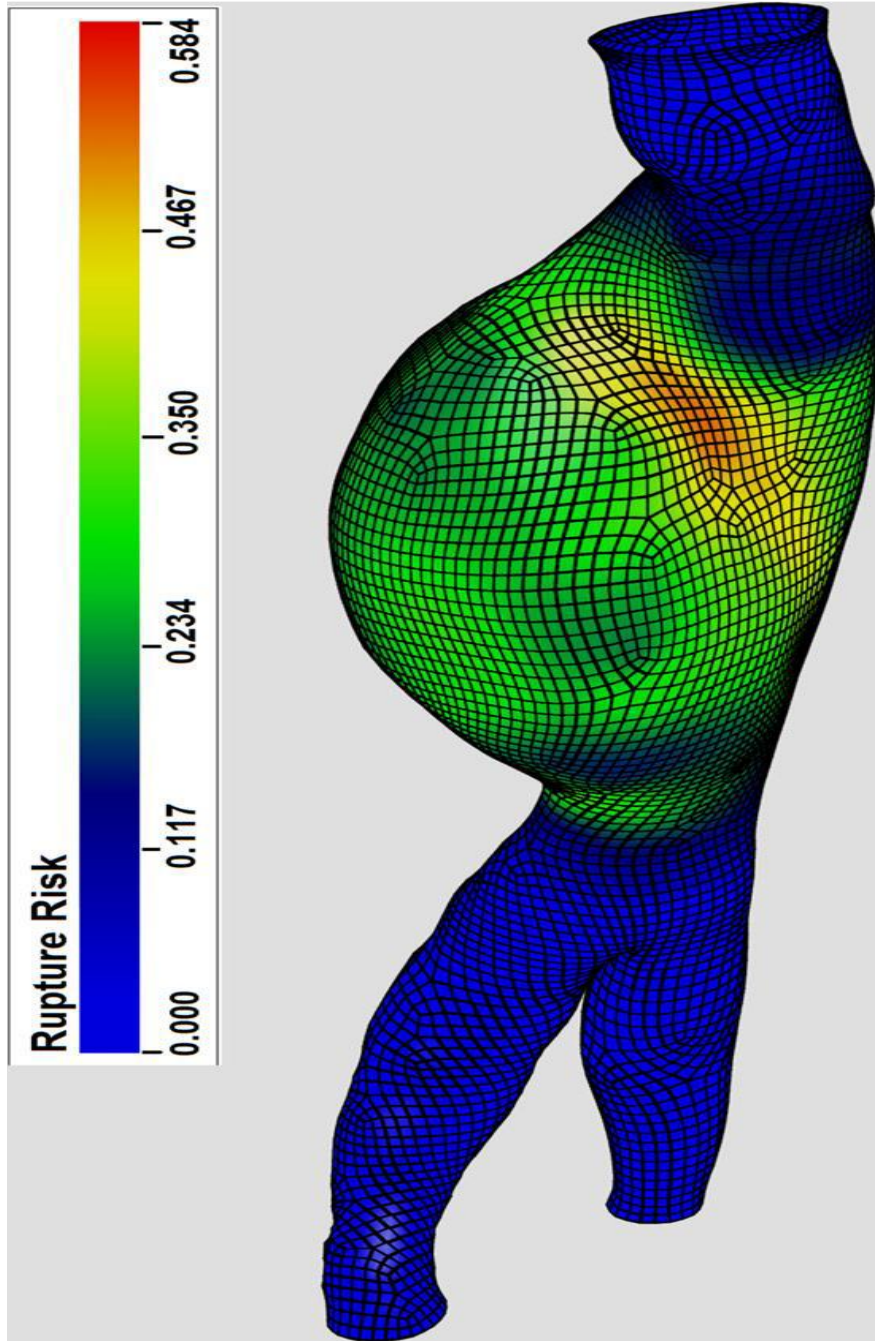


*Figure 35 RPI prediction of rupture risk for a patient-specific aneurysm using FEM with 28000 nodes [7].*

Zelaya et al. suggested a linear model in order to improve the efficiency, effectivity, and ease of AAA wall stress computations [2]. As a result, such models can be used as clinical tools for patient-specific wall stress assessments. Figure 36 displayed three models developed to improve the relative accuracy of the linear approach used in computing AAA wall stresses: a reference model, a conventional model, and a proposed linear model [2].

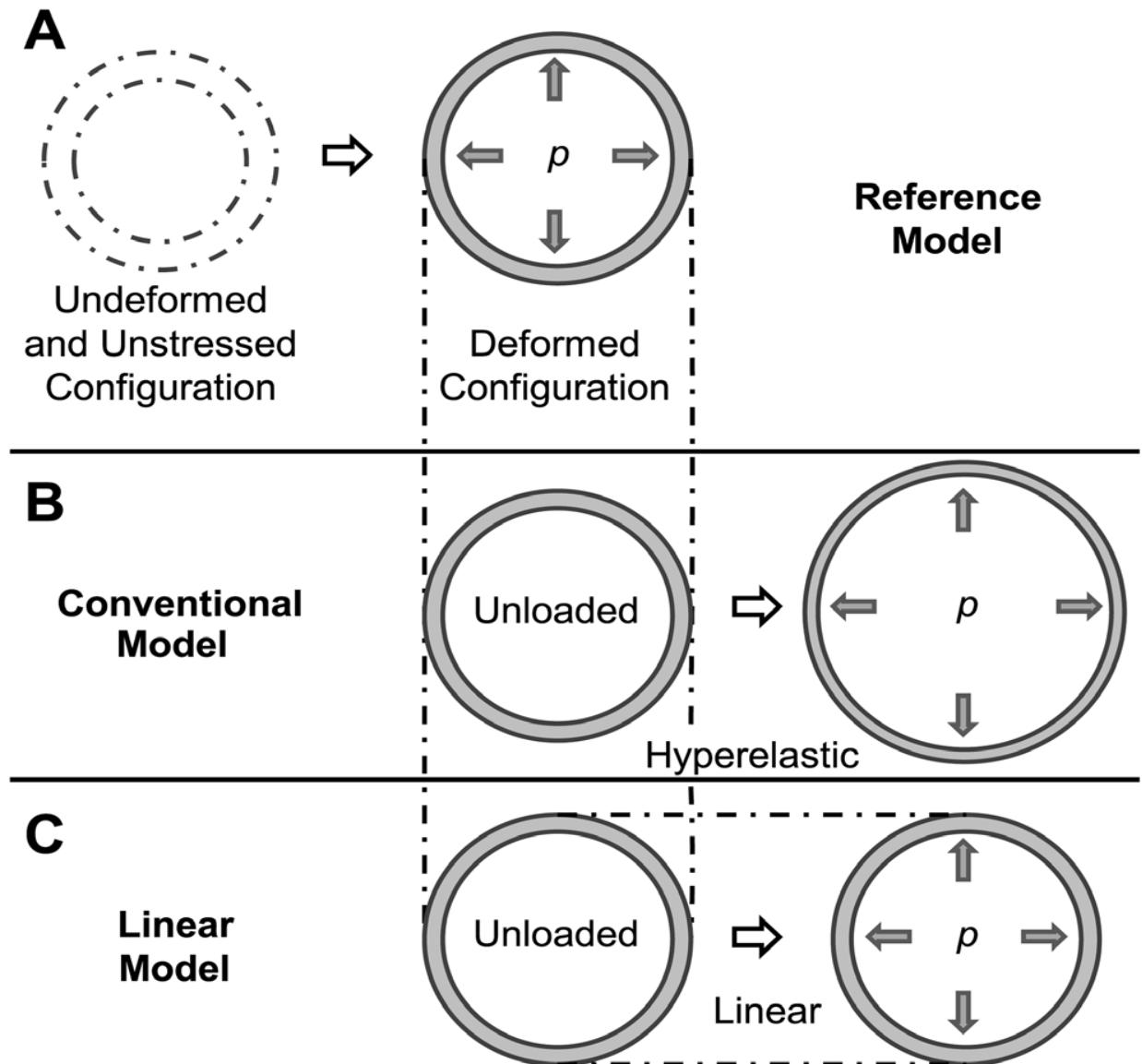


Figure 36 Three models were employed in the study. The deformed configuration of the reference model was the initial configuration for conventional and linear models. For A & B models, the walls are hyperelastic with nonlinear behavior. For (C) model, the walls are linear elastic, with infinitesimally small deformations and strains [2].

For all models proposed, the equations of equilibrium were used and solved with boundary conditions as shown in the equilibrium equation below [2]:

$$\nabla \cdot \boldsymbol{\sigma} = \mathbf{0} \quad \text{in } \Omega \quad (2.2)$$

where  $\boldsymbol{\sigma}$  is the Cauchy stress tensor,  $\Omega$  is the body domain in the deformed configuration.

Boundary conditions are shown in equations 7.

$$\boldsymbol{\sigma} \cdot \hat{\mathbf{n}} = -p\hat{\mathbf{n}} \quad \text{on } \Gamma_l \quad \text{and} \quad \boldsymbol{\sigma} \cdot \hat{\mathbf{n}} = \mathbf{0} \quad \text{on } \Gamma_o \quad (2.3)$$

Where  $\hat{\mathbf{n}}$ , a unit vector, is normal to the wall surface;  $p$  is the intraluminal systolic pressure, which is 120 mmHg (0.016N/mm<sup>2</sup>);  $\Gamma_l$  is the lumen surface of the deformed configuration;  $\Gamma_o$  is the outer surface of the deformed configuration.

Equation 8 is an energy density function,  $W$ , for almost incompressible, homogenous, and isotropic AAA wall properties:

$$W = \alpha(\mathbf{I}_B - 3) + \beta(\mathbf{I}_B - 3)^2 + \gamma(\mathbf{I}_B - 3)^3 \quad (2.4)$$

where  $\alpha$ ,  $\beta$ , &  $\gamma$  are coefficients that denote the properties of the tissue;  $\mathbf{I}_B$  is the first invariant of the left Cauchy-Green Tensor  $\mathbf{B}$  ( $\mathbf{I}_B = \text{tr}\mathbf{B}$ ) with  $\mathbf{B} = \mathbf{F}\mathbf{F}^T$ ;  $\mathbf{F}$  is the deformation gradient tensor.

Equation 9 represents a constitutive relation for nonlinear material.

$$\boldsymbol{\sigma} = -H\mathbf{I} + 2 \frac{\partial W}{\partial \mathbf{I}_B} \mathbf{B} \quad (2.5)$$

where  $\mathbf{H}$  is the hydrostatic pressure, and  $\mathbf{I}$  is the identity tensor.

The following assumptions were made for the linear model: almost incompressible, linear and elastic material, and high Young's modulus. The constitutive relation is expressed in equation 10.

$$\boldsymbol{\sigma} = \mathbf{C}\boldsymbol{\varepsilon} \quad (2.6)$$

where  $C$  is the stiffness tensor; for an isotropic material,  $C$  depends on  $E$  and Poisson's ratio  $\nu$ ;

$\boldsymbol{\varepsilon}$  is the infinitesimal strain.  $E=8.4 \cdot 10^9 \text{ N/mm}^2$  and  $\nu = 0.4999$  were used for the linear model [2].

Initial configurations and material properties were different among the three models. The initial configuration in the reference model was the unstressed and unloaded configuration of the tissue. For the conventional and linear models, the initial configuration is the deformed configuration of the reference model [2]. Figure 37 shows a thick wall cylindrical model with applied internal pressure. No stress or load was applied in the undeformed configuration. However, internal pressure exists in the deformed configuration [2].

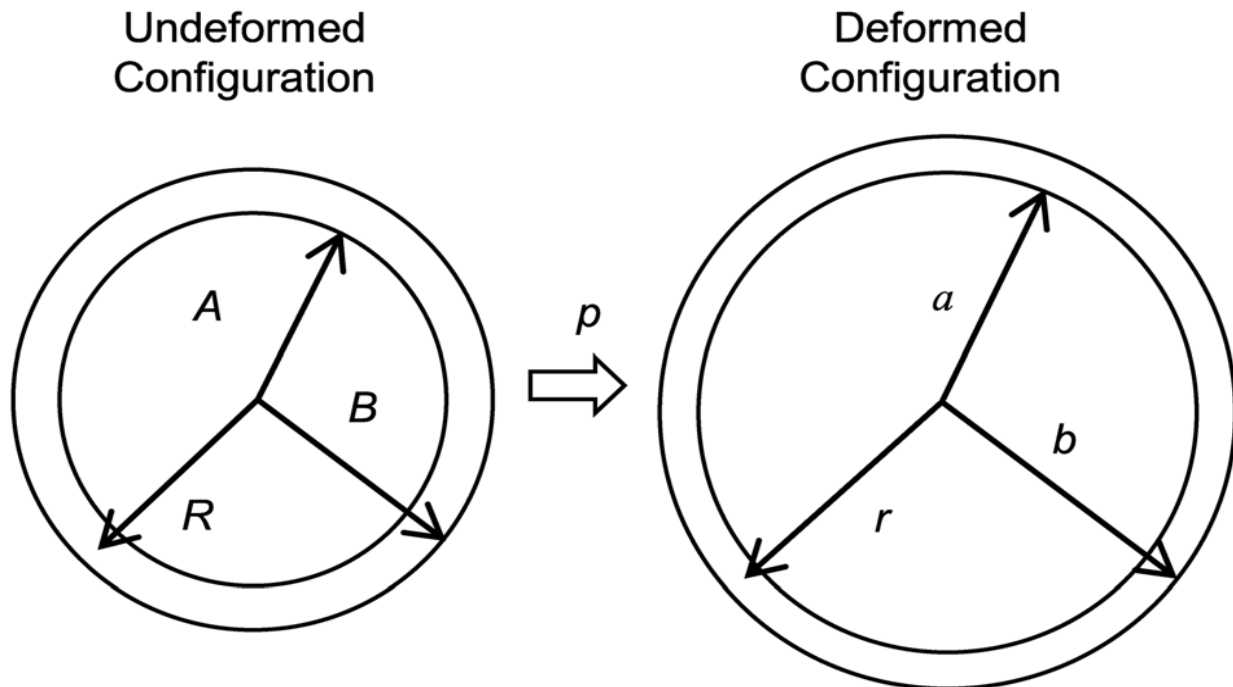


Figure 37 shows the deformed configuration once an internal pressure,  $p$ , was applied.  $A$  represents the internal wall radius,  $B$  represents the external wall radius, and  $R$  represents the radial wall coordinate. The  $a$ ,  $b$ , and  $r$  represent the same, but in the deformed configuration [2].

Figures 38 and 39 show effective stress results obtained using the three different models and the relative difference in effective stress between the linear and conventional models:

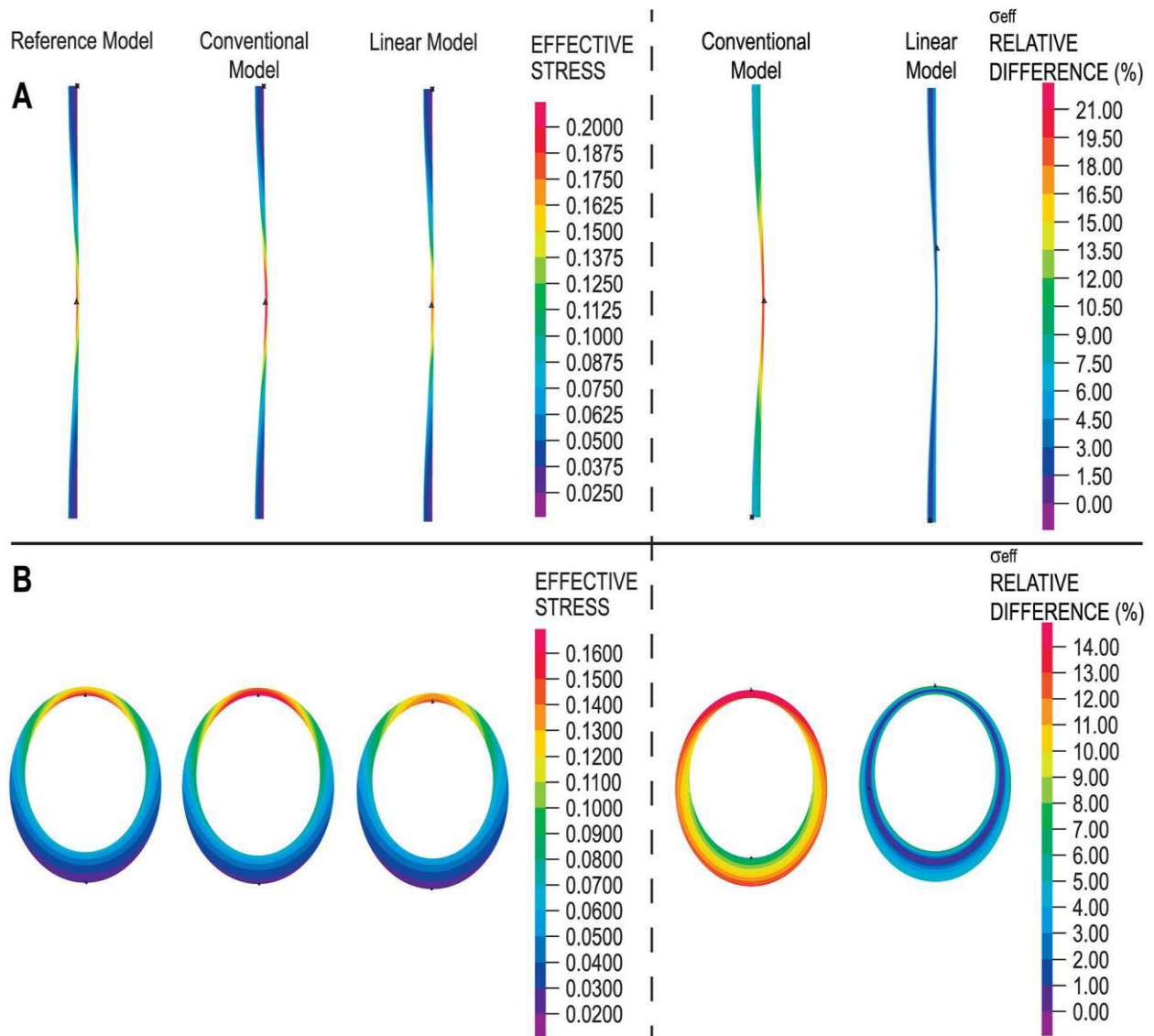


Figure 38 shows the effect of variable wall thickness on wall stress distributions using all three models. A is an axisymmetric model with longitudinally varying wall thickness, where B is a plane strain model with circumferentially varying wall thickness [2].



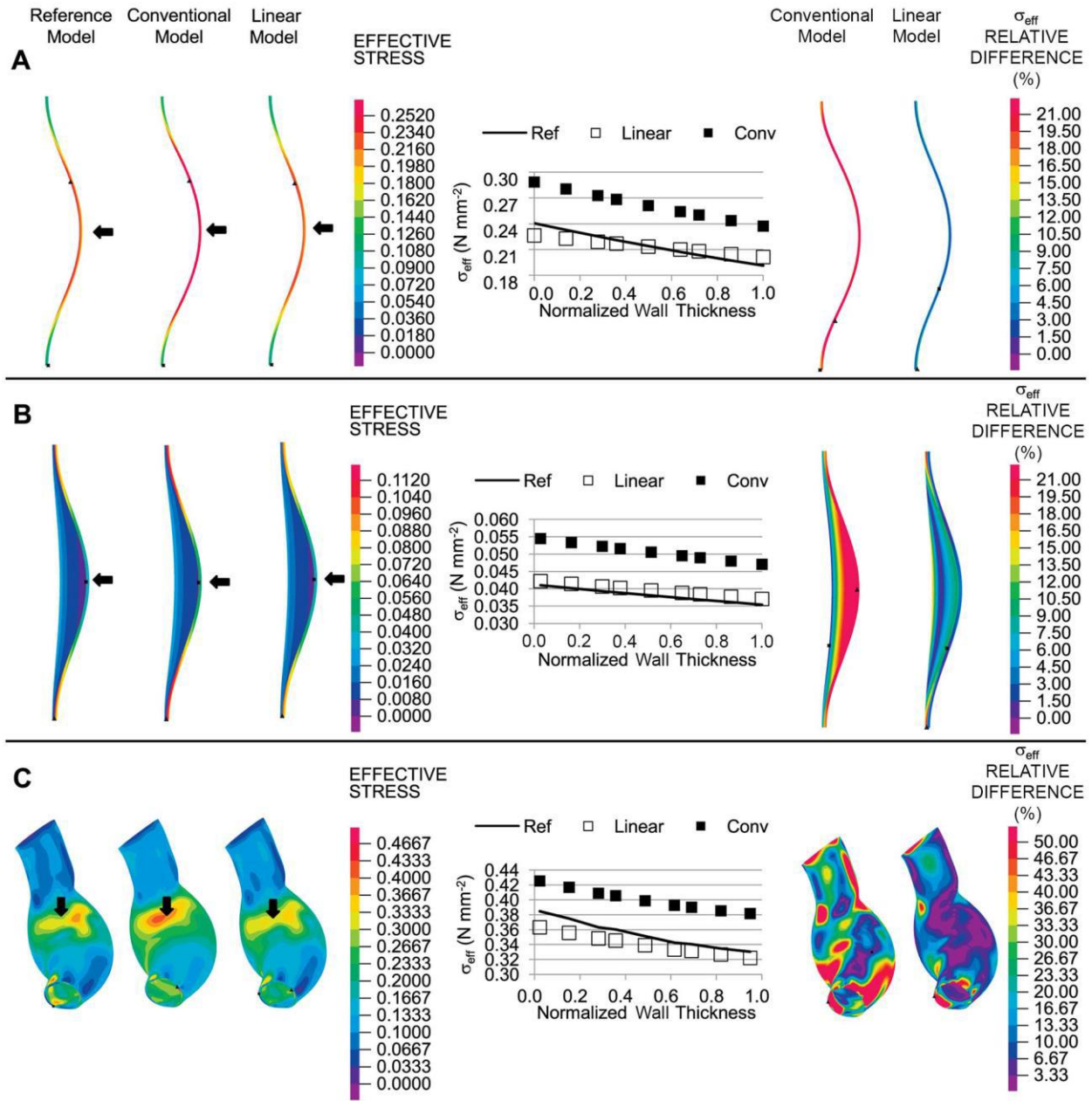


Figure 39 shows the effect of different geometries of AAA on wall stress distributions using all three models. A is an axisymmetric model, B is an axisymmetric model with ILT, and C is a patient-specific model [2].

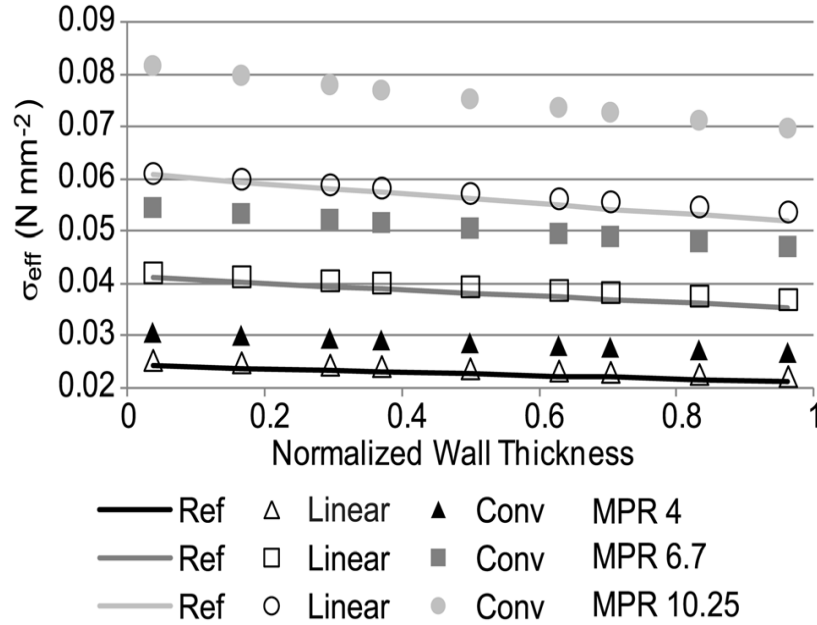


Figure 40 shows the effect of wall/thrombus material property ratio (MPR) on the effective stress distributions [2].

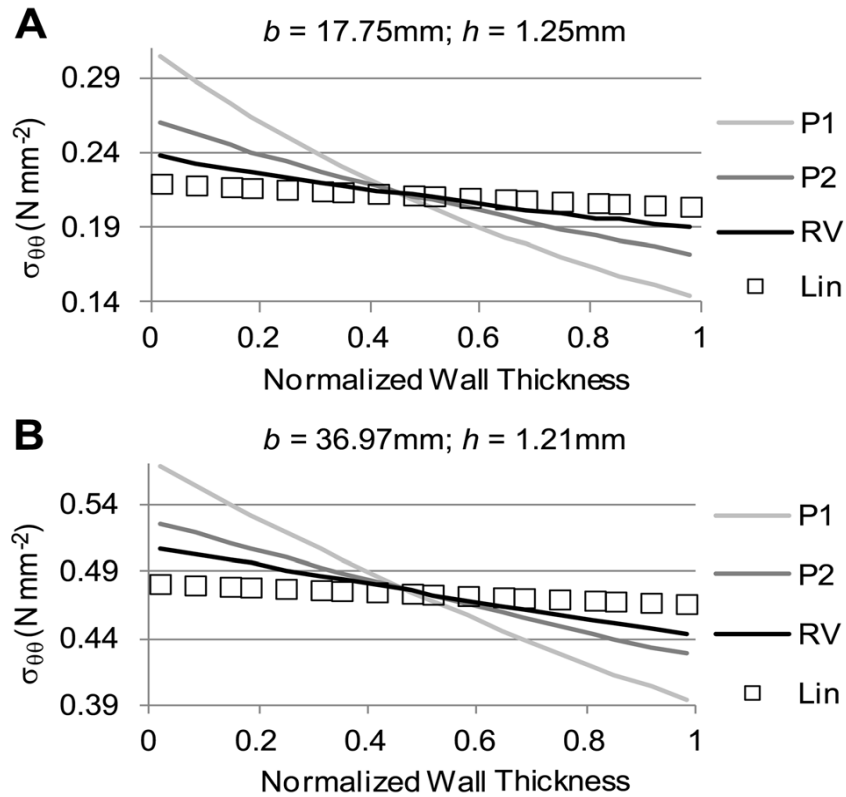


Figure 41 shows a comparison of circumferential stress distributions using the tissue property values (RV, P1, & P2), and results using the linear model (Lin). (A) is a small aneurysm, where (B) is a bigger aneurysm [2].

Zelaya et al. concluded that their linear approach can accurately approximate wall stresses for various geometries with different material properties, which makes their model effective to use as a clinical tool for measuring and analyzing patient-specific wall stresses [2]. When comparing the linear model with reference model, Figure 38, the linear model demonstrates closer approximations of stress values than the reference model. Thus, Zelaya et al. suggested that the linear approach could be a more accurate tool to measure wall stresses and effects of wall thickness than the conventional model [2].

Also, Zelaya et al. accounted for curvature in their models. They constructed axisymmetric, curved wall aneurysms subjected to internal pressure at the interior [2]. Higher stresses were found at walls with higher curvature, Figure 38A. In addition, the effect of ILT on wall stress was studied, Figure 39B. The effect of complex curvature and asymmetry in an aneurysm was assessed, considered patient-specific AAA, and applied the models to approximate wall stresses, Figure 39C. In all of the aforementioned cases, the linear model had closer approximations than the reference model. This finding indicated that the linear model is a more accurate model in computing wall stresses for various geometries of AAA and provides desirable physiological wall stress profiles across the spectrum of wall thicknesses [2].

Realistically, aneurysms are not usually symmetrical. It is important that modeling methods account for that fact. Considering asymmetry in modeling methods will allow us to compute more accurate stress and strain values, and, ultimately, improve the assessment of prediction of rupture site in the aneurysm.

The expansion of AAA's wall is not usually symmetrical over time. Most aneurysms exhibit asymmetric and complex geometrical shapes. The bulge shape and diameter of the AAA may have an effect on wall strength and risk assessment [4]. Vorp et al. focused on studying AAA wall stress distribution due to the effects of AAA bulge and diameter, as shown in Figure 42 [4].

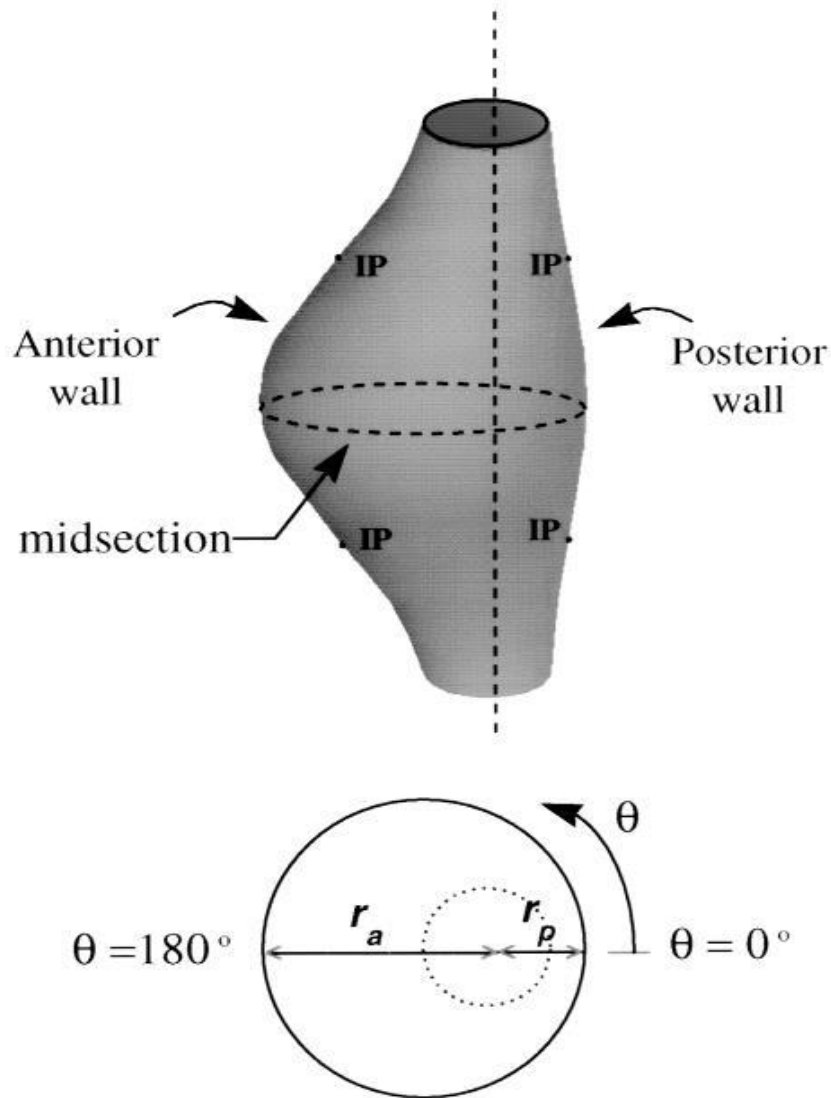
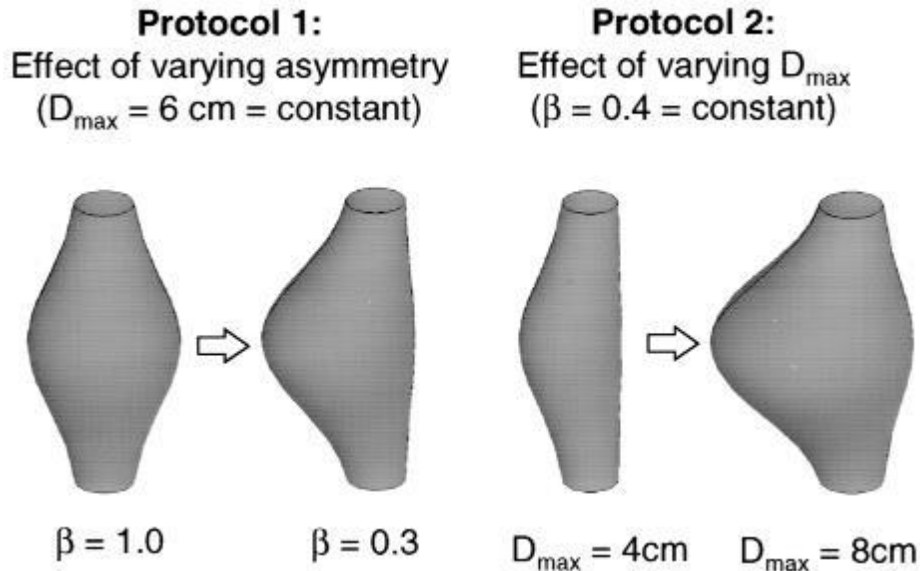


Figure 42 shows a 3D model of an AAA, where  $r_a$  is the maximum anterior wall dimension, and  $r_p$  is the maximum posterior wall dimension. The vertical dashed line passes through the center of the undilated inlet and outlet. Inflection points (IP) indicate the points at which the concavity of the wall changes from outward to inward and vice-versa [4].

Vorp et al. constructed a hypothetical 3-D aneurysm using ANSYS, a computer software. Varying wall thickness was not considered in the study, since the main focus was on symmetry, asymmetry, and maximum diameter of the bulge [4].



*Figure 43 shows two cases, varying the asymmetry under constant maximum diameter (fusiform and saccular aneurysms) and varying maximum diameter [4].*

Each modeled aneurysm was 12 cm long ( $z = 0 - 12$ , superior and inferior end, respectively), where  $z = 6 \text{ cm}$  is the midsection. Wall thickness of the constructed aneurysms remained constant and uniform at 1.5 mm,  $D_{max} = r_p + r_a$ , and  $\beta = r_p/r_a$ . The application of finite element techniques was utilized. Each aneurysm was discretized into small linear elastic, quadrilateral shell elements. The total number of elements ranged from 3200 to 3800 depending on the structure of each constructed aneurysm [4]. The wall tissue was assumed to be incompressible; the applied internal pressure was 120 mmHg ( $1.6 \text{ N/cm}^2$ ); the shear stress was neglected due to its small values compared to large wall stress values; the elastic modulus of the tissue was  $E = 500 \text{ N/cm}^2$ , and the Poisson's ratio was  $\nu = 0.49$  [4].

The results of the 3D analysis of wall stress distribution for a total of 10 constructed aneurysms (5 with constant maximum diameter and 5 with constant symmetry) are shown in Figure 44.

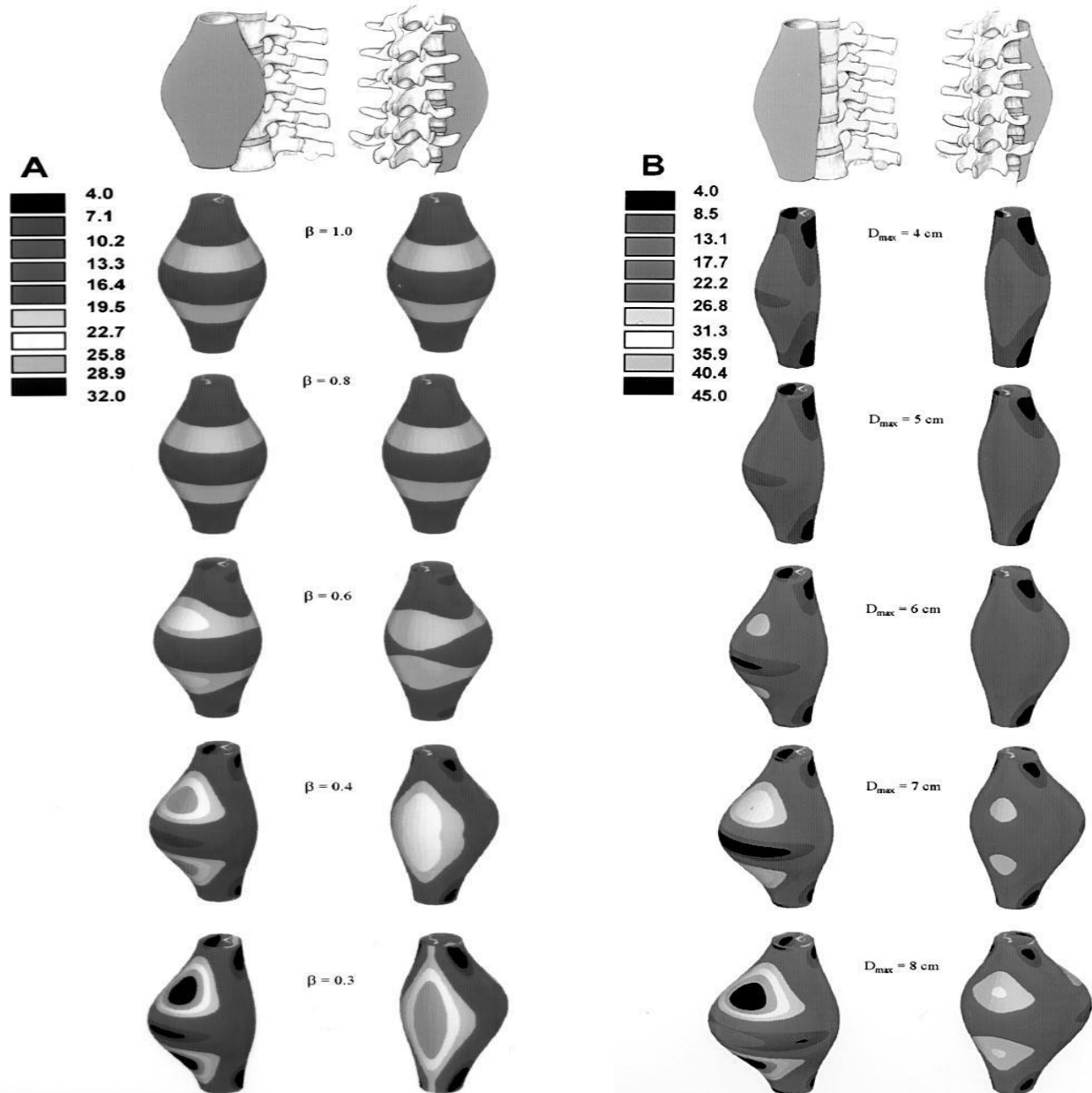
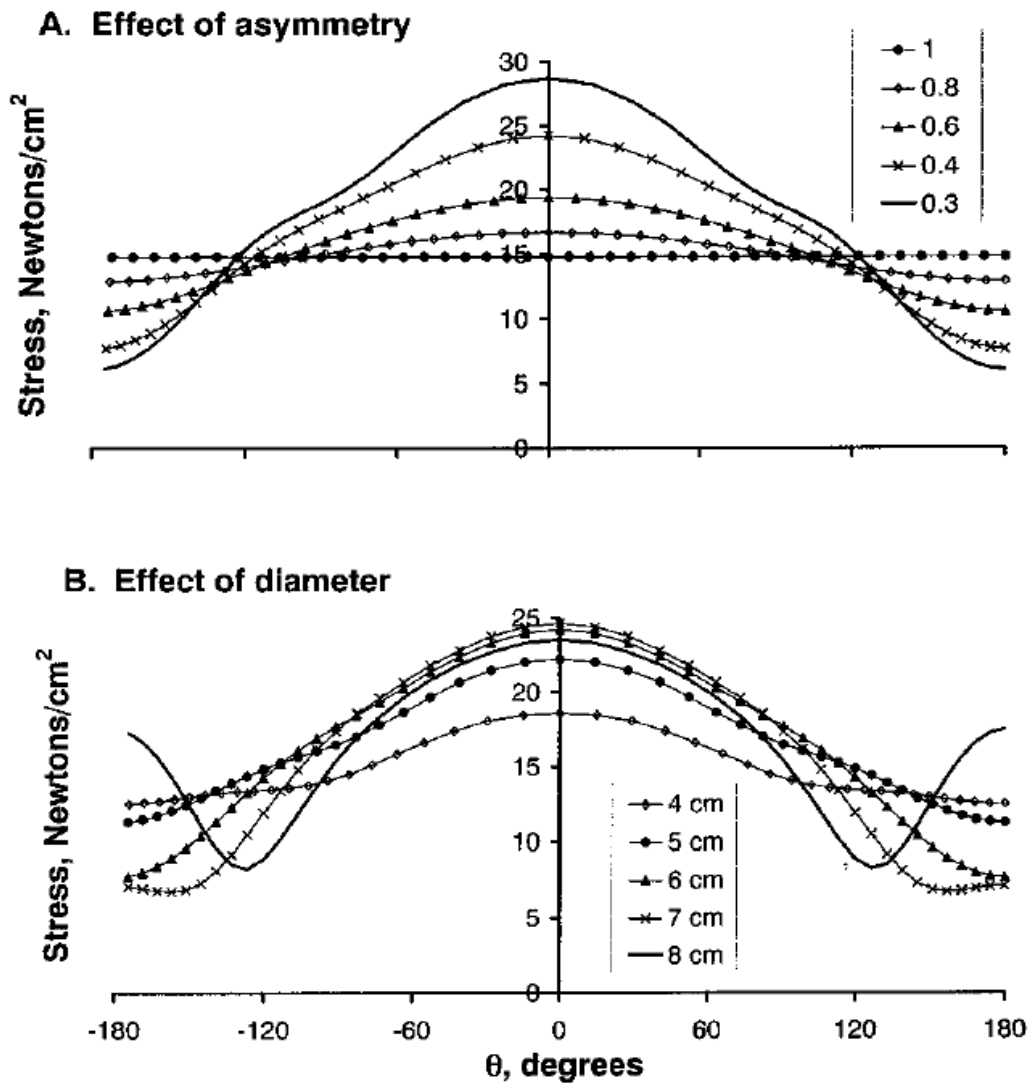


Figure 44 shows distribution of mechanical wall stress for all 10 aneurysms. For A, the symmetry is varied, and for B, the maximum diameter is varied. The left columns of A and B show the anterior surface of the aneurysm, and the right columns of A and B show the posterior surface of the aneurysm. The anatomic reference is shown above where the aneurysm is attached to the vertebrate column. The color scales on the side represent the magnitudes of wall stress (in  $N/cm^2$ ) [4].

The effects of asymmetry and maximum diameter on the circumferential and longitudinal wall stress distributions at midsection, anterior, and posterior surfaces are shown in Figures 45-47 [4].

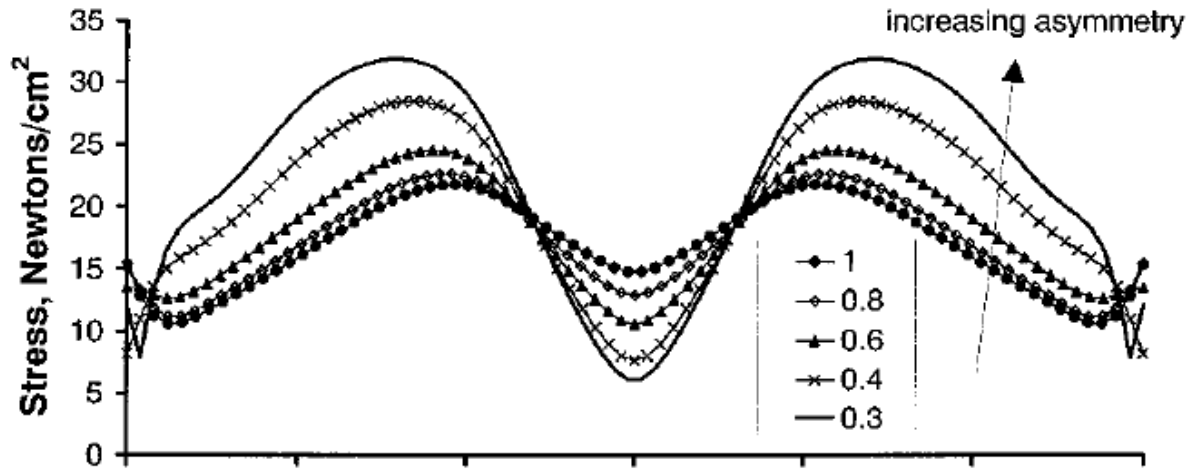
### Circumferential Distribution of Wall Stress at Midsection



anterior surface                      posterior surface                      anterior surface  
 Figure 45 shows A, effect of symmetry, and B, effect of maximum diameter on the circumferential wall stress distribution starting from the posterior position and ending in the anterior position along the angle theta of the midsection of each aneurysm [4].

# Longitudinal Distribution of Wall Stress on Anterior Surface

## A. Effect of asymmetry



## B. Effect of diameter

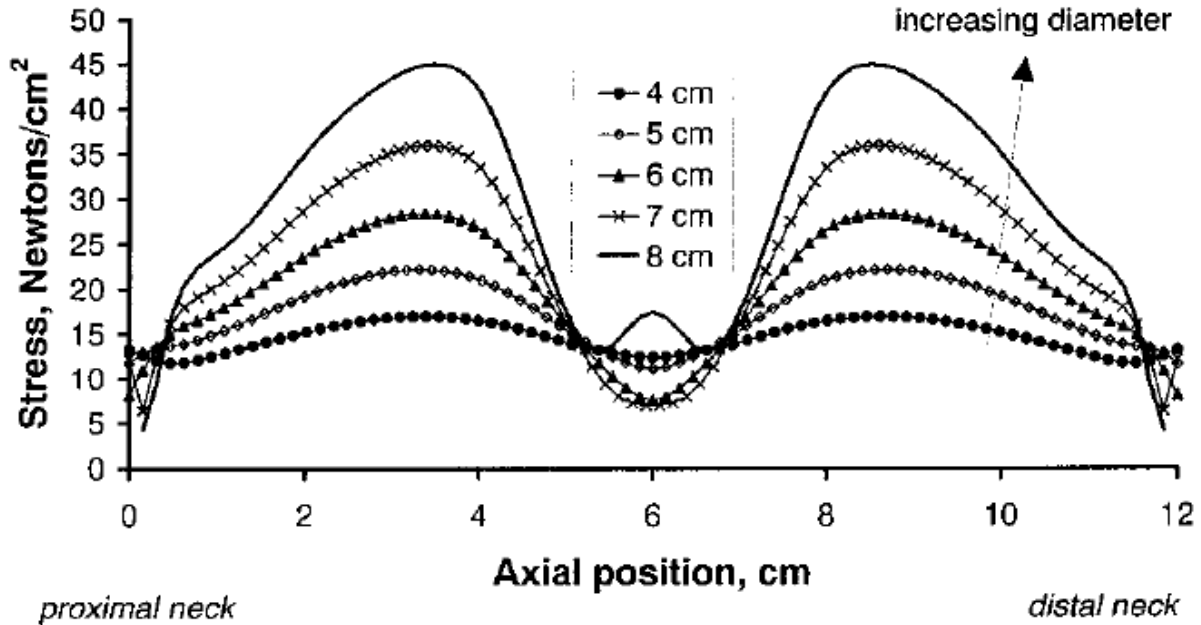
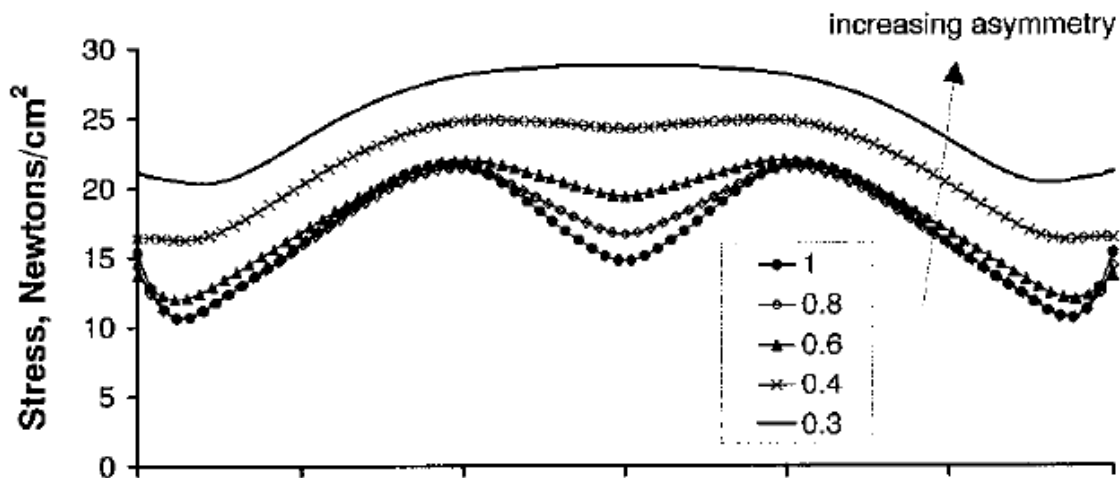


Figure 46 shows A, effect of symmetry, and B, effect of maximum diameter on the longitudinal wall stress distribution on the anterior surface, starting from  $z = 0$  cm, superior end, to  $z = 12$  cm, inferior end, and  $z = 6$  cm, midsection [4].



## Longitudinal Distribution of Wall Stress on Posterior Surface

### A. Effect of asymmetry



### B. Effect of diameter

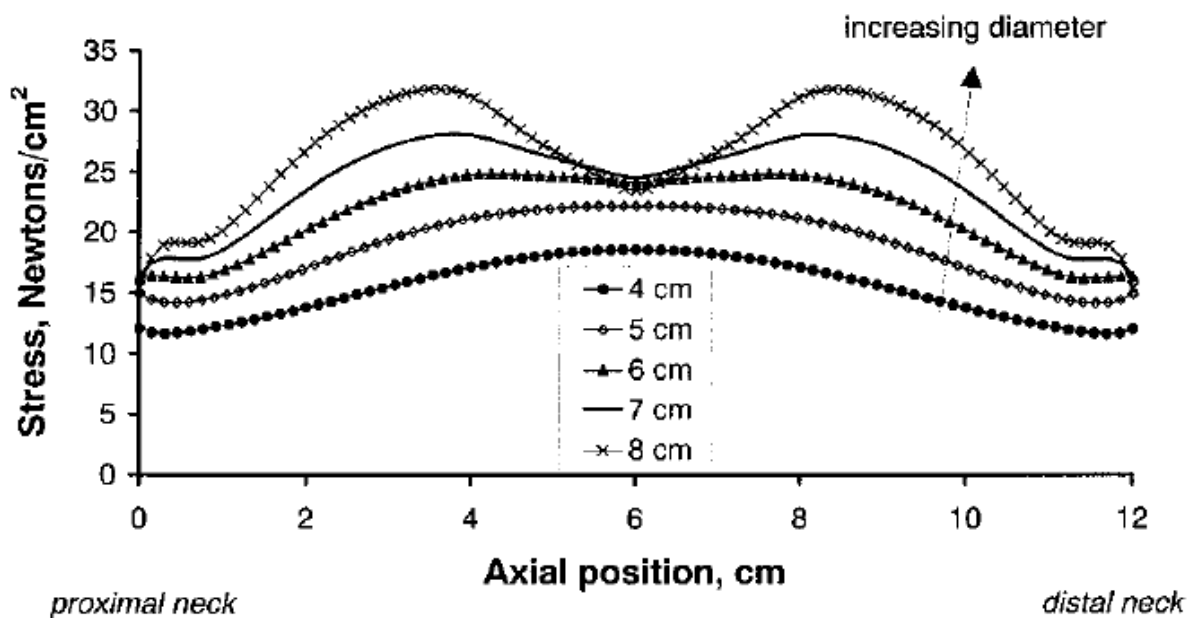


Figure 47 shows A, effect of symmetry, and B, effect of maximum diameter on the longitudinal wall stress distribution of the posterior AAA's surface, starting from  $z = 0$  cm, superior end, to  $z = 12$  cm, inferior end, and  $z = 6$  cm midsection [4].

## Effect of Diameter and Asymmetry on Peak Wall Stress

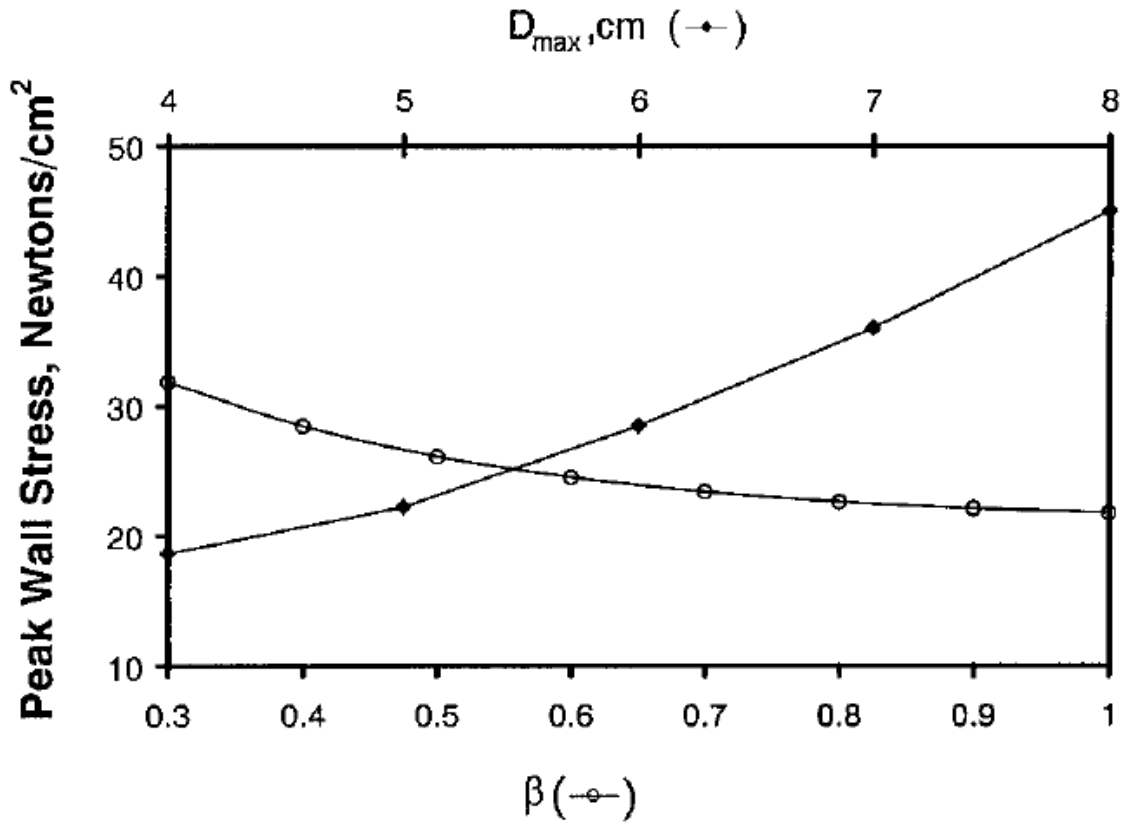


Figure 48 shows the effect of increasing diameter and asymmetry on the peak wall stress constructed AAA [4].

Based on the results, Vorp et al. concluded that different shapes of AAA experienced different wall stress distributions, and that some geometries may be at higher risk than others depending on the wall stress values of each AAA. However, this study was not able to conclude whether the maximum wall stress was always at the midsection, where the maximum diameter is, or elsewhere within the aneurysm, or whether large diameter aneurysms were at a higher rupture risk than the small diameter aneurysms. On the other hand, it could be concluded that an increase in maximum diameter and asymmetry increases overall rupture risk [4].

Canchi et al. performed a systematic review of various computational methods used in determining rupture risk factors in abdominal aortic aneurysms [51]. Computational fluid dynamics (CFD) were utilized to determine the nature of blood flow in the cardiovascular system, providing valuable information for physicians such as wall shear stress and pressure distributions [51]. Several steps were taken to employ CFD methods. First, CT or MRI is used to construct a 3-D model. Boundary conditions were obtained during surgery, which included pulsatile velocity and pressure. Finally, CFD codes were applied to obtain wall shear stress and pressure distributions [51]. Most CFD models used Navier-Stokes equations, which effectively described momentum flow. These equations were discretized using the flow volume method as well as the Finite Element Method. FEM is frequently used due to its ability to accurately simulate aortic wall tissue displacement. Inclusion of material properties provided the most accurate solutions. A fluid-structure interaction model, which coupled blood flow and wall movement through the application of arbitrary Lagrangian Eulerian method, was implemented [51]. Moreover, machine learning or data mining can be used to develop models which predict progression factors of AAAs and rupture potential based on comparison with previous data [51].

### **2.11. Implications**

Based on many studies performed in the literature, it is observed that the pathophysiology of AAA is very complex. The studies reviewed in this chapter provide an insight on different aspects of contributing to better assessment of rupture risk in AAA. An area lacking in the literature is the ability to predict rupture in AAA based on the tissue's microstructural state of Type-I collagen via relating stress-strain behavior with fragmentation of Type-I collagen in porcine tissue.

Thus, the research work done in this dissertation will provide insight on the accuracy of rupture prediction based on relating the stress-strain behavior and the microstructural state of healthy and Type-I collagen degraded samples. Then, the tissue property constants derived from experimental data will be utilized in a Finite Element model in order to mimic aneurysmal growth in AAA. Chapter 3 will discuss in detail the hypothesis, objective, and specific aims of this research work.

**Chapter 3**  
**Hypothesis, Objective, and Aims**

### **3.1. Goals and Objectives**

The objective of the study is to develop the capability to simulate the deformation of the aortic wall during growth and progression of AAA that requires the capability to conduct finite element analysis of pipes made from soft tissue to determine the following: Stress and strain in the region of the aneurysm and the effect of collagen degradation. Ultimately, the goal is to contribute to developing and identifying accurate constitutive relationships between stress and strain for large deformations and to develop a biomechanical rupture criterion, based on time-dependent Type-I collagen degradation, that can be incorporated into the current rupture criteria list to improve the accuracy of AAA risk assessment.

This study is designed to address the following questions: (a) How does collagen degradation contribute to rupture in AAA and (b) what is the effect of time-dependent collagen Type-I degradation on the tissue's biomechanical properties in relation to the risk of AAA rupture? It is likely that abnormal collagen degradation overtime causes the aortic tissue to rupture sooner in AAA. Thus, quantification of abdominal aortic aneurysm development, growth kinetics, and rupture criteria involving time-dependent collagen degradation are important because it will allow us to predict growth stages and when rupture may occur with greater accuracy.

### **3.2. Hypothesis**

The following are the hypotheses of this study:

Hypothesis 1: Rupture risk increases as tissue's stress-strain biomechanical behavior experiences reduction in non-linearity due to Type-I collagen degradation.

Hypothesis 2: Time-dependent collagen degradation can be used as an additional biomechanical predictor of AAA growth stages and rupture prediction.

### 3.3. Specific Aims

Our goal is to develop a more accurate model predicting aneurysmal growth and risk of rupture. We know that time-dependent collagen degradation alters tissue biomechanical properties. Thus, collagen degradation will lead to the development of an aneurysm and, eventually, rupture. As a result, the study of time-dependent collagen degradation will allow us to contribute to developing a more accurate growth prediction model. The study will potentially contribute to the development of a prognostic tool that will be able to identify the stages of AAA growth and potentially predict rupture more accurately. This study will focus on the following:

1. Perform stress-strain testing on healthy and time-dependent collagen degraded abdominal aortic specimens.
2. Observe and quantify Type-I collagen fiber content in healthy and time-dependent collagen degraded abdominal aortic specimens.
3. Conduct a Finite Element Analysis (FEA) to compare a time-dependent collagen degraded aortic model with a healthy aortic model via using experimentally calculated healthy and collagen Type-I tissue parameters in the FEA software.

This will be accomplished through the following specific aims (Figure 49): perform enzymatic degradation and biomechanical testing; observe tissue histology by imaging and quantification of reduction in mature Type-I collagen fiber content in healthy and time-dependent collagen-degraded aortic specimens using the Picrosirius red staining (PSR) method; and apply a strain-rate dependent constitutive relationship to conduct Finite Element Modeling using the experimentally calculated tissue parameters.

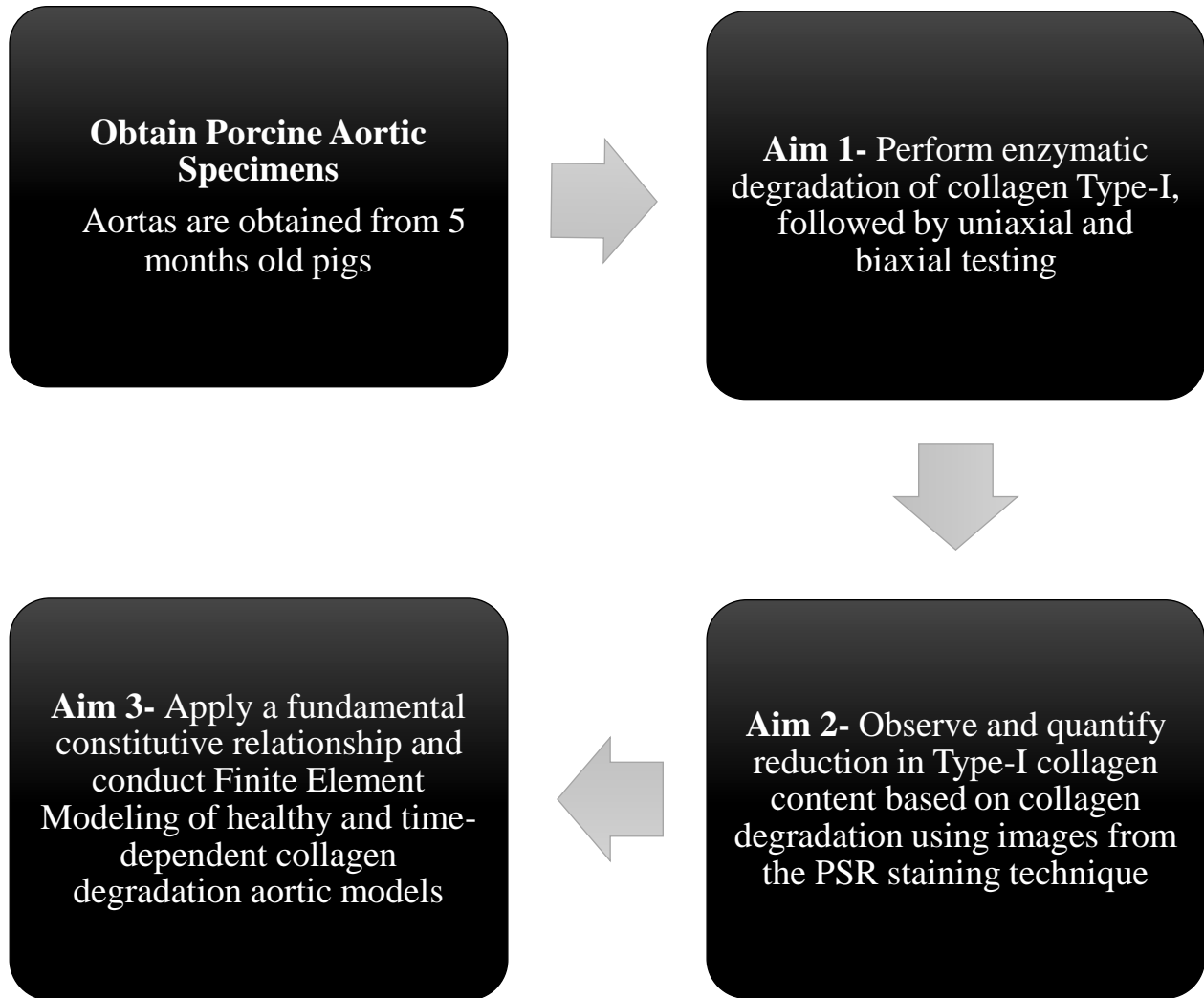


*Figure 49 Specific Aims*

In each of the following three chapters, chapter 4: Mechanical Testing and Constitutive Model, chapter 5: Imaging and Collagen Quantification, and chapter 6: Finite Element Modeling, the methods, results, and discussion of each specific aim will be addressed. Even though all specific aims are related, different techniques were applied to achieve the results. In fact, breaking down the methods for each specific aim will make it easier to communicate a thorough understanding of the research process. Finally, a conclusion chapter will follow the aforementioned three chapters.



**Chapter 4**  
**Mechanical Testing**

#### **4.1. Methods**

A stress-strain apparatus, an Instron 5944 (Instron, Norwood, MA, USA), was used for uniaxial mechanical testing, and a biaxial testing machine (TestResources, Shakopee, MN, USA) was used for equibiaxial testing. Both of the machines' set-up included a bio-bath, which allowed tests to be performed under natural physiological conditions that resemble the in-vivo environment of soft tissue.

A total of 80 abdominal aortic specimens were obtained from five month old pigs. Sections of the abdominal aorta were cut along the sagittal plane to obtain a longitudinal orientation and along the transverse plane to obtain a circumferential orientation. Each specimen had a length of 5-7 cm, a width of 2-2.5 cm, and a thickness of approximately 1.5-2 mm. Specimens were stored in a freezer at a temperature of  $-80^{\circ}\text{C}$ . Prior to mechanical testing, specimens were thawed at room temperature for 12 hours. Uniaxial stress-strain testing was performed on healthy and collagen Type-I degraded specimens in longitudinal and circumferential orientations. Specimens were mounted on the stress-strain apparatus and were immersed in the bio-bath, containing a phosphate-buffered saline solution (1X PBS), at  $37^{\circ}\text{C}$  for 30 minutes before performing the mechanical tests. The abdominal aortic specimens marked as collagen degraded were immersed in Type-I collagenase solution for periods of 4, 8, 12, and 16 hours prior to mechanical testing. The collagenase solution had a concentration of 0.30 g/ml, and was made via mixing of collagenase powder with 1X HBSS (Hank's Balanced Salt Solution). Specimens were placed in a fresh collagenase solution prior to every test performed. After mounting on the apparatus, specimens from both groups were preconditioned by performing 10 hysteresis cycles to untangle collagen fibers.

In addition, equibiaxial stress-strain testing was performed on healthy abdominal aorta (AA) specimens and collagen Type-I degraded AA specimens under conditions identical to uniaxial testing.

#### 4.2. Strain Rate Constitutive Model

A fundamental strain rate constitutive model was applied to fit the strain-rate dependent stress-strain relationship and the time-dependent collagen degradation stress-strain relationship. The derived equation below shows the fundamental strain rate constitutive model.

$$\sigma = E_0\varepsilon + c(\varepsilon^{m+1})(\dot{\varepsilon})^{m_1} \quad (4.1)$$

Where  $\sigma$  is stress,  $\varepsilon$  is strain,  $\dot{\varepsilon}$  is strain rate, and  $E_0$ ,  $c$ ,  $m$ , and  $m_1$  are property constants. The strain-rate dependent stress-strain relationship is illustrated in Figure 50. For constant strain rate, the following fundamental constitutive model is used.

$$\sigma = E_0\varepsilon + c_1(\varepsilon^{m+1}) \quad (4.2)$$

Where  $E_0$ ,  $c_1$ , and  $m$  are property constants, and the constant  $c_1$  absorbs the strain-rate term.

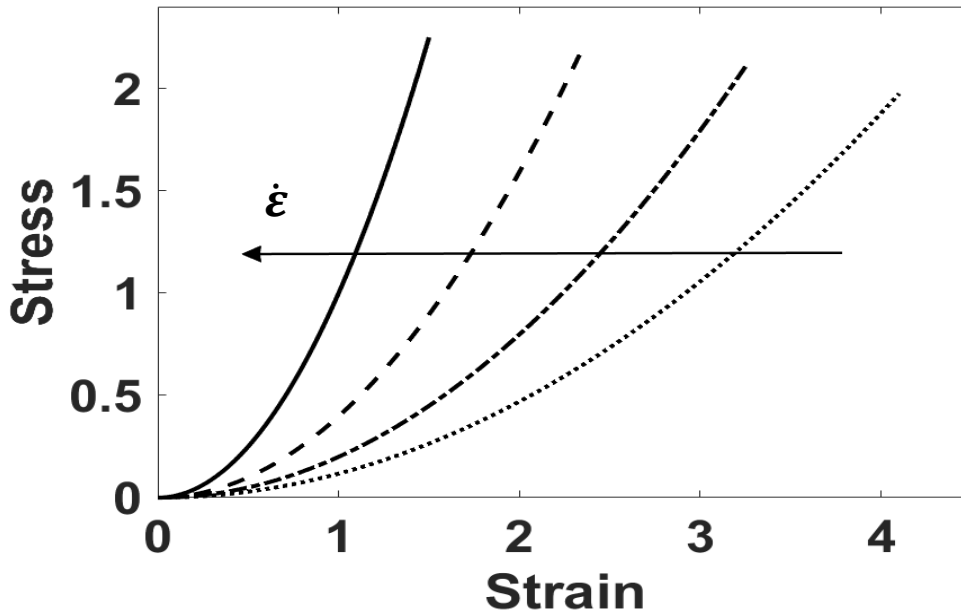


Figure 50 Fundamental Strain rate model illustrating how stiffness increases with increasing strain rate.

The above constitutive model can be utilized to incorporate the transition of mature Type-I collagen-fiber recruitment in tissue's stress support. Incorporation of time-dependent degradation of mature collagen-fiber content will allow us to observe how the stress-strain relationship is affected over time by degrading Type-I collagen. When fitting the results of the collagen degraded specimens to the model, the values of the constants will be used to represent changes in collagen Type-I content in each of the 4 periods for collagen degraded specimens. Multiple regression steps were used in order to compute average constant values of  $E_0$ ,  $m$ , and  $mI$  that are applicable to all testing conditions of strain-rate dependence. The only parameter that was left to vary with the strain-rate testing conditions was parameter  $c$ . Parameter  $c$  quantifies the recruitment of collagen fibers in supporting the stress applied.

### 4.3. Fung Constitutive Model

The Fung Constitutive Model was utilized in this study in order to characterize and quantify the planar biaxial behavior of healthy and time-dependent collagen degraded tissue groups. The Fung-type Model is well-known and suitable for arterial wall [52]. The model accounts for anisotropic material property and has proper ties with the strain energy density function given by:

$$W = \frac{A_0}{2} \left[ e^{(A_1 E_{11}^2 + A_2 E_{22}^2 + 2A_3 E_{11} E_{22})} - \mathbf{1} \right] \quad (4.3)$$

Where  $E_{11}$  and  $E_{22}$  are Green strains along the circumferential and longitudinal orientations, respectively, and  $A_0$ ,  $A_1$ ,  $A_2$ , and  $A_3$  are constitutive parameters. The following assumptions were considered in this model: incompressible tissue, circumferential and longitudinal collagen fiber orientations (0 and 90 degrees, respectively), uniform wall thickness, and mostly homogenous tissue.

#### 4.4. Uniaxial Tests

Uniaxial biomechanical tests were performed to observe the stress-strain relationship in healthy and time-dependent collagen degraded aortic specimens. Uniaxial tests were performed using Instron 5944 machine (Instron, Norwood, MA, USA), as shown in Figure 51.

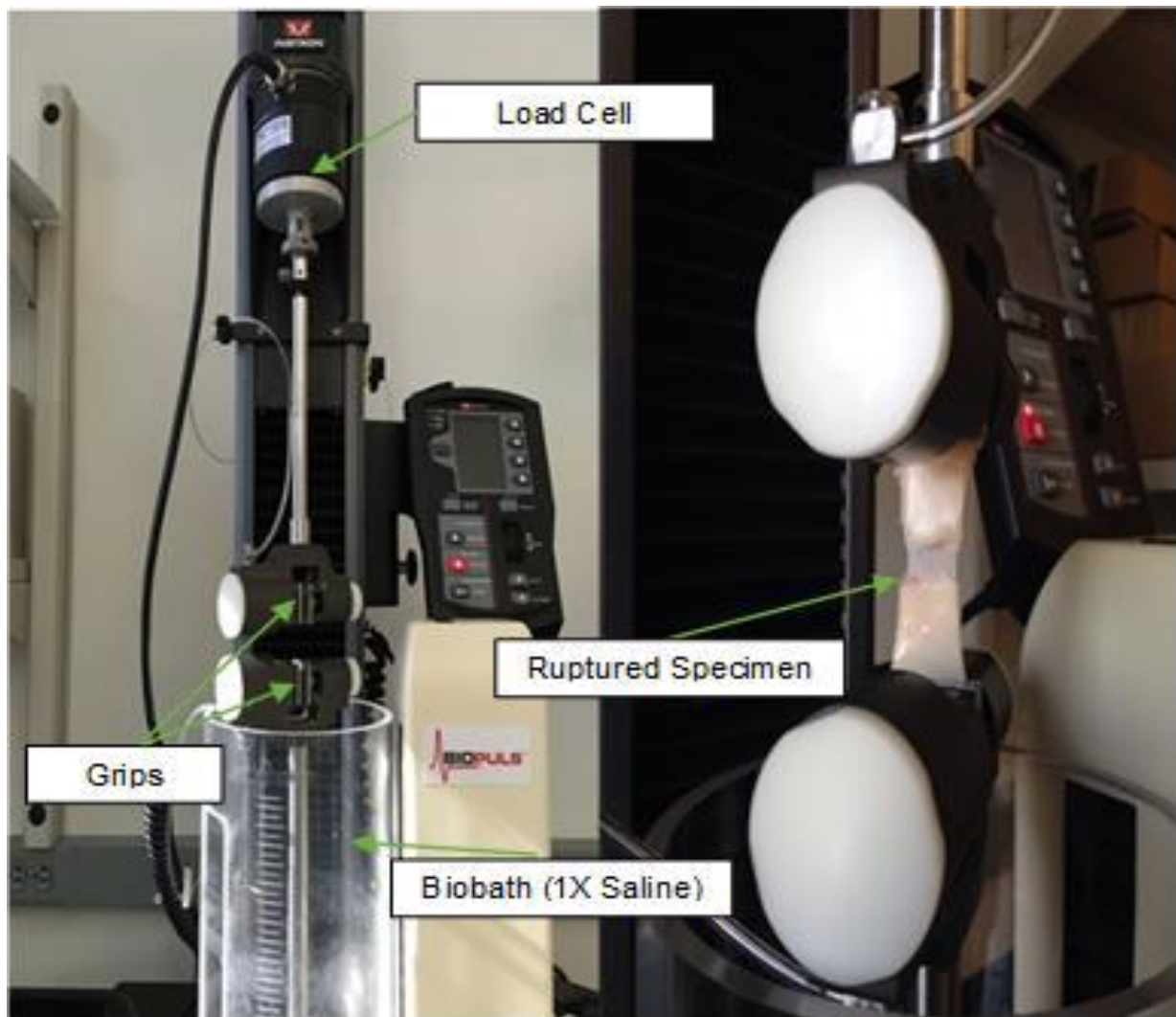


*Figure 51 Instron 5944 Testing machine equipped with a Bioplus bath and a post-testing uniaxial ruptured specimen.*

Uniaxial stress-strain testing was performed on healthy and 4, 8, 12, and 16-hour collagen degraded infrarenal porcine aortic specimens in order to study the biomechanical properties of

aortic tissue. Specific tissue properties/parameters were calculated using an established stress-strain relationship model. Strain rate-dependent uniaxial stress-strain testing was performed on healthy infrarenal aortic specimens to demonstrate how stress-strain relationship in longitudinal and circumferential directions vary with time, as shown in Figures 52 and 53.

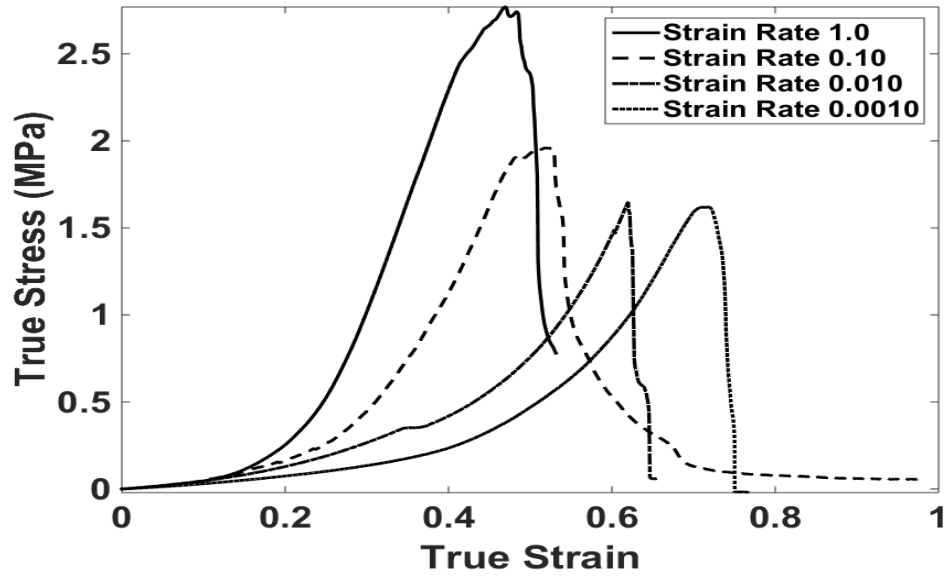


Figure 52 Strain rate-dependent uniaxial test on healthy circumferential specimens. (strain-rate in mm/mm/min)

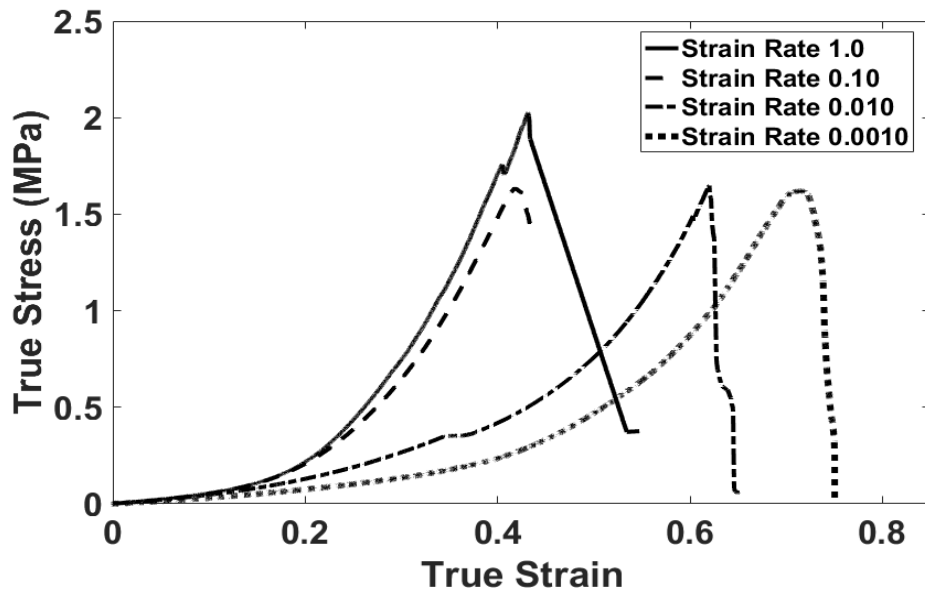
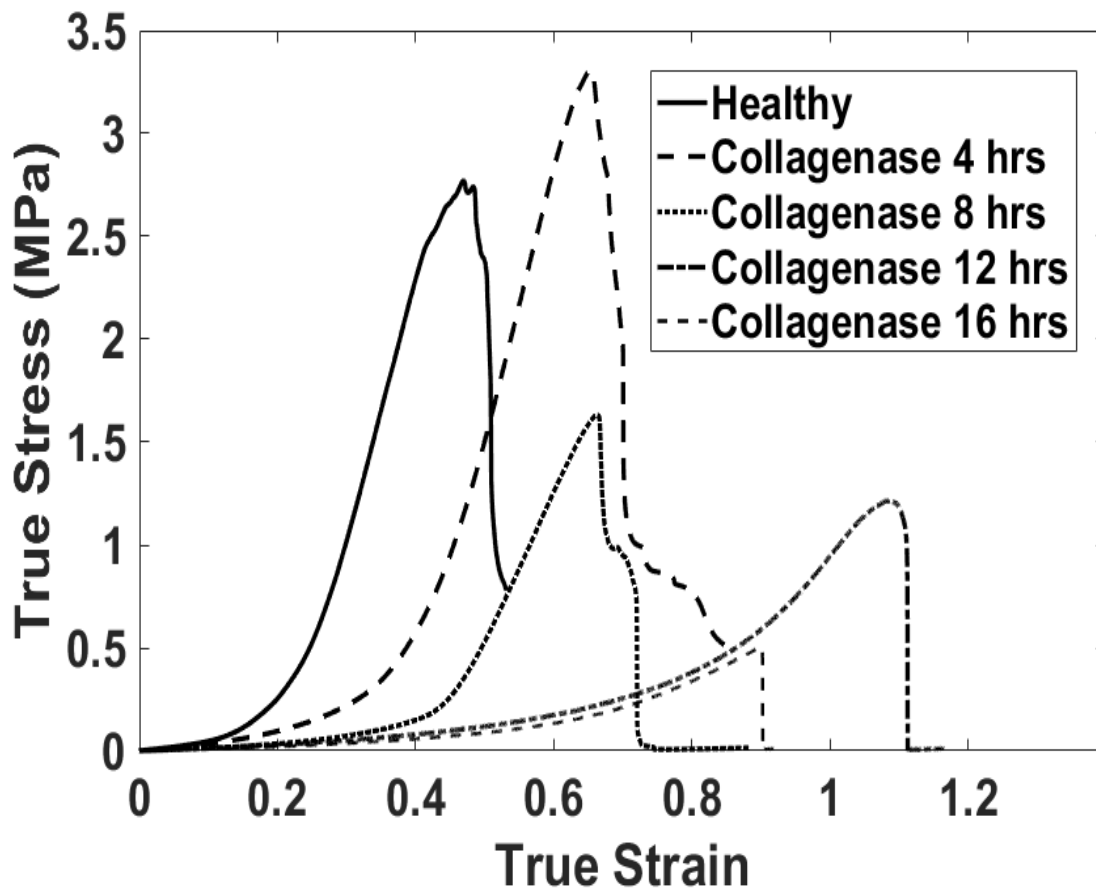


Figure 53 Strain rate-dependent uniaxial test on healthy longitudinal specimens. (strain-rate in mm/mm/min)

The changes in tissue elasticity with time are essential in prediction of rupture. Thus, time-dependent collagen degradation is considered in order to observe and compare the relationship between strain-rate-dependence and time-dependence.

Uniaxial and biaxial testing were performed on collagen degraded specimens for 4 periods: 4 hours, 8 hours, 12 hours, and 16 hours. A constant collagenase concentration of 1000 units/mL was maintained. Uniaxial stress-strain testing results are shown in Figures 54 and 55.



*Figure 54 Uniaxial stress-strain behavior of collagen degraded abdominal aortic specimens in the circumferential orientation*

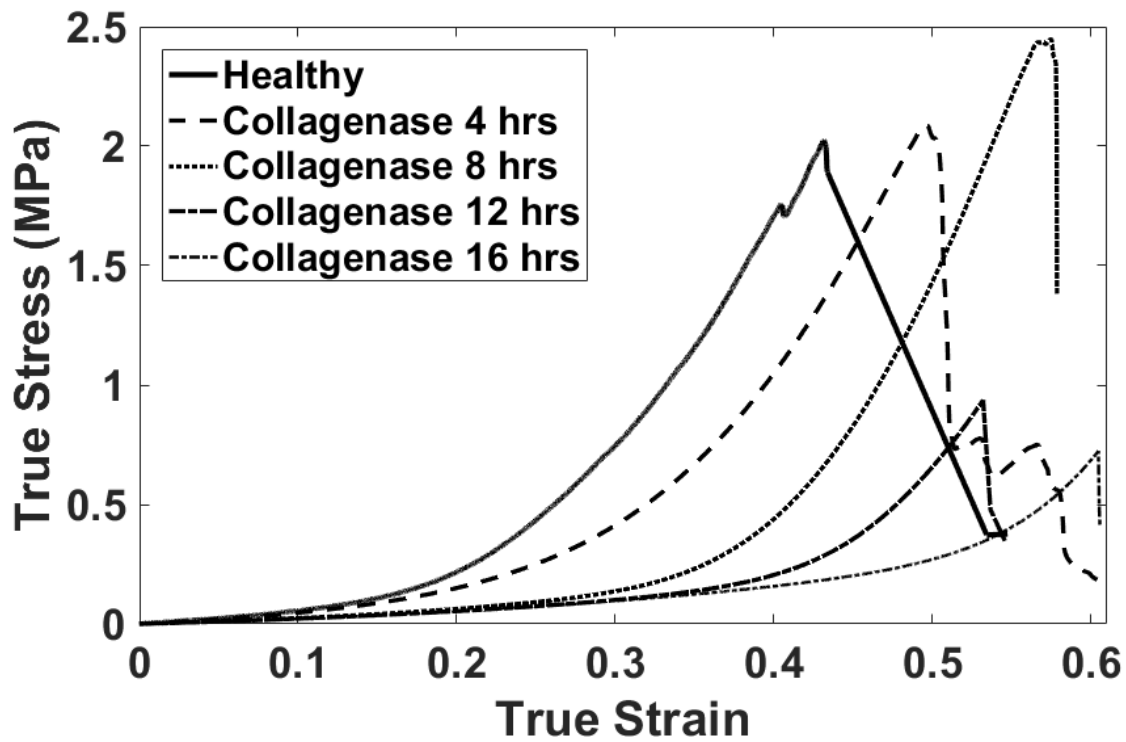


*Figure 55 Uniaxial stress-strain behavior of collagen degraded abdominal aortic specimens in the longitudinal orientation*

In Figures 54 and 55, focusing on the strain range from 0 to 0.40 the change in stress-strain illustrates how the non-linear turns into more linearized behavior as more collagen is degraded over time. Figures 56 and 57 below show a focused view of this stress-strain relationship over a strain range of 0 to 0.40.



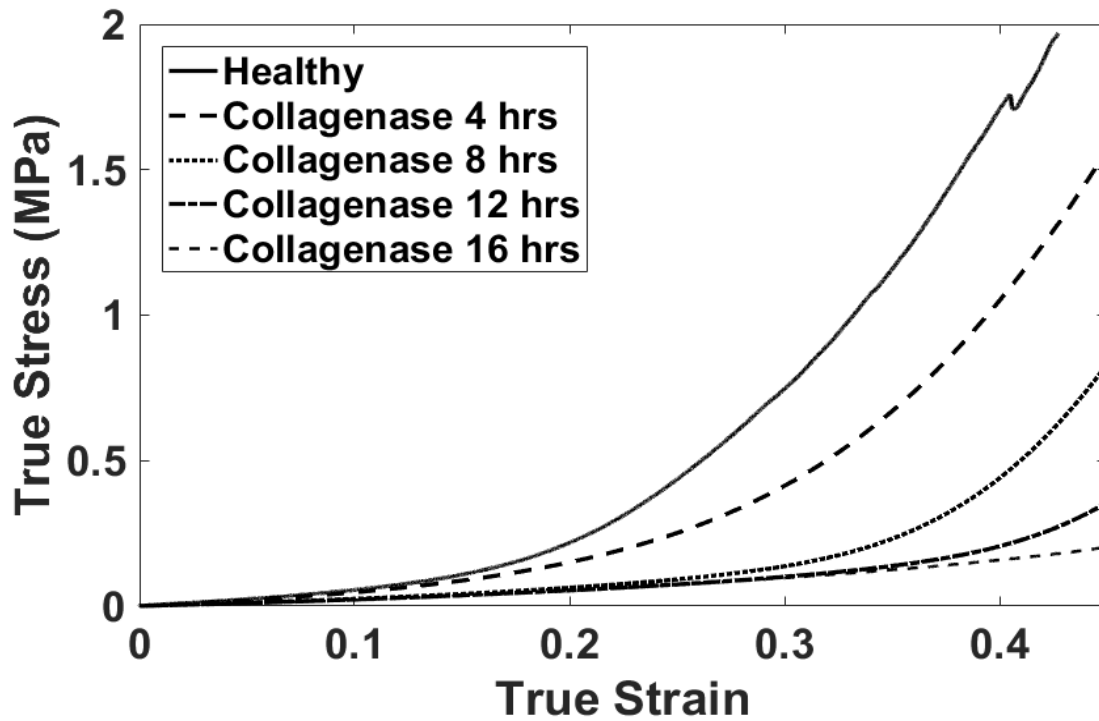


Figure 56 Uniaxial stress-strain behavior of collagen degraded abdominal aortic specimens in the circumferential orientation

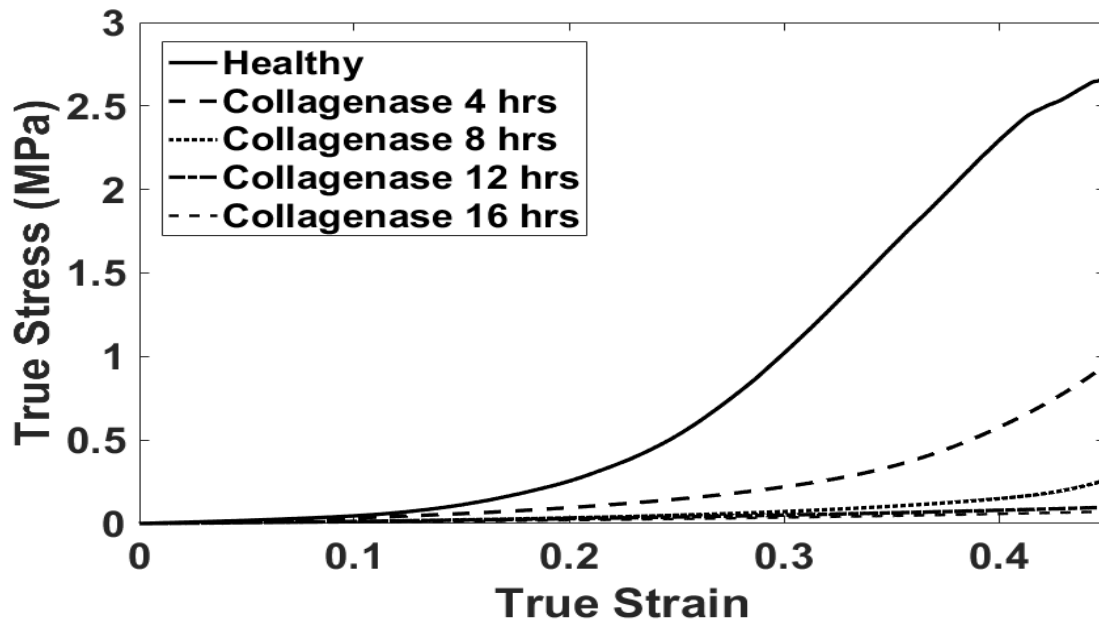


Figure 57 Uniaxial stress-strain behavior of collagen degraded abdominal aortic specimens in the longitudinal orientation

Table 4 shows the calculated values of  $E_o$ ,  $c$ ,  $m$  and,  $ml$  from regression for the 4 different strain rates (1, 0.1, 0.01, and 0.001 per min).

*Table 4 Regression values of  $E_o$ ,  $c$ ,  $m$  and,  $ml$  for the 4 different strain rates in both orientations.*

<b>Orientation-Strain Rate (mm/mm/min)</b>	<b><math>E_o</math></b>	<b><math>c</math></b>	<b><math>m</math></b>	<b><math>ml</math></b>	<b><math>R^2</math></b>
<b>C (1)</b>	0.3531	61.71	2.8985	-0.5352	0.999
<b>C (0.1)</b>	0.3531	15.41	2.8985	-0.5352	0.999
<b>C (0.01)</b>	0.3531	0.8967	2.8985	-0.5352	0.995
<b>C (0.001)</b>	0.3531	0.1609	2.8985	-0.5352	0.992
<b>L (1)</b>	0.3531	23.95	2.8985	-0.5352	0.989
<b>L (0.1)</b>	0.3531	2.191	2.8985	-0.5352	0.988
<b>L (0.01)</b>	0.3531	0.1196	2.8985	-0.5352	0.976
<b>L (0.001)</b>	0.3531	0.0132	2.8985	-0.5352	0.999

Table 5 shows the calculated values of  $E_o$ ,  $c_l$ , and  $m$  from regression of the data for the 4 different periods of collagen degradation (4, 8, 12, and 16 hours).

*Table 5 Regression values of  $E_o$ ,  $c$ , and  $m$  for the 4 different periods in collagenase in both orientations.*

<b>Orientation-Period (hrs)</b>	<b><math>E_o</math></b>	<b><math>c_l</math></b>	<b><math>m</math></b>	<b><math>R^2</math></b>
<b>C (Healthy)</b>	0.3531	61.71	2.8985	0.999
<b>C (4)</b>	0.3531	31.69	2.8985	0.999
<b>C (8)</b>	0.3531	13.97	2.8985	0.936
<b>C (12)</b>	0.3531	4.06	2.8985	0.904
<b>C (16)</b>	0.3531	0.8293	2.8985	0.955
<b>L (Healthy)</b>	0.3531	23.95	2.8985	0.989
<b>L (4)</b>	0.3531	19.37	2.8985	0.991
<b>L (8)</b>	0.3531	5.217	2.8985	0.866
<b>L (12)</b>	0.3531	0.146	2.8985	0.846
<b>L (16)</b>	0.3531	0.0857	2.8985	0.738

Figures 58-59 show the experimental and fitted graphs of the stress-strain behavior for different strain-rates, and Figures 60-61 show the experimental and fitted graphs of the time-dependent collagen degraded groups using the proposed strain-rate constitutive model. The agreement is quite good for the various strain rates and for various collagen degraded groups in the longitudinal and circumferential directions.

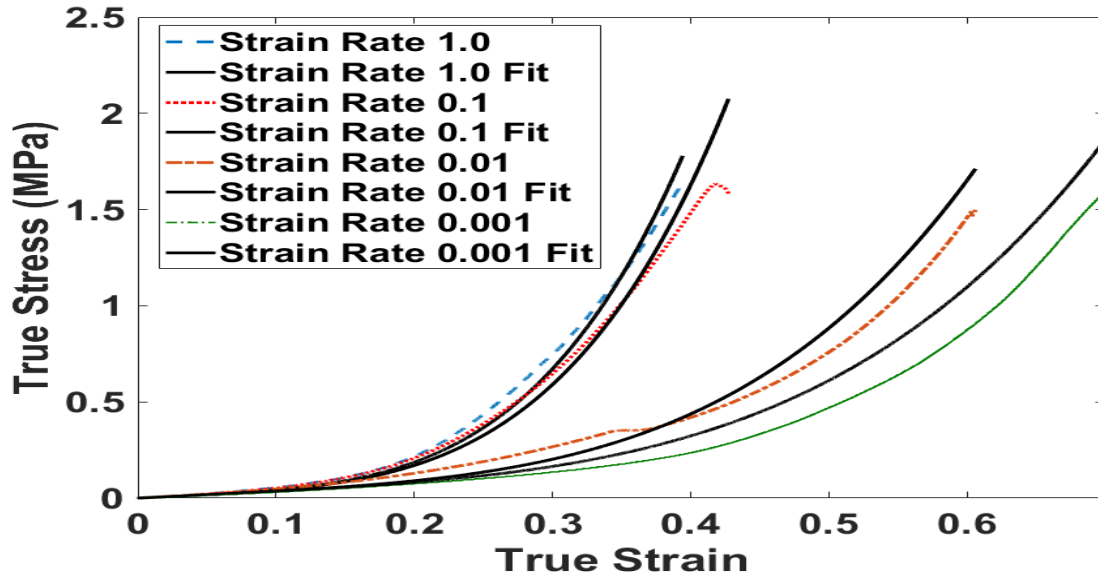


Figure 58 strain-rate dependent data and fitted curves in the circumferential orientation

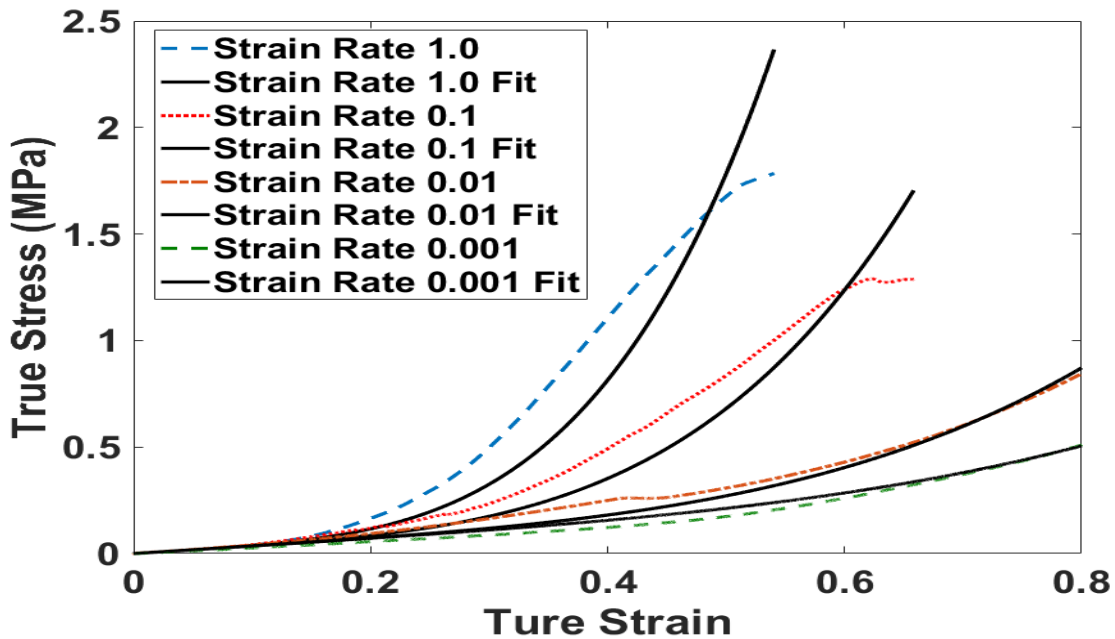


Figure 59 strain-rate dependent data and fitted curves in the longitudinal orientation

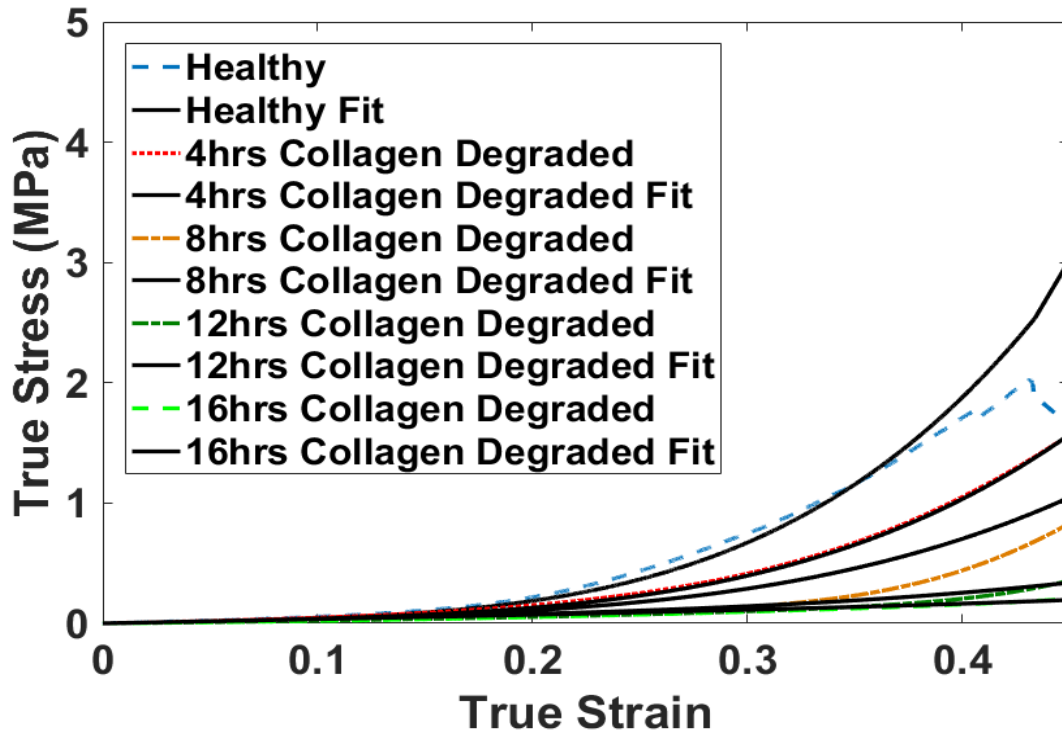


Figure 60 Collagen-degraded data and fitted curves for circumferential orientation specimens

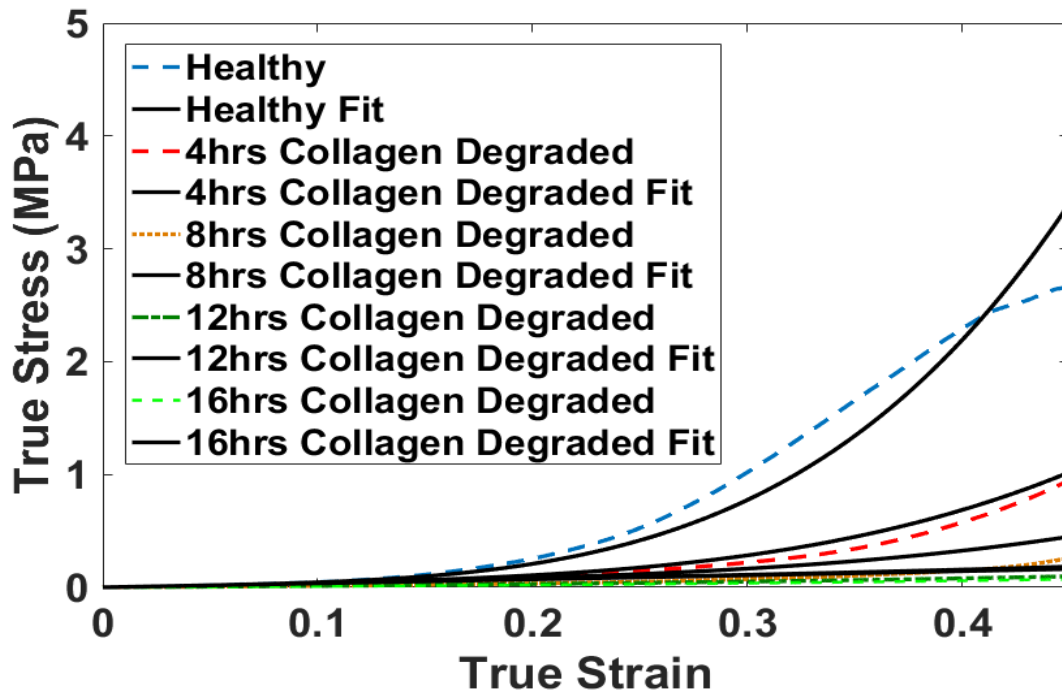
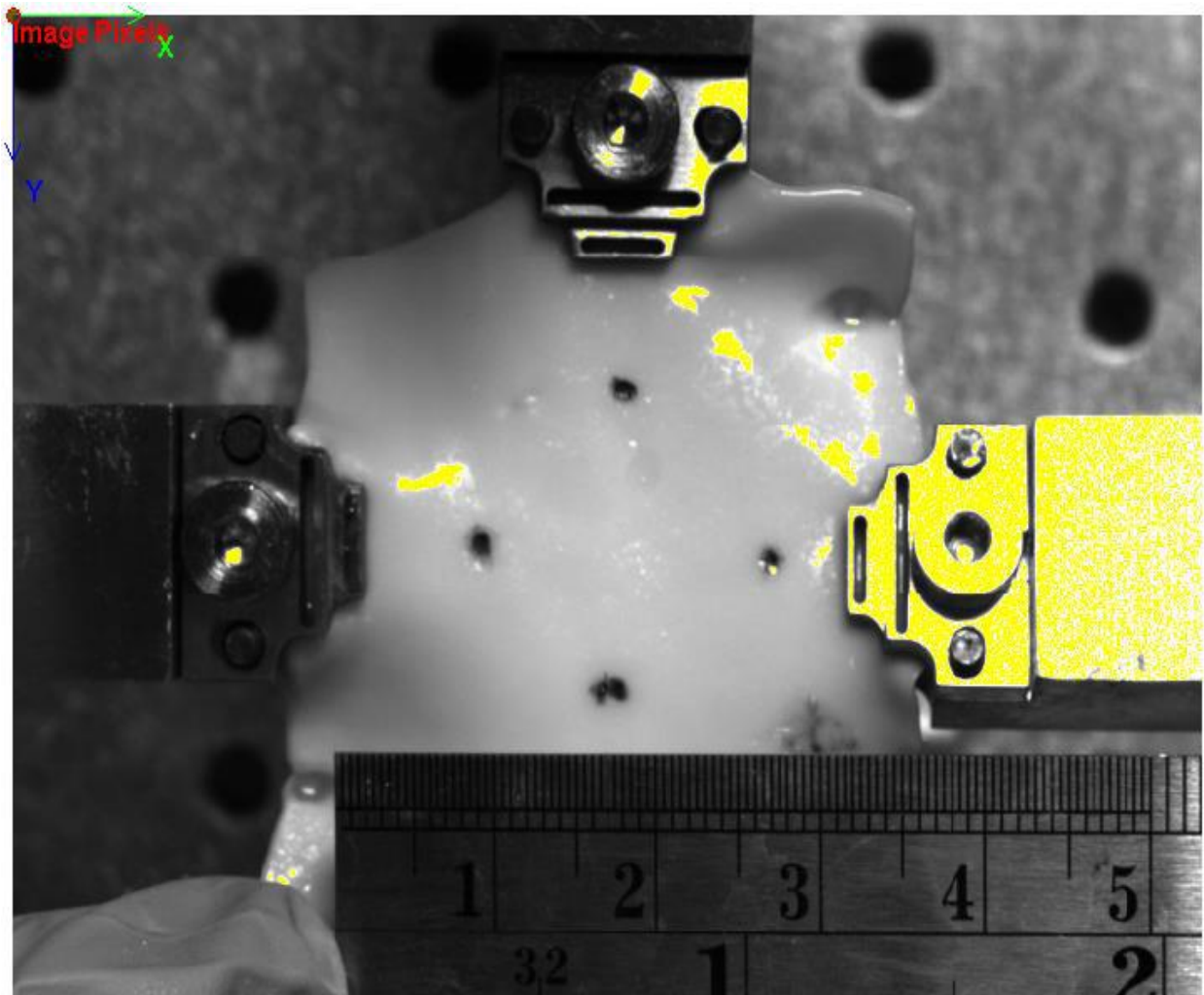


Figure 61 Collagen-degraded data and fitted curves for longitudinal orientation specimens

#### 4.5. Biaxial Tests

Biaxial testing machine (TestResources, Shakopee, MN, USA (Figure 62)) was used to perform stress-strain tests on healthy and 4, 8, 12, and 16-hour collagen degraded infrarenal porcine aortic specimens in order to detect how the stress-strain relationship in longitudinal and circumferential directions relates to uniaxial tests, as shown in Figures 63 and 64. To avoid strain measurement distortions while using the video extensometer system, the specimens were marked with ink dots at points far enough in front of the grips, as shown in Figure 62.



*Figure 62 TestResources Biaxial Testing machine with a specimen mounted where the vertical direction is the longitudinal orientation and the horizontal direction is the circumferential orientation.*

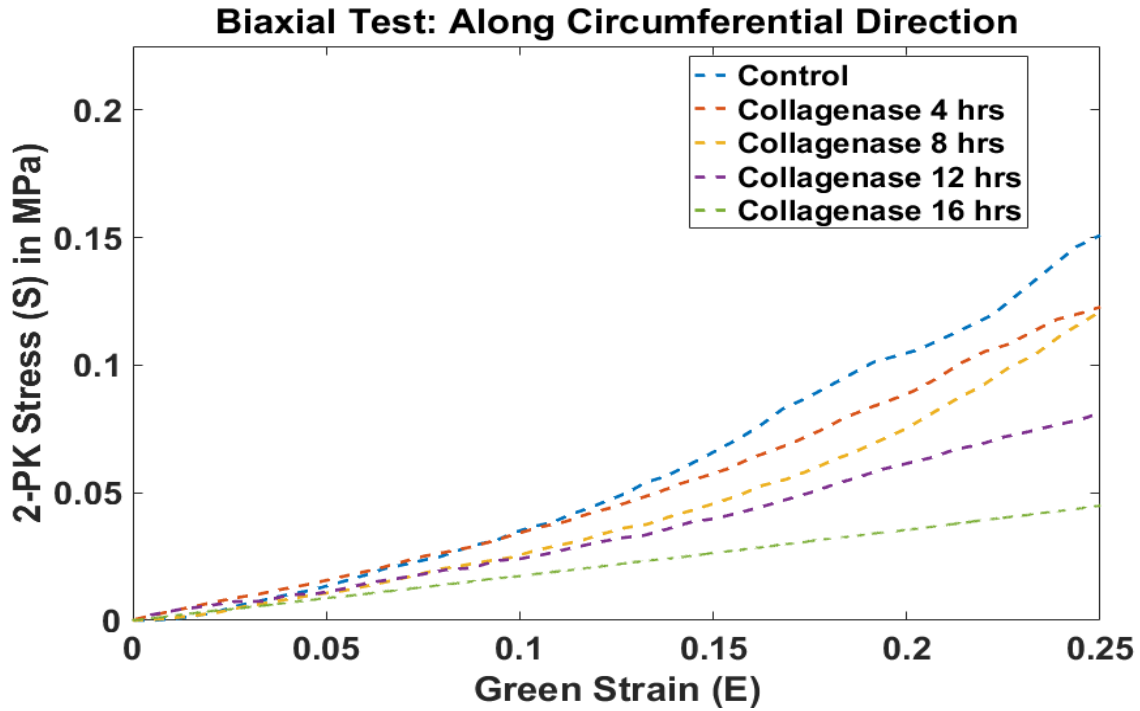


Figure 63 Biaxial stress-strain behavior of collagen degraded abdominal aortic specimens in the circumferential direction

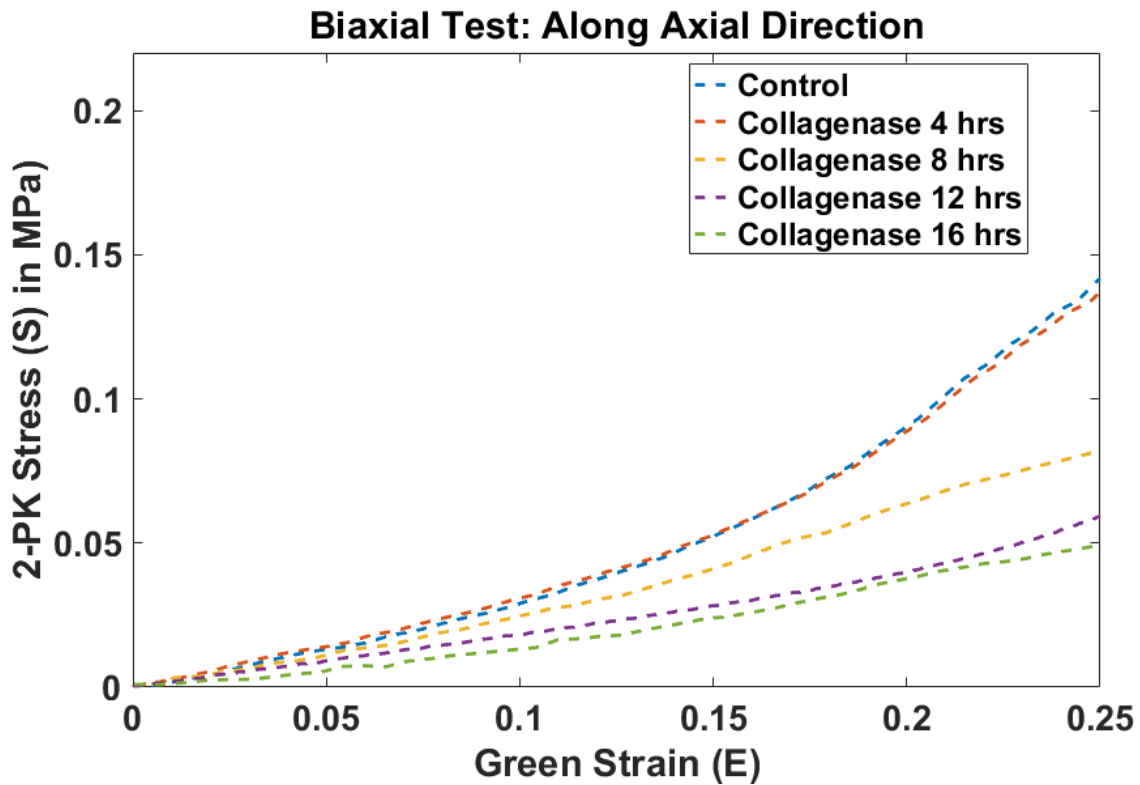


Figure 64 Biaxial stress-strain behavior of collagen degraded abdominal aortic specimens in the longitudinal direction

The constitutive parameters of the Fung model, shown in Table 6, were estimated from regression using the Levenberg-Marquardt method in MATLAB.

*Table 6 The fitted constitutive parameters of the Fung model*

<b>Group</b>	$A_0$ (MPa)	$A_1$	$A_2$	$A_3$	$R^2$
<b>Healthy</b>	0.03708	12.07	3.224	0.999	0.992
<b>4-hour Collagen Degraded</b>	0.0412	10.01	1.205	0.6905	0.997
<b>8-hour Collagen Degraded</b>	0.02044	14.54	1.543	0.5577	0.998
<b>12-hour Collagen Degraded</b>	0.04178	7.421	1.188	0.3033	0.996
<b>16-hour Collagen Degraded</b>	0.05077	4.137	0.5202	0.0901	0.999

The fitted parameters were used to calculate the strain energy density using the Fung Model, equation 4.3. Figures 65-69 show the strain energy density and the Green's strains along the circumferential and longitudinal axis for all five groups.

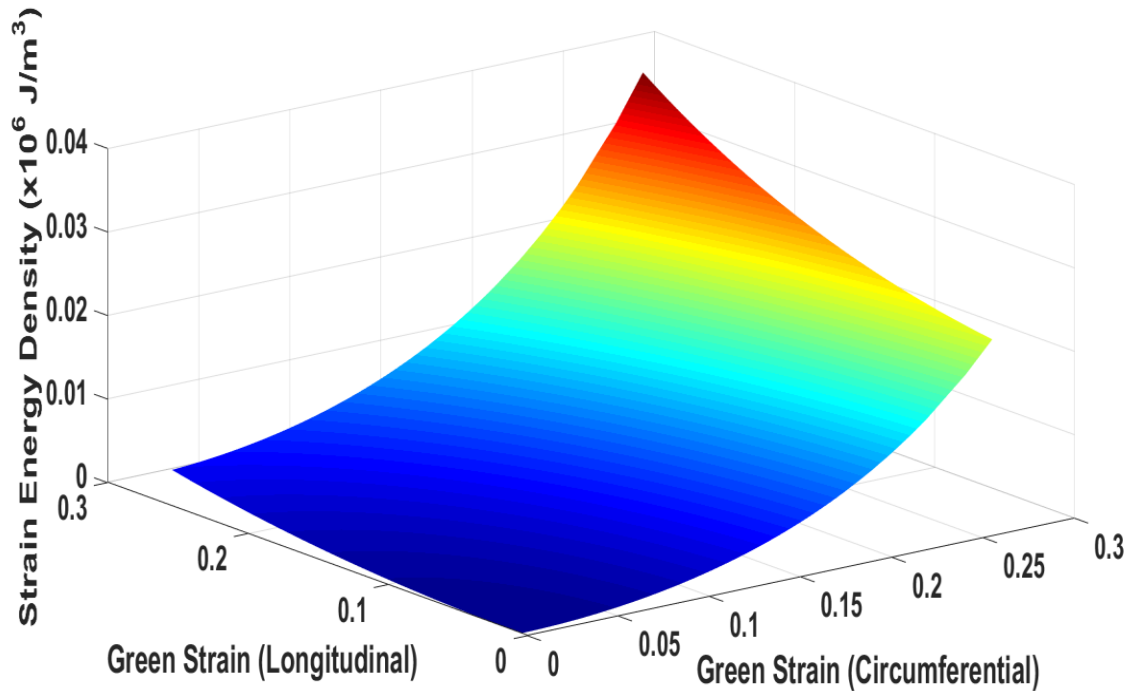


*Figure 65 Strain energy density vs Green strain for healthy specimen*

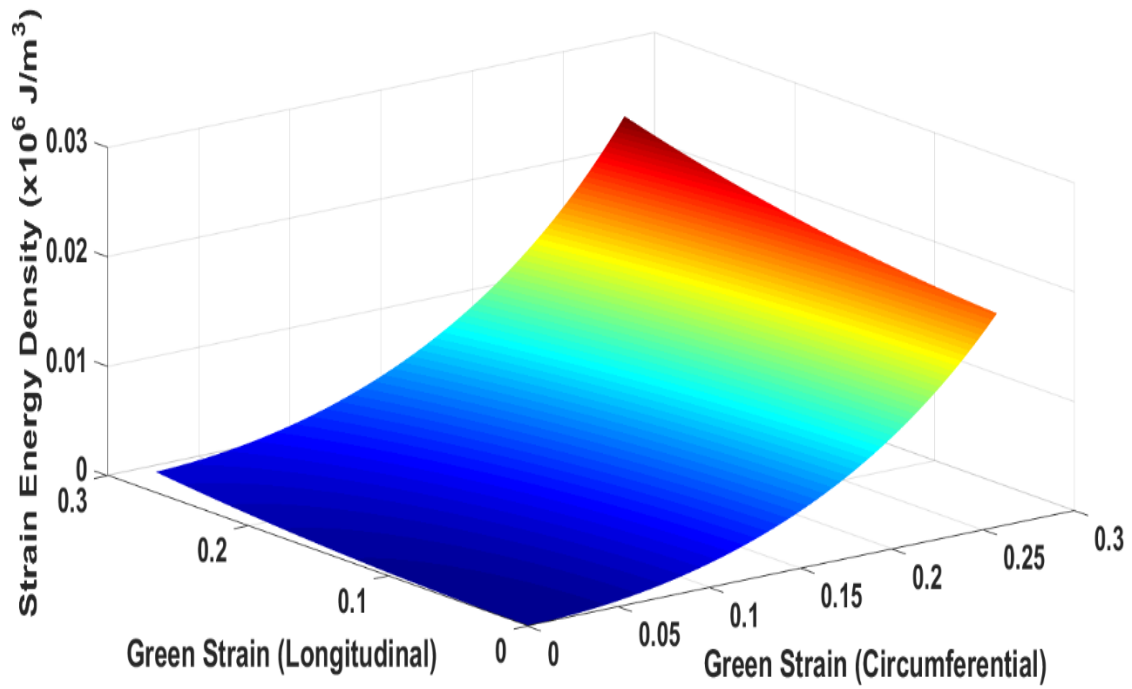


Figure 66 Strain energy density vs Green strain for 4-hr collagen degraded specimen

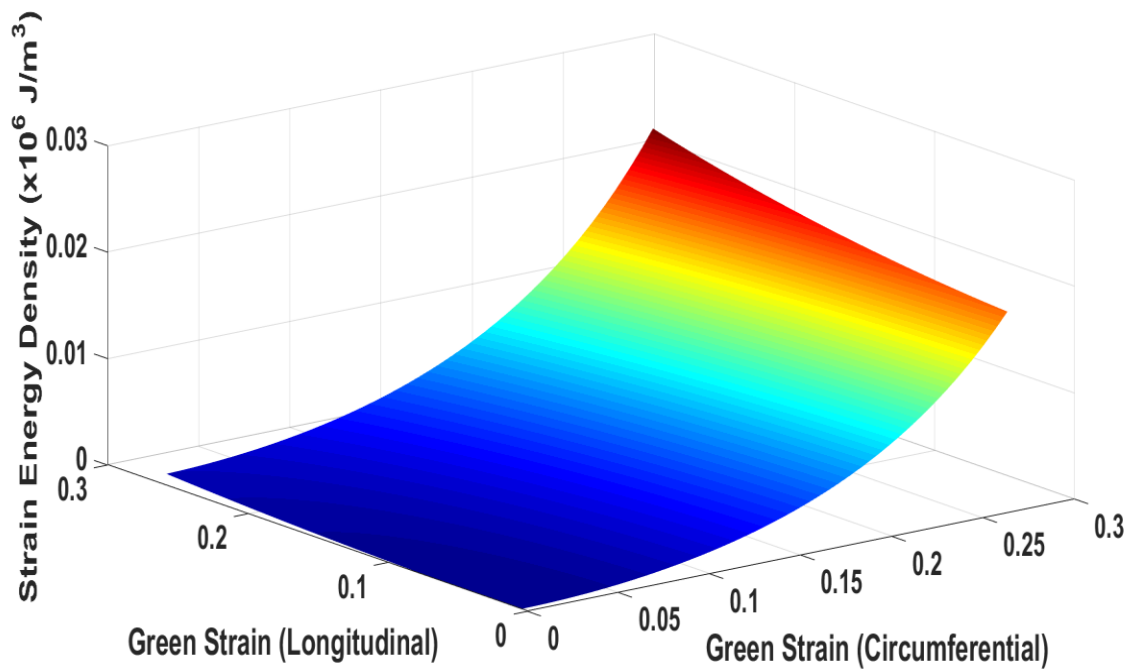


Figure 67 Strain energy density vs Green strain for 8-hr collagen degraded specimen



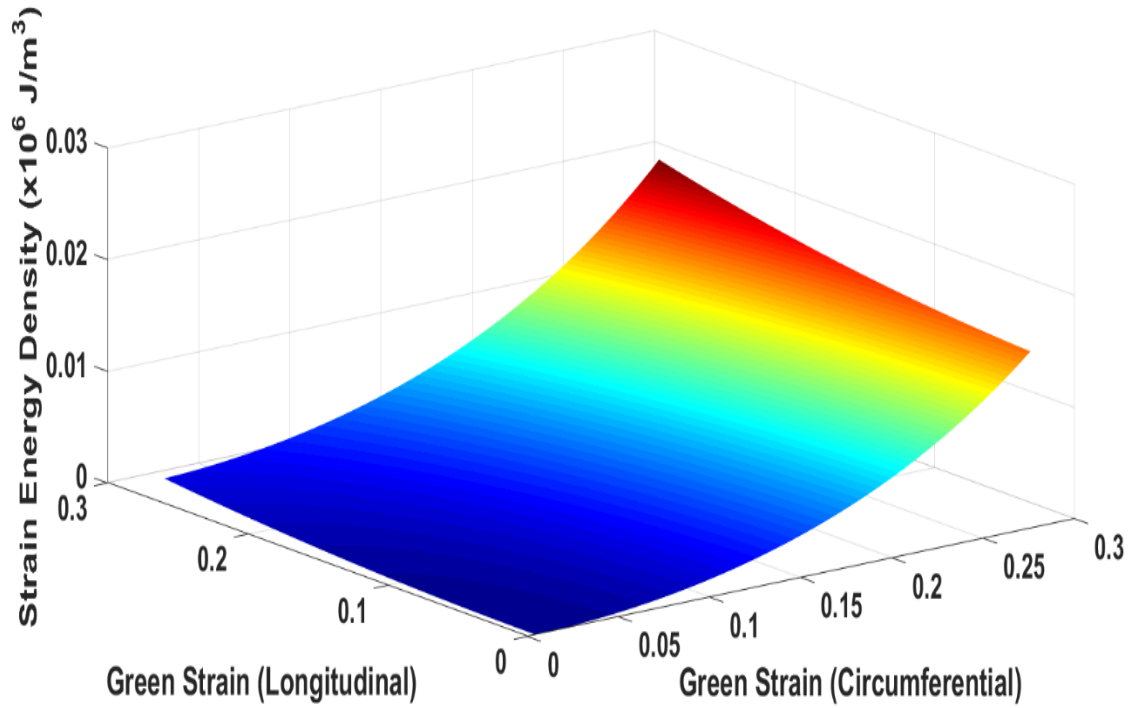


Figure 68 Strain energy density vs Green strain for 12-hr collagen degraded specimen

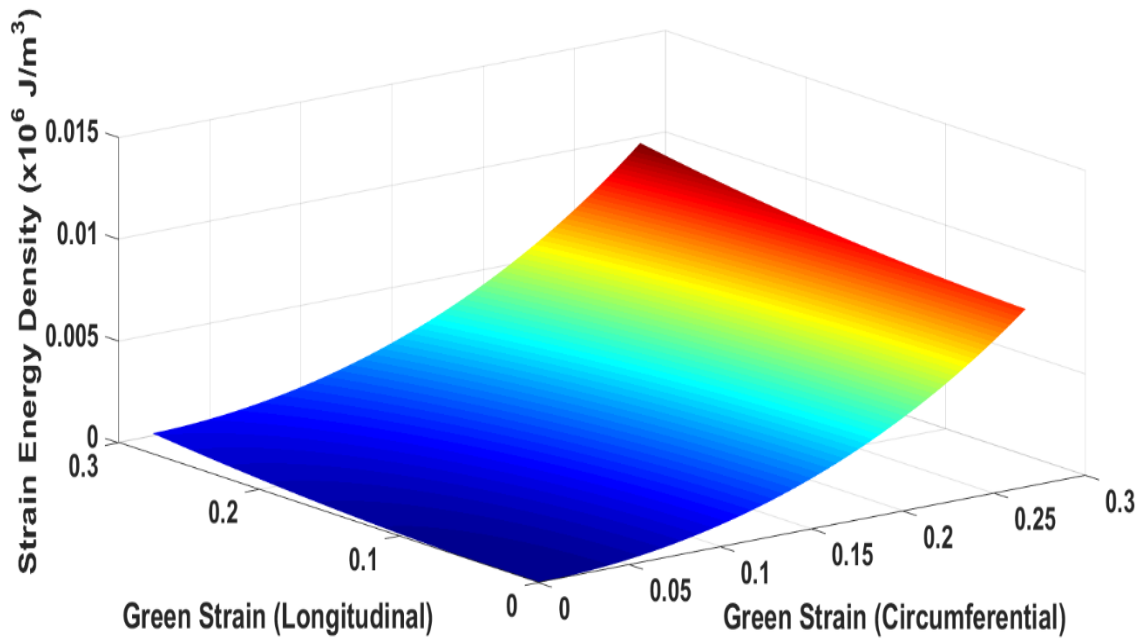


Figure 69 Strain energy density vs Green strain for 16-hr collagen degraded specimen

#### 4.6. Discussion

The stress-strain relationship behavior of aortic tissue is illustrated in Figure 70 below:

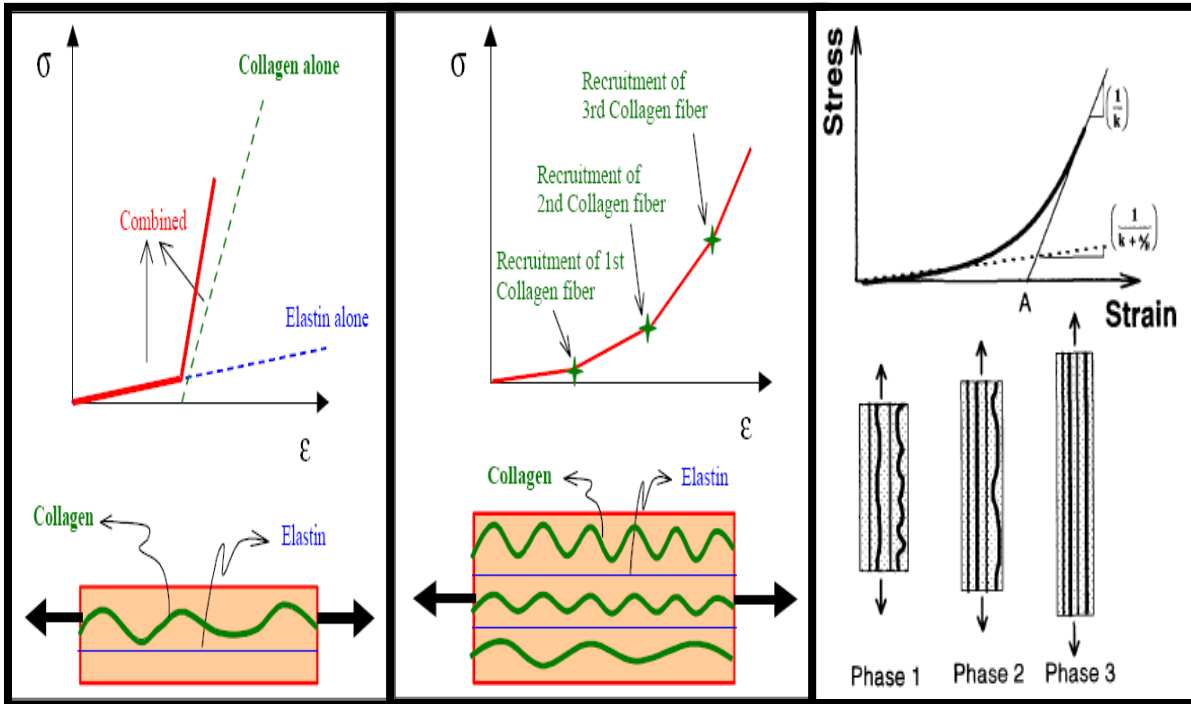


Figure 70 stress-strain relationship of aortic tissue illustrated as an exponential relationship when elastin and collagen are intact [1, 20].

At low strain values, collagen fibers are coiled and support minimal stress. However, when strain increases, collagen fibers begin to uncoil to support stress. Although elastin and collagen *separately* exhibit linear behavior, each with a unique elastic property, the *combined* behavior of the fibers appears non-linear as shown in Figure 70.

The recruitment phases labelled in Figure 70 are phases 1, 2, and 3. Phase 1 represents the recruitment of the first collagen fiber, phase 2 represents the recruitment of the second collagen fiber, and phase 3 represents the full recruitment of collagen fibers. In our study, we establish the concept of critical strain, which is the strain at the condition of full collagen fiber recruitment. The critical strain value ( $\epsilon_c$ ) is the parameter A value shown in Figure 70. In this study, a more precise definition of parameter A is established. Parameter A can be redefined as the critical strain that is

related to expected strain at rupture. When the applied strain exceeds the critical strain value ( $\epsilon_c$ ) of the tissue, the tissue will be at a higher significant risk of rupture [22].

Collagen is important for the tissue to maintain its strength. If only elastin fibers are present, the tissue will be much weaker. As a result, the tissue will have low ability to sustain loads/stresses and a low critical strain value. Consequently, the tissue will be at a much higher risk of rupture, especially due to the forcing function, which is the pressure generated to push a volume of blood through the aorta. However, in the region of the aneurysm, the local pressure will be somewhat relieved because the same volume of blood flows through a larger cross-sectional area.

When comparing the average elastic modulus in the full collagen recruitment region for healthy tissue group with that for collagen degraded tissue groups, as shown in Table 7 below, the collagen degraded tissue groups are less stiff than the healthy tissue. The decrease in stiffness is due to collagen degradation in the tissue, which lowers its ability to support the stress applied and, ultimately, leads to smooth muscle degradation causing an overall destruction of the tissue's structural integrity [3, 18]. Such change in tissue properties alters the biomechanical behavior of the tissue as shown previously in the collagen degraded stress-strain relationship in Figures 54 and 55.

The uniaxial testing on the healthy tissue group was performed at 4 different strain rates to observe the change in elastic modulus at full collagen recruitment for slower strain rates. The results in Figures 52 and 53 showed that the elastic modulus at full collagen recruitment decreased for lower strain rates. The stress and strain reported in uniaxial testing graphs are true stress and true strain. True stress accounts for change in cross sectional area with time and is defined as the load applied on the specimen divided by the instantaneous cross-sectional area. True strain

accounts for instantaneous increases in instantaneous gauge length of the specimen and is defined mathematically as the natural log of the instantaneous length over the original length.

When comparing peak wall strength points in Figures 52 and 53 (peak points in the stress-strain curve) for healthy specimens tested at different strain rates, we found that the peak wall strength point decreased with decreasing strain rate. Peak wall strength decreased from 2.55 MPa to 1.5 MPa in circumferential orientation and from 2.2 MPa to 1.7 MPa in longitudinal orientation, for strain rate 1.0 and strain rate 0.001, respectively. The reason for such reduction is due to the viscoelastic response of elastin, which is time-dependent; thus, it can accommodate, at slower strain rates, the applied displacements at a lower value of stress. Our constitutive model accounts for that. In addition, the reduction could be due to the slow transition in recruitment of collagen fibers in supporting the stress and the prolonged tensile stress applied on the tissue at slower strain rates. When observing the values of the fitted parameters in Table 4, we can see that the value of parameter  $c$  decreases as strain rates decrease, which indicates that the needed collagen recruitment rate to accommodate the applied displacement is lower at slower strain rates. Thus, the recruitment of collagen fibers in stress support is essential in predicting rupture, and eliminating such transition to support the stress will make rupture imminent.

The primary focus of conducting time-dependent collagen degradation and computing the critical strain value ( $\epsilon_c$ ) was to assess collagen degradation with time and its association with rupture risk. To calculate the critical strain, an additional mathematical relationship derived from the strain-rate constitutive model was utilized in this study to further analyze the ex vivo biomechanical behavior of healthy and time-dependent collagen degraded abdominal aortic specimens [20].

The following mathematical equation was used to calculate the critical strain value ( $\epsilon_c$ ):

$$\sigma_{phase\ 3} = \left(\frac{1}{K}\right)\epsilon - \frac{\epsilon_c}{K} \quad (4.4)$$

Where  $(1/K)$  is the average elastic modulus at full collagen recruitment ( $E$ ). From Uniaxial testing of healthy AA specimens and collagen degraded specimens, the average elastic modulus at full collagen recruitment values ( $E$ ), critical strain value ( $\epsilon_c$ ), average maximum stress, and average maximum strain ( $\epsilon$  at rupture) are shown in Table 7.

*Table 7 calculated values of average elastic modulus, parameter A, average uniaxial maximum stress, and average maximum strain for all the specimens used in the study.*

<b>Specimens Group</b>	<b>Average E (MPa)</b>	<b>Critical Strain (<math>\epsilon_c</math>)</b>	<b>Average maximum <math>\sigma</math> (MPa)</b>	<b>Average maximum <math>\epsilon</math> (<math>\epsilon</math> at rupture)</b>
Healthy circumferential (N=12)	7.6375 $\pm$ 0.0299	0.3146 $\pm$ 0.0049	2.7297 $\pm$ 0.0192	0.7611 $\pm$ 0.0047
Healthy longitudinal (N=12)	4.0385 $\pm$ 0.0761	0.2216 $\pm$ 0.0040	2.1837 $\pm$ 0.0048	0.6429 $\pm$ 0.0053
4hr Collagen degraded circumferential (N=6)	4.0888 $\pm$ 0.0715	0.2039 $\pm$ 0.0042	3.3022 $\pm$ 0.0071	0.6233 $\pm$ 0.0049
4hr Collagen degraded longitudinal (N=6)	2.5332 $\pm$ 0.0715	0.1895 $\pm$ 0.0027	2.0715 $\pm$ 0.0111	0.4800 $\pm$ 0.0040
8hr Collagen degraded circumferential (N=6)	2.0578 $\pm$ 0.0356	0.1828 $\pm$ 0.0026	1.4269 $\pm$ 0.0226	0.6536 $\pm$ 0.0050
8hr Collagen degraded longitudinal (N=6)	0.9689 $\pm$ 0.0056	0.1433 $\pm$ 0.0028	2.3557 $\pm$ 0.0174	0.5820 $\pm$ 0.0053
12hr Collagen degraded circumferential (N=6)	0.8293 $\pm$ 0.0067	0.1221 $\pm$ 0.0031	1.2118 $\pm$ 0.0040	1.1366 $\pm$ 0.0331
12hr Collagen degraded longitudinal (N=6)	0.3760 $\pm$ 0.0052	0.0238 $\pm$ 0.01323	0.9214 $\pm$ 0.0079	0.5433 $\pm$ 0.0050
16hr Collagen degraded circumferential (N=6)	0.4501 $\pm$ 0.0087	0.0459 $\pm$ 0.0020	0.4967 $\pm$ 0.0052	0.8078 $\pm$ 0.0057
16hr Collagen degraded longitudinal (N=6)	0.3593 $\pm$ 0.0062	0.0062 $\pm$ 0.0003	0.7187 $\pm$ 0.0074	0.6021 $\pm$ 0.0047
Values given as	Mean $\pm$ SEM			

We conclude that a higher critical strain value ( $\epsilon_c$ ) is indicative of an age younger than 30 years old based on similar findings from Raghavan et al. [20]. The conducted in-depth analysis of the significance of critical strain value ( $\epsilon_c$ ) is essential for potential rupture risk prediction, as observed in our study where the critical strain values ( $\epsilon_c$ ) for all of our specimens were calculated. It is shown in Table 7 that the critical strain values ( $\epsilon_c$ ) decrease as collagen degrades in the tissue. Consequently, the tissue weakens and will not be able to withstand moderate to high stress. In addition, our study indicates that collagen degrades as humans become older based on critical strain ( $\epsilon_c$ ), which has been proposed in a study by Raghavan et al. based on the corresponding age of donors in their study [20]. Thus, the risk for rupture also increases severely with age.

Two major points were drawn from the uniaxial and biaxial tensile testing of time-dependent treatment of porcine abdominal aortas with Type-I collagenase. When treated with collagenase, the porcine aortas became significantly less stiff. As the time of specimen exposure to collagenase increased, the level of tissue compliance also increased (Figures 54 and 55). This was true for the circumferential and longitudinal orientations under uniaxial and biaxial testing conditions. Gundiah et al. performed a similar study in which porcine aorta segments were treated with collagenase for periods of 1 and 6 hours (Figure 33) and reported an overall increase in tissue compliance, with a positive relationship to time [5]. Our results from tensile testing also revealed an increase in the linear behavior of collagenase treated aorta segments, compared to that of healthy aortas (Figures 54 and 55). Gundiah et al. recorded similar results with respect to collagenase's effect on aortic tissue stress-strain behavior (Figure 33) [5].

Collagen degraded specimens, in Figures 54 and 55, exhibit a decreased non-linear stress-strain behavior under uniaxial tension due to reduced collagen fiber recruitment. This behavior mimics the phenomenon suggested by Raghavan et al. studies [1, 20]. In addition, for collagen

degraded specimens, it is shown in Table 5 that the value of parameter  $c_1$  decreases with degrading collagen Type-I. This indicates that degrading collagen will eliminate the recruitment of collagen in tissue stress support. In addition, tissue exposure to collagenase Type-I resulted in increased dispensability, which was proved in similar studies by Choke et al., Gundiah et al., and Vorp et al. All three studies investigated the effects of tissue collagen degradation, which may indicate that the disruption in collagen structure can interfere with the overall structural integrity of the tissue's main components such as elastin and smooth muscle [3, 5, 18]. Kivikari and Gundiah et al. reported that similar degrading of collagen for longer periods of time resulted in increased dispensability, reasoning that the dissociation of the adventitia layer overstretches the tissue and causes rupture [5, 53].

Uniaxial testing of AA specimens is not sufficiently accurate. The physiological application of stress on the abdominal aorta is not solely uniaxial in the human body; rather, it is multiaxial. In addition, the aortic tissue is subjected to hoop and radial stress. Thus, to improve upon the accuracy of the modeled stress-strain behavior and to closely mimic the physiological loading state on the aorta, biaxial testing of AA porcine specimens was performed. When performing biaxial testing on specimens, the stress is reported as second Piola-Kirchhoff stress  $S$  (2<sup>nd</sup> P-K), and the strain is reported as Green strain due to large displacements that occur during deformation. Second P-K stress is a measure of the force vectors in the deformed configuration of the specimens converted back to the forces in the undeformed configuration of the specimen via the deformation gradient divided by the undeformed cross-sectional area of the specimen, given as the following:  $S = JF^{-1}\sigma F^{-T}$ , where  $J$  is the Jacobian ( $J = 1$ , for incompressible materials, which is one of our assumptions);  $F^{-1}$  is the inverse of the deformation gradient;  $\sigma$  is the stress;  $F^{-T}$  is the

inverse of the transpose of the deformation gradient matrix. Second P-K is symmetric and is a material tensor field, which is parametrized by material coordinates only.

In small strains, the change in square length of elements (quadratic strain terms) can be neglected due to infinitesimally small displacements, and instead can be calculated using the simple strain relationship:  $\varepsilon = \frac{\Delta l}{l}$ . However, when strains are large, the relationship is affected by the quadratic terms because the square length of elements is considerably larger. Green strain accounts for the quadratic terms in large deformations and is unaffected by rotations that may occur to the specimen under testing conditions; thus, it is used in this study. Green strain ( $E$ ) is also symmetric and based on the deformation gradient ( $F$ ) of the specimen and is given by  $E = \frac{1}{2}(F^T \cdot F - I)$ , where  $F^T$  is the transpose of the deformation gradient matrix, and  $I$  is the identity matrix.

Similar to uniaxial testing results, biaxial testing showed a decrease in stiffness when collagen is degraded over time. In addition, referring to Table 6, the value of parameter  $A_3$  decreased, as more collagen was degraded. Thus, such a decrease indicated that in-plane coupling among collagen fibers between the circumferential and longitudinal orientations decreased; Kural et al. proposed a similar concept by characterizing the biaxial behavior of diseased human carotid and coronary arteries and concluded that diseased arteries exhibited less in-plane coupling among collagen fibers [52]. To demonstrate the differences between equibiaxial testing of healthy and time-dependent collagen degraded groups for up to 30% strain, the strain energy density for all groups was calculated using the Fung Model fitted parameters and plotted in Figures 65-69. A



significant reduction in strain energy density exists between healthy and all collagen degraded groups ( $p < 0.05$ ) and among all collagen degraded groups, shown in Figure 71.

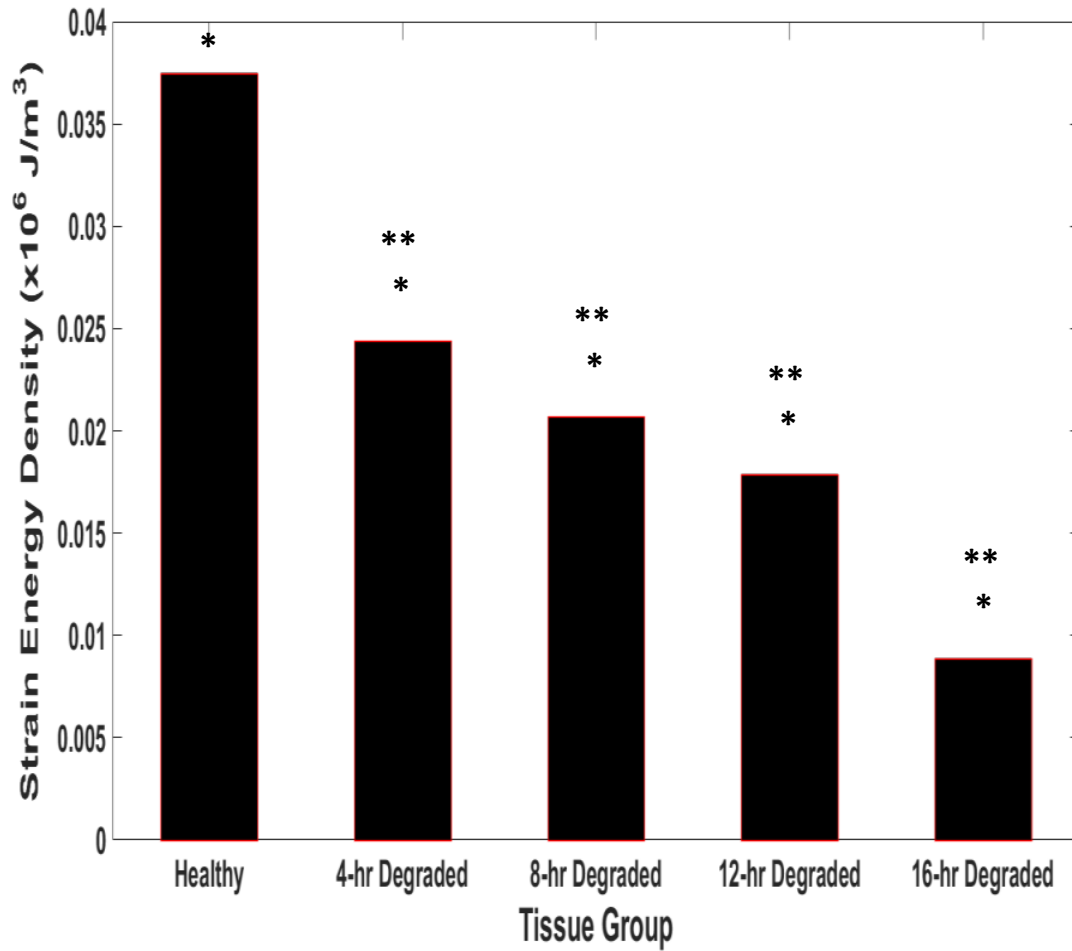


Figure 71 strain energy density for all groups. (\*) significant reduction in strain energy density exists between healthy and all collagen degraded groups ( $p < 0.05$ ). (\*\*) significant reduction in strain energy density exists among all collagen degraded groups ( $p < 0.05$ )

Many studies assess the biomechanical behavior of human AAA and rupture risk. Incorporating a biomechanical approach in clinical data is necessary in order to improve the accuracy of rupture risk assessment. Thus, collagen fiber content and fragmentation with age is an essential biomechanical factor that plays an important role in assessing rupture risk because of collagen's vital role in maintaining the tissue's microstructural integrity and cohesiveness. More importantly, quantifying the decrease in collagen recruitment due to time-dependent collagen degradation can contribute to predicting when rupture may take place. If collagen fibers are able to be imaged and quantified in vivo using dyes and imaging techniques in the near future, then the application of this study is feasible.

**Chapter 5**  
**Collagen Imaging**

## 5.1. Methods

Collagen-fiber staining was done using picosirius red staining (PSR) method. PSR is used for detection and quantification of collagen fiber thickness based on the optical properties of collagen. Sirius red is a strong anionic dye that stains collagen fibers. The sulphonic acid groups of the PSR react with basic ( $\text{pH}>7$ ) groups present in the collagen molecule. The elongated dye molecules are attached parallel to the long axes of collagen fibers, and the dye molecules are enhanced by collagen's birefringence.

Once the mechanical testing was carried out on healthy and collagen degraded samples, the staining procedure was performed as follows: samples were covered with Optimal Cutting Temperature compound (OCT) and were left to freeze at  $-26^{\circ}\text{C}$  before sectioning to  $7\ \mu\text{m}$  slices using the cryotome, as shown in Figure 72.



*Figure 72 Cryotome used to slice specimens*

Next, the prepared slides were placed in acetone for 5 minutes, washed with tap water for 10 minutes, dipped in distilled water, placed in Phosphomolybdic Acid .2% aqueous for 4 minutes, stained in sirius red, .1% in saturated picric acid, for 90 minutes, set in .01 N hydrochloric acid for 2 minutes, subjected to dehydration with 70% alcohol for 45 seconds, dehydrated in 95% ethanol for 3 minutes, dehydrated again in absolute ethanol for 3 minutes, and placed in Xylene for 5 minutes. Then, the slides were mounted with Cytoseal and coverslips were added. Finally, the mounted slides were left to cure in the hood for 24 hours before imaging.

A regular bright field microscope was used to image the collagen content in each specimen. Our protocol established the use of a polarizer placed on a regular bright field microscope, as shown in Figure 73. The polarizer was oriented in such a way that the background was as dark as possible. The phase plate was set to Phase 1 (PH1) and filter wheel was set to 6. The color order represented fiber-thickness as follows: Green<Yellow<Orange<Red (from thinnest to thickest fibers).

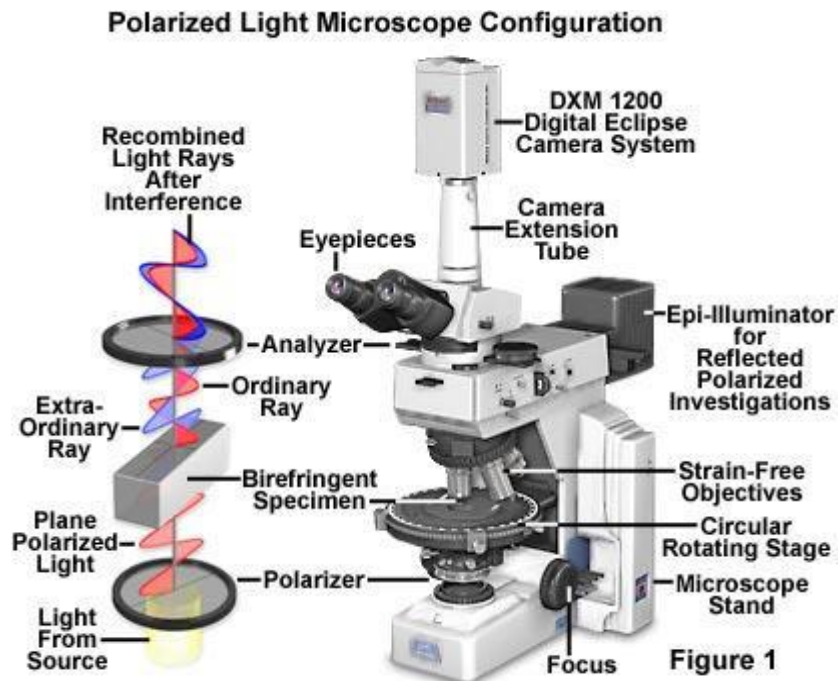


*Figure 73 Polarized Light Microscope Setup*  
 [<http://www.microscopechina.net/newsend2.asp?id=7>]

## 5.2. Collagen Microstructural Imaging

Imaging of healthy and collagen degraded specimens was done to examine changes in collagen-fiber content at a microstructural level. Collagen-fiber staining was done using picosirius red staining (PSR) method as mentioned above [54]. When specimens were immersed in collagenase, collagen fibers were cleaved and fragmented as exposure time to collagenase increased.

When picosirius red stains collagen fibers, the exhibited colors reflect fibers' thickness based on maturity of the fibers. The reddest fibers are known to be the most mature. Collagen Type-I was the primary focus of interest because it's known for being the most abundant and mature in the tissue [9]. Thus, only reduction in red collagen fibers (Type-I collagen) was quantified, using MATLAB. The images in Figures 74 and 75 show the stained collagen fibers for healthy and collagen degraded groups (4, 8, 12, and 16-hour collagen degraded groups) for circumferential and longitudinal specimens, respectively.

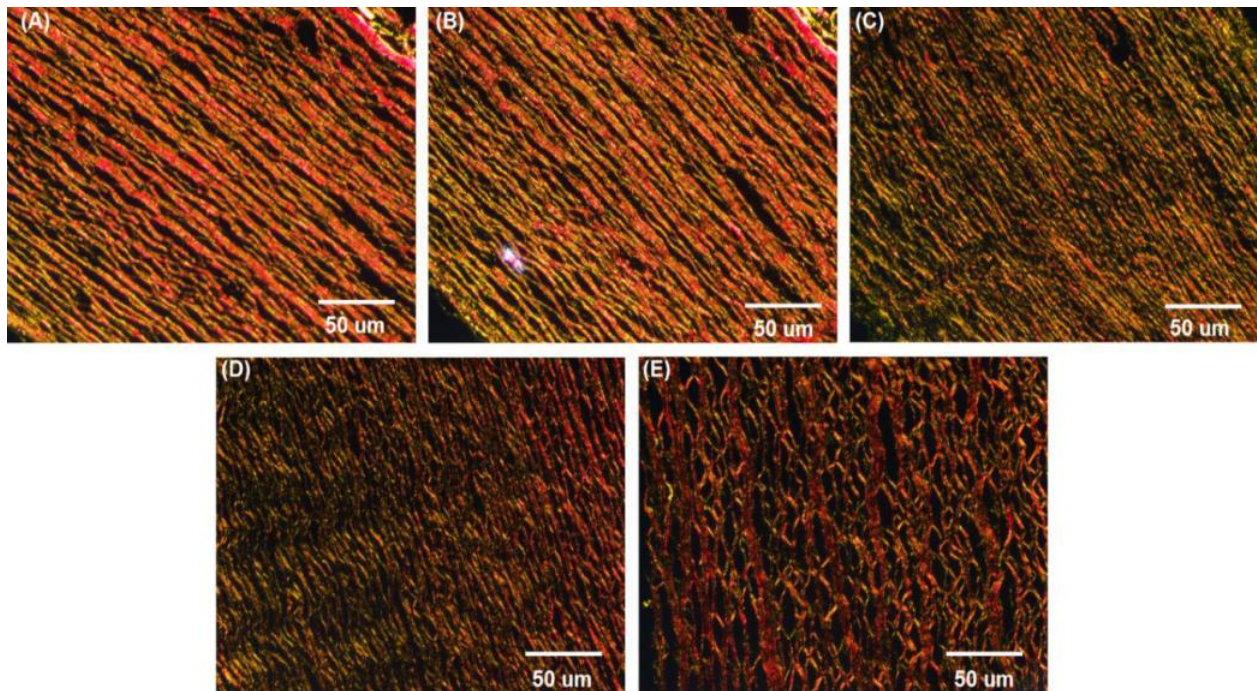


*Figure 74 picosirius red staining of collagen fibers for specimens in the circumferential orientation where (A) Healthy, (B) 4-hour (C) 8-hour (D) 12-hour and (E) 16-hour*

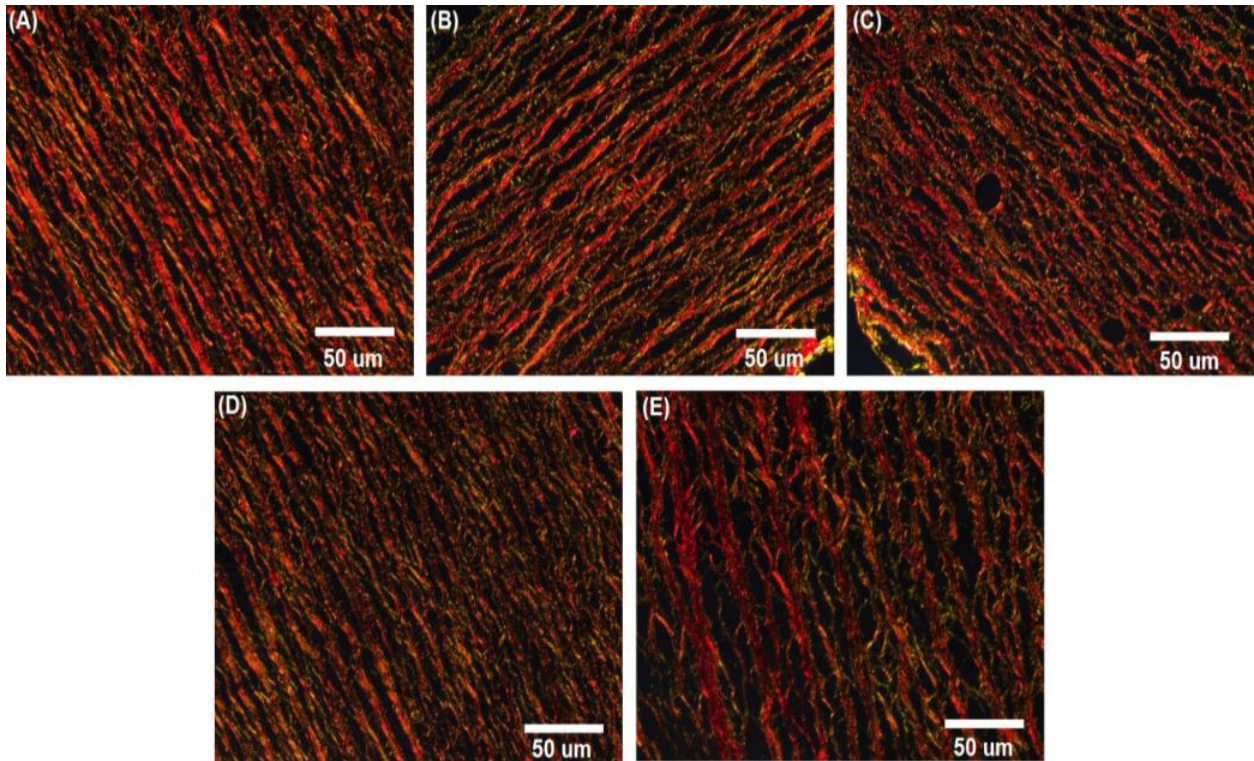


*Figure 75 picrosirius red staining of collagen fibers for specimens in the longitudinal orientation where (A) Healthy, (B) 4-hour (C) 8-hour (D) 12-hour and (E) 16-hour*

### **5.3. Collagen Fiber Fragmentation**

Using MATLAB, a code was developed in order to compute the relative reduction in volume fraction of red collagen fibers in healthy and collagen-degraded groups. After running the analysis in MATLAB, it was detected that collagenase did not affect fiber orientation; however, it did reduce the volume fraction of collagen-fiber content due to fragmentation. In addition, Gundiah et al. showed that collagen-fiber fragmentation occurs when collagenase is used which supports our findings [5].

Referring back to the strain-rate constitutive model results in chapter 4, the reduction in collagen-fiber volume fraction affected the aortic tissue by decreasing the overall tissue stiffness, which was validated through the change in stress-strain relationship and the PSR images that showed the reduction of mature collagen-fiber fraction and increased fragmentation. The reduction

fraction percentages of mature collagen fibers are shown in Table 8. It is essential to take into account that the calculated values shown in Table 8 do not reflect the exact amount of collagen content in the tissue due to the fact that collagen exhibits birefringence, which will cause certain fibers to appear under the microscope only when the slides are rotated to certain specific angles under the shined polarized light. Instead, the numbers reflect relative degradation values.

The primary goal of applying PSR technique was to examine the changes in the microstructural collagen-fiber network when comparing healthy and time-dependent Type-I collagen degradation specimens. Thus, when mounted on the microscope stage, the specimen slides were oriented at multiple angle, and images were captured. Images showing the most visible collagen fibers were chosen for the analysis.

*Table 8 The relative calculated percentage values of mature collagen-fiber reduction in tissue cross-section (n=6 for each one of the 5 groups)*

<b>Collagenase Immersion Time (in hours)</b>	<b>Type-I Relative Collagen Reduction Fraction in Circumferential Orientation (<math>\pm</math> Standard Deviation)</b>	<b>Type-I Relative Collagen Reduction Fraction in Longitudinal Orientation (<math>\pm</math> Standard Deviation)</b>
<b>0 hours (Control)</b>	100% $\pm$ 0%	100% $\pm$ 0%
<b>4 hours</b>	90.6% $\pm$ 5.6%	93.4% $\pm$ 5.1%
<b>8 hours</b>	73.2% $\pm$ 4.8%	93.1% $\pm$ 3.8%
<b>12 hours</b>	47.6% $\pm$ 5.8%	77.0% $\pm$ 3.2%
<b>16 hours</b>	46.2% $\pm$ 3.9%	72.8% $\pm$ 3.1%

#### **5.4. Discussion**

The macroscopic mechanical properties of the aortic tissue are governed by the intact state of the tissue's main components such as collagen. Collagen maintains the necessary cohesiveness



between other micro components in the aortic tissue such as elastin and smooth muscle [18, 41]. Thus, collagen fragmentation can result in destruction of the unity among the tissue components, which weakens the tissue and allows for rupture to become imminent.

As mentioned in chapters 1 and 2, the adventitia of the aortic tissue plays a critical role in maintaining a healthy state of the tissue and allows the tissue's wall to be flexible yet strong enough to prevent rupture and overstretching. Lindeman et al. suggests that the stress-strain behavior of intact arterial tissue is due to the different collagen architectures of the two layers, where the medial layer results in the flat linear phase of the curve and the adventitial layer results in transition to the non-linear phase of the curve [48]. Also, they concluded that alterations in the length of collagen fibers at the intrafibril, intrafiber, and suprafiber levels are associated with defects in AAA [48]. In addition, our findings indicate that collagen fragmentation does alter fiber length in addition to reducing volume fraction. Thus, impaired collagen fiber network behavior has a major contribution to mechanical failure of the aortic tissue.

As mentioned previously and according to Rizzo et al., Type-I collagen is the most abundant in the aortic tissue, which accounts for approximately 74% of all collagen types [9]. Thus, when comparing and linking the amount of Type-I collagen fiber volume by observing the PSR images in Figures 74 and 75, the numerical values presented in Table 8, and the stress-strain behavior discussed in chapter 4, we find that Type-I collagen degradation should be used as a biomechanical predictor in AAA rupture risk. Collagen degradation affects peak wall strength values and decreases tissue strength, which reduces the tissue's ability to withstand highly applied stress on the tissue's wall by the blood.

We can say that patients with hypertension who experience collagen degradation and fragmentation are at a higher risk of rupture due to developing weaker abdominal aortic tissue as

they age. This finding is supported by Urab et al. and Gundiah et al. who investigated fiber orientation in adventitial collagen [5, 49]. However, they did not consider the quantitative aspect of Type-I collagen volume fraction and relate it to changes in stress-strain behavior. Hope et al. referred to a study in which protein content was quantified using a “collagen-specific gadolinium-labeled lipid micelle” [55]. They reported a correlation between decreasing collagen and increasing rupture risk [55]. This confirms the work done by our lab in which we showed how collagenase exposure significantly weakens tissue in the abdominal aorta of porcine specimens.

The aortic tissue can be viewed as a matrix embedded with collagen fibers. The Fiber Elastic-Matrix Plastic theory states that in a matrix embedded with fibers of length ( $l$ ), fibers carry most of the load while the matrix carries a minimal amount of the load. According to the Fiber Elastic-Matrix Plastic theory, for a fiber to carry its maximum stress, its length has to be equal to or greater than the critical length of the fiber. The following equation relates fiber length to the breaking stress of the fiber:

$$\sigma_{fu} = 2\tau \frac{l_c}{d} \quad (5.1)$$

Where  $\sigma_{fu}$  is the maximum stress of the fiber,  $\tau$  is the shear stress at the fiber surface,  $l_c$  is the critical fiber length, and  $d$  is the diameter of the fiber.

The weakening of the aortic tissue is due to the fragmentation of collagen fibers by the action of collagenase. When collagen fibers are fragmented, their maximum load bearing ability decreases because the overall length of the fibers is shortened [56]. Thus, the tissue matrix will bear higher loads than its ability to withstand, and, as a result, will be more susceptible to rupture. Similarly, when collagen fragmentation occurs, collagen fibers are cleaved at specific amino acid ends causing the overall fiber lengths not only to lose critical length but also to fragment into many shorter fibers. Thus, the tissue’s ability to withstand high stresses will be lowered.

**Chapter 6**  
**Finite Element Analysis**

## 6.1. Methods

ABAQUS Finite Element Modeling Software was used in this study to conduct Finite Element Analysis on two models: healthy aortic tube model and time-dependent collagen degradation aortic tube model.

The healthy abdominal aorta was modeled as a cylindrical tube with the following dimensions: 14 cm long, 3 cm outer diameter, and 0.2 cm thick. The model was assigned an orthotropic elastic material behavior, and the assigned tissue property material values (shown in Tables 4-6) were derived from the experimental data. The geometry was meshed using C3D8 8-noded quad element mesh-type and has at least 20,000 elements, as shown in Figure 76. The boundary condition applied at each end of the tube model was pinned.

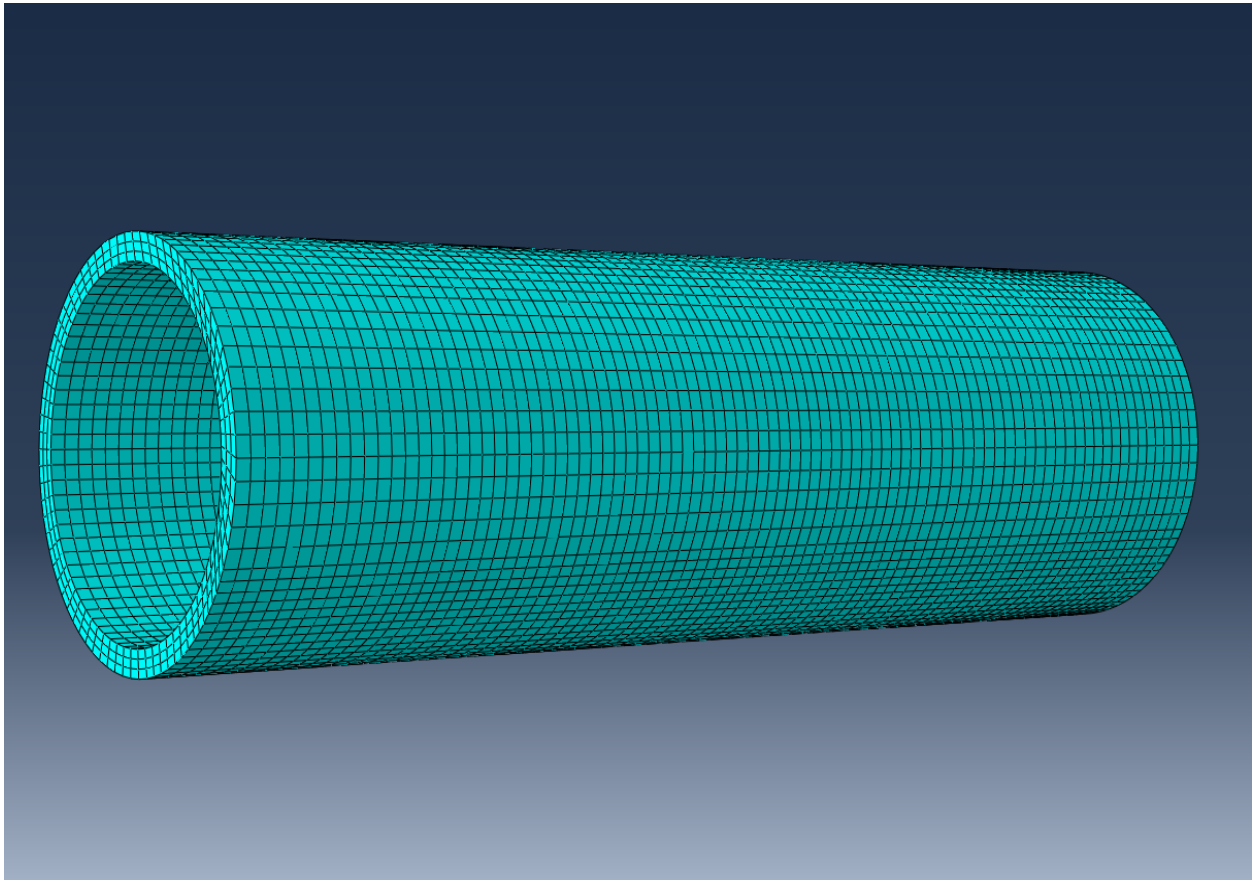


*Figure 76 Aortic tube model showing the meshed elements*

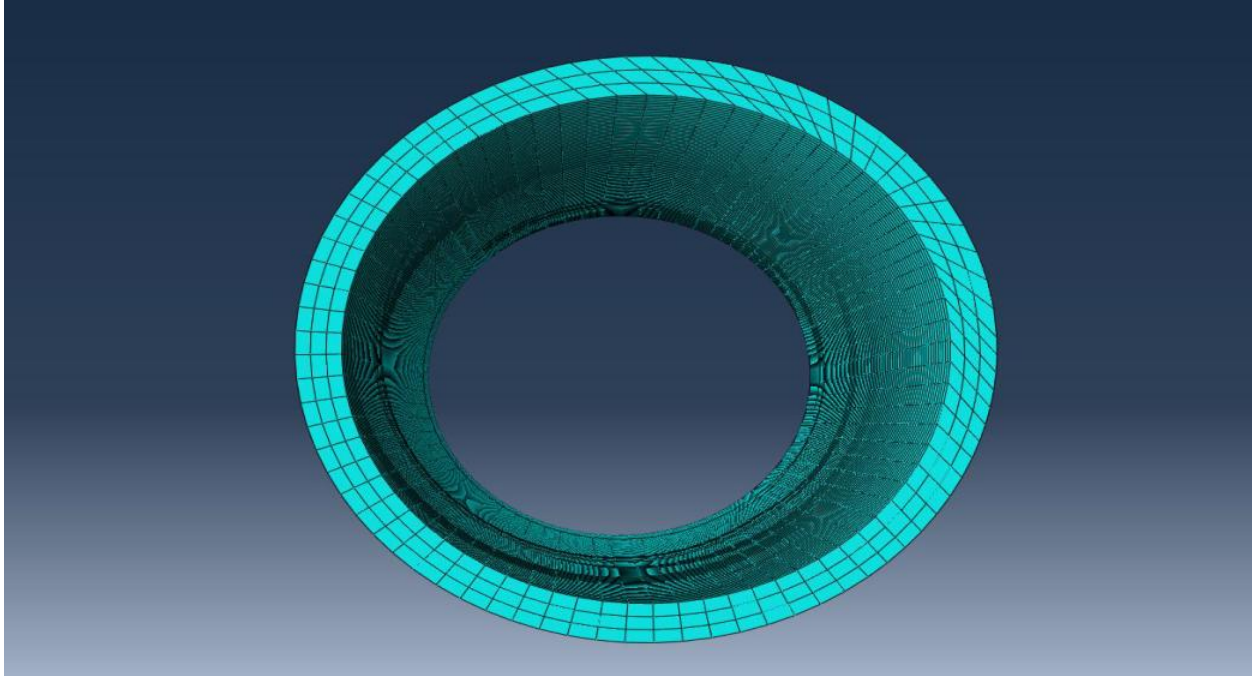


*Figure 77 Cross-sectional view of the aortic tube model*

The second model is the time-dependent collagen degradation aortic tube model which was created with the same exact geometry and dimensions of the healthy aortic model. However, in the aneurysmal model, the tube was partitioned into two halves. One half was assigned a healthy material property. The other half was partitioned into 9 sections, as shown in Figure 78.

Sections 1 and 9 were assigned healthy tissue material property, sections 2 and 8 were assigned 4-hour collagen degraded tissue property, sections 3 and 7 were assigned 8-hour collagen degraded tissue property, sections 4 and 6 were assigned 12-hour collagen degraded tissue property, and section 5 was assigned 16-hour collagen degraded tissue property. For both aortic models, an internal cyclic pressure load was applied. The pressure applied on the internal surface of the tube is a sinusoidal waveform that mimics the heart beat pattern, as shown in the following function  $f(t) = 12.5 + 3.5\sin(7.33 * t)$ .

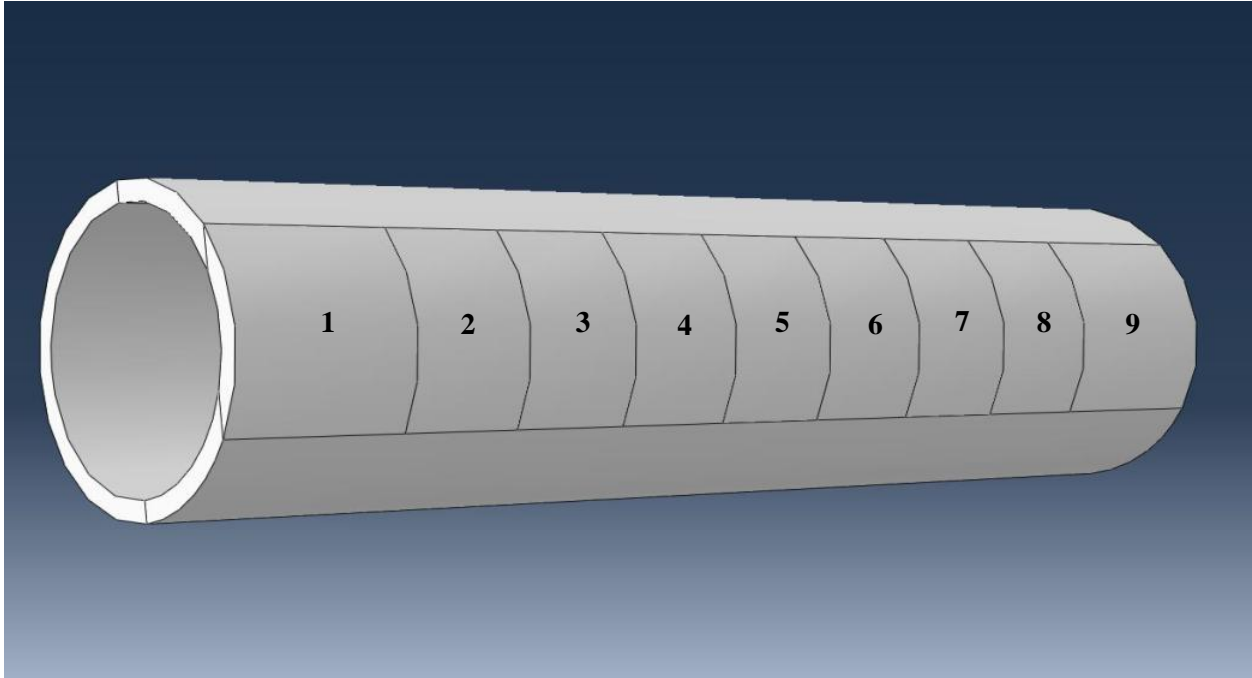


Figure 78 Section breakdown of time-dependent collagen degraded abdominal aortic model

## 6.2. Healthy Aortic Tube Model

The pulsing behavior of the healthy aortic model is shown in Figure 79 below. A uniform pressure mimicking heartbeat was applied.

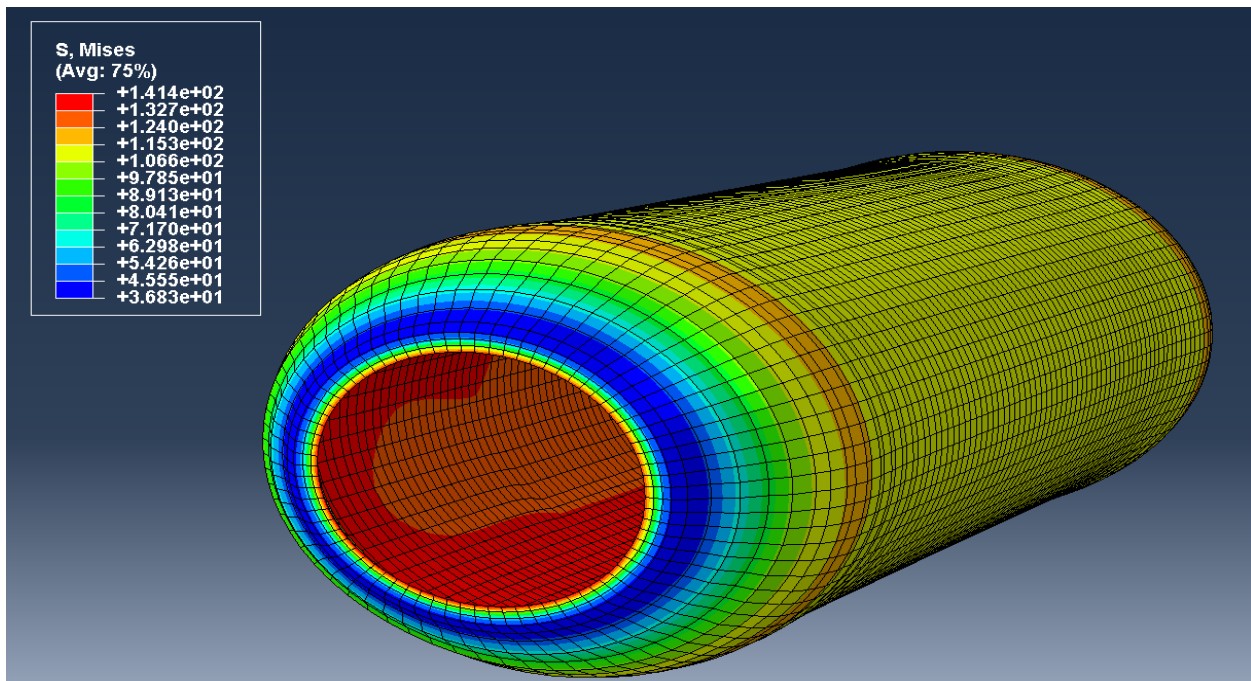
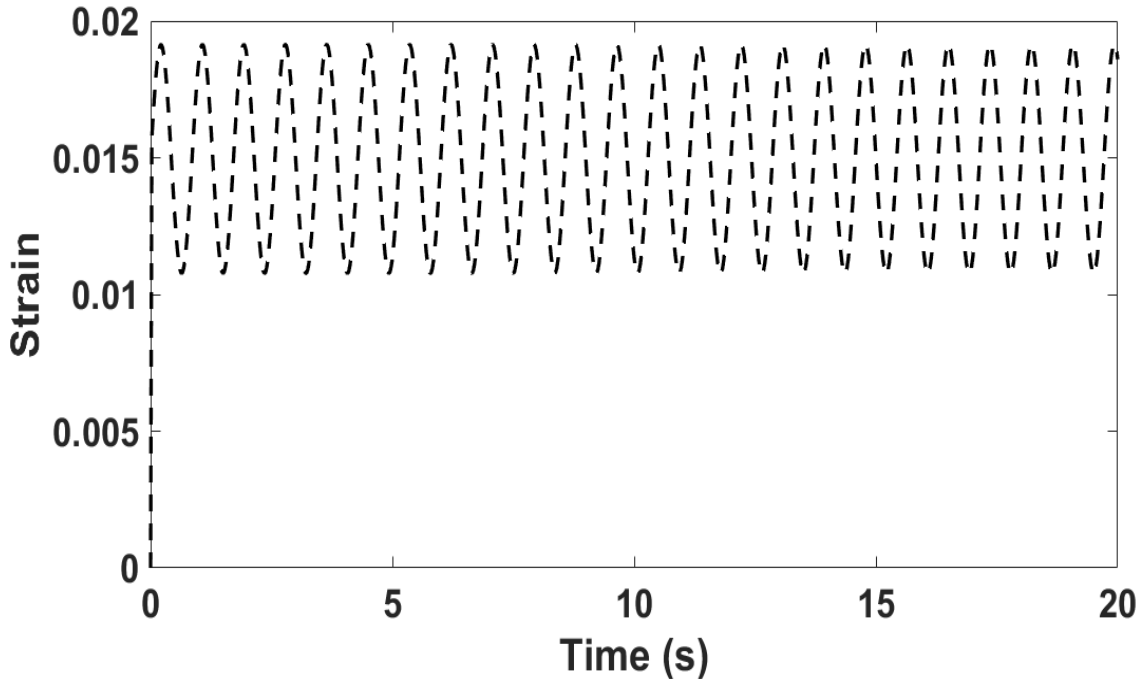
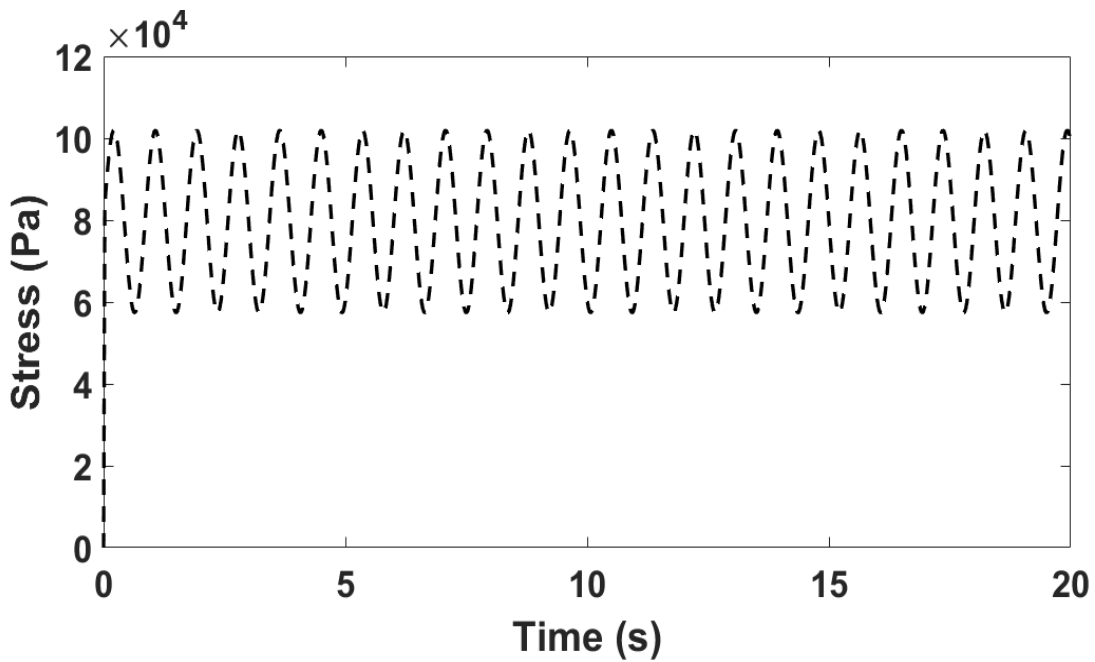


Figure 79 Deformed shape of pulsing behavior of healthy aorta subject to normal blood pressure wave

A single element was chosen from the healthy aortic tube model after completion of Finite Element Analysis to illustrate stress and circumferential strain magnitudes as a function of time, as shown in Figures 80 and 81.



*Figure 80 Strain vs time range based on cyclic blood pressure wave applied*



*Figure 81 Stress vs time range based on cyclic blood pressure wave applied*

### 6.3. Time-Dependent Collagen Degradation Aortic Model

The pulsing behavior of time-dependent collagen degradation aortic model is shown in Figure 82 below. A uniform pressure mimicking heartbeat was applied. The bulging of the wall in the model is due to the time-dependent collagen degradation tissue properties assigned. This model mimics aneurysmal growth from an initial stage based on changes in biomechanical tissue properties.

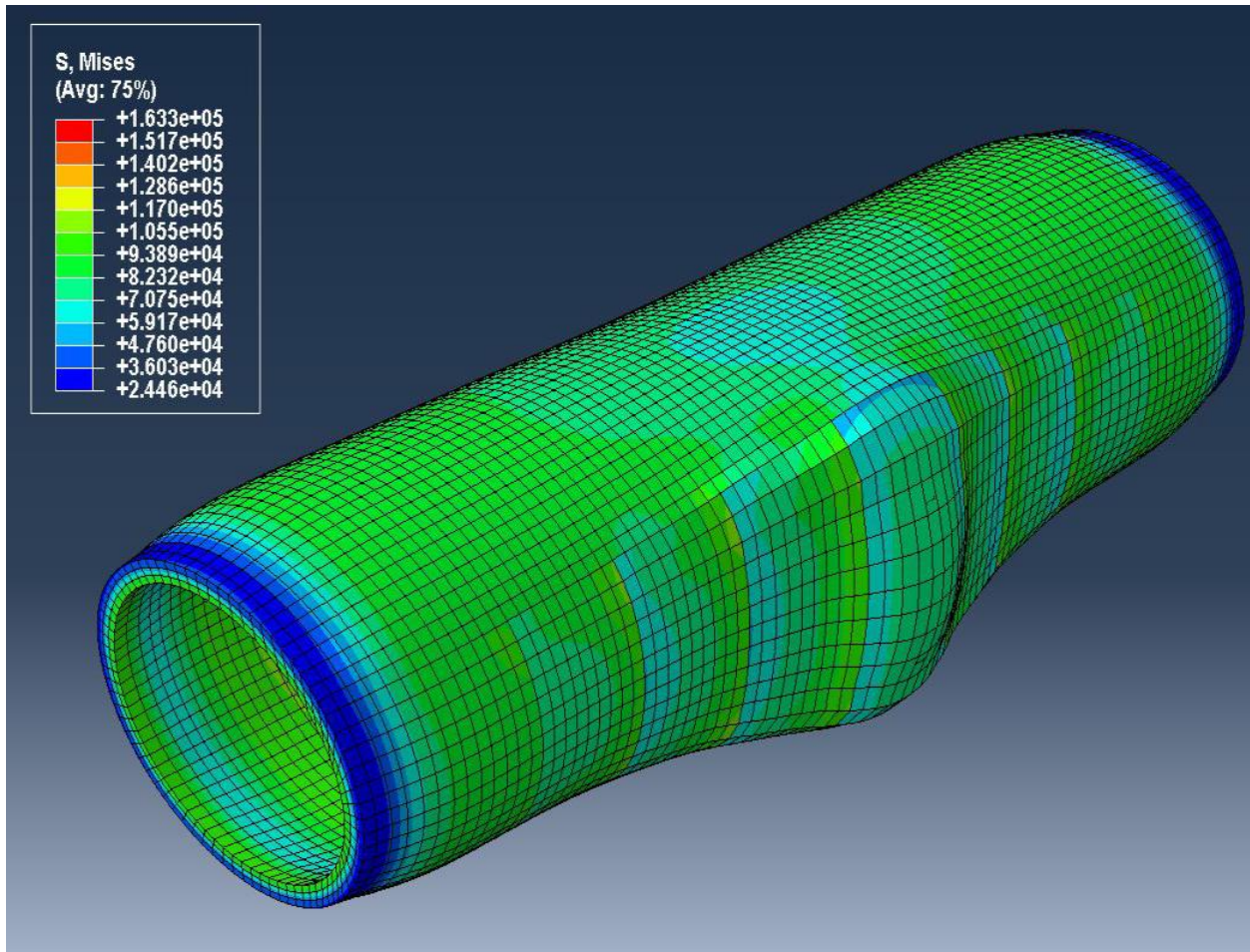


*Figure 82 Deformed shape due to pulsing behavior of the time-dependent collagen degraded aortic model*



A single element was chosen from each of the 9 sections in the time-dependent collagen degradation aortic tube model to demonstrate the change in stress and circumferential strain magnitudes as a function of time, as shown in Figures 83 and 84.

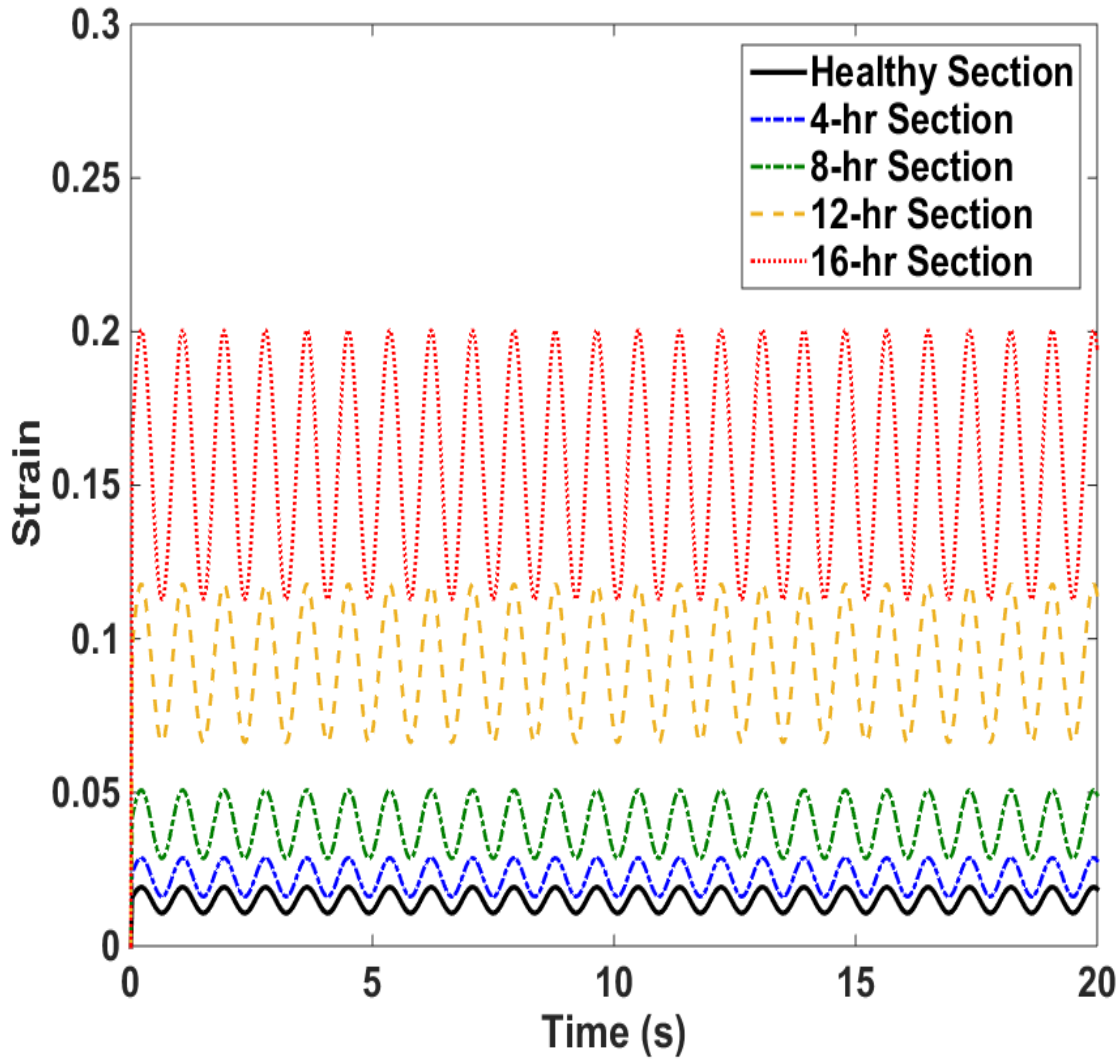


Figure 83 Strain vs time range based on cyclic blood pressure wave applied for elements chosen from all 9 sections in the time-dependent collagen degraded aortic model

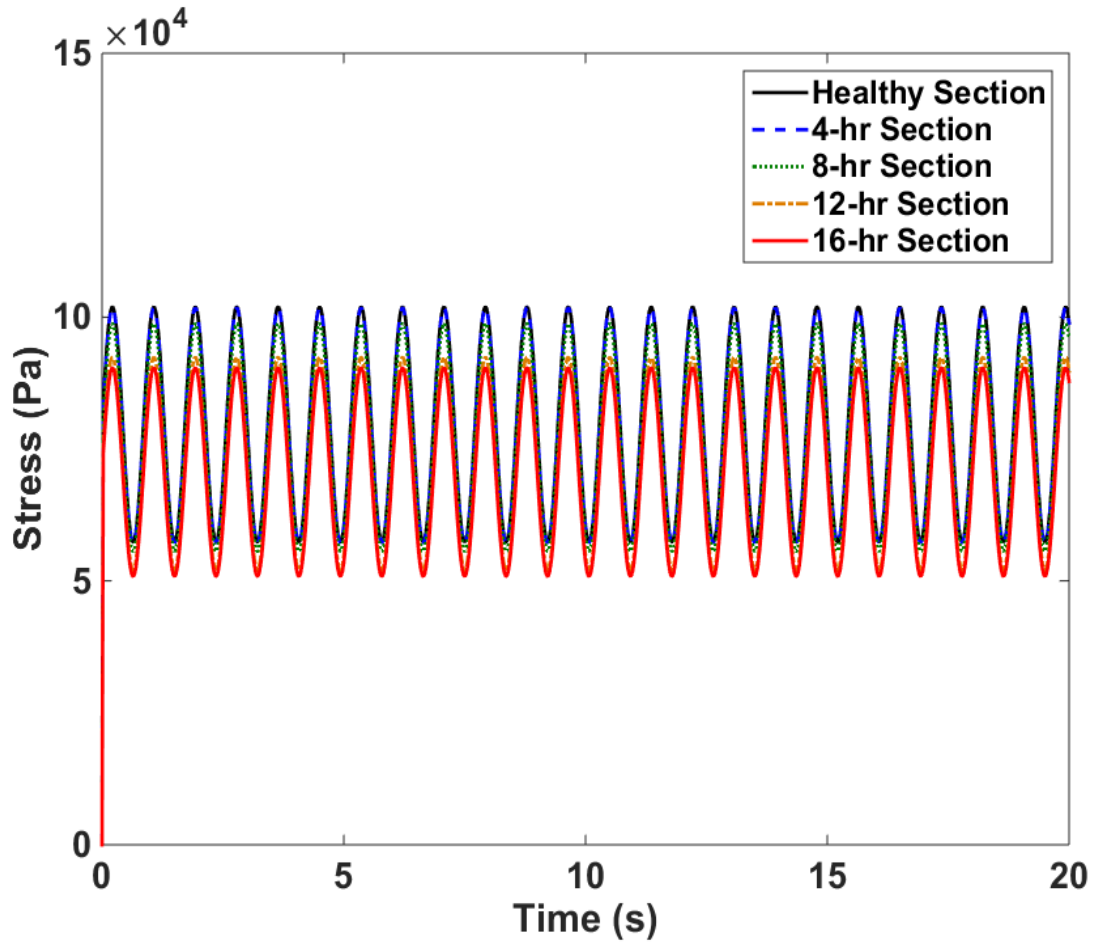


Figure 84 Stress vs time range based on cyclic blood pressure wave applied for elements chosen from all 9 sections in the time-dependent collagen degraded aortic model

#### 6.4. Discussion

Finite Element Analysis (FEA) of axisymmetric healthy aortic model tube in Figure 79 mimics the actual behavior of a healthy abdominal aorta in humans. FEA of time-dependent collagen degradation aortic tube model shows how aneurysm formation may happen due to lack of Type-I collagen remodeling in the tissue. Since stress is dependent on strain, the FEA indicates how strain, rather than stress, may be critically important in predicting where an aneurysm may rupture, because the strain values were different for all elements chosen from all 9 sections. On the other hand, the stress values for all elements chosen from all 9 sections were in close proximity.

An analysis of strain values from the time-dependent collagen degradation aortic model (Figure 83) shows that the circumferential wall strain values increase as Type-I collagen degradation occurs. The results show importance of Type-I collagen in maintaining tissue strength and preventing blood vessel rupture. The data also indicate that with adequate knowledge of tissue microstructure, a strain dependent approach can be used to predict rupture.

In addition, patients with hypertension, who develop abdominal aortic aneurysms, need to monitor the growth of the aneurysm more frequently due to the fact that an increase in wall stress along with collagen degradation will most likely result in a sooner vessel rupture.

Moreover, when comparing the maximum principal strain values for all chosen sections' elements in the time-dependent collagen degradation aortic tube in Figure 83, it can be seen that the maximum strains increased by the following approximate factors when compared to the healthy strain value: 2 times in the 4-hour collagen section, 3 times in the 8-hour collagen section, 6 times in the 12-hour collagen section, and 11 times in the 16-hour collagen section. Thus, these reported changes in strain values demonstrate that collagen presence in the tissue is vital in maintaining the structural integrity and necessary support to resist over-strain and over-stress that can result in tissue rupture.

Due to the focus on one variable (Type-I collagen in the tissue), normal blood pressure values, in the range of 80 mmHg to 130 mmHg, were applied in the model. No hypertension values were assigned to maintain the focus on Type-I collagen degradation. Thus, we are able to contribute to improving the accuracy of rupture prediction in a specific group of patients who suffer from Type-I collagen degradation due to genetics or age.

Incorporating biomechanical factors such as stress-strain relationships in aneurysms aids in evaluating the patient's case. It is essential to monitor and predict the status of the aneurysm

and be able to approximate the time to rupture as accurately as possible. Tissue stress-strain relationships allow us to predict potential rupture sites on an aneurysm because they can be used as a tool to determine aneurysmal regions that may be under high stress or strain.

One way to implement the use of a stress-strain biomechanical tool is through FEA of patient specific aneurysms. The aneurysmal geometry is reconstructed using CT scans, and tissue material properties are assigned. However, the analysis of rupture risk using FEA software may not be accurate if the tissue material parameters do not accurately mimic those of the patient's aneurysmal tissue properties. Thus, it is crucial to assign material properties that are very similar to the patient's actual tissue biomechanical behavior. Many studies conduct FEA of aneurysms under isotropic material property, but aortic tissue is not isotropic. It is reported to be anisotropic or at least orthotropic [45, 57].

This study applies orthotropic tissue material properties by utilizing the experimental data collected in order to better improve the FEA aspect of the problem, which will lead, ultimately, to more precise aneurysm monitoring, rupture site prediction, and time-to-rupture calculation.

The physiological stress applied on the aortic wall is multiaxial or, at least, biaxial. Conducting biaxial testing on aortic specimens helps us assign accurate tissue material properties when applying FEA. As a result, calculated critical stress-strain values will be accurate rupture criteria parameters. Also, biaxial tension tests allow us to implement constants that are closely related to the anisotropic biomechanical behavior of aortic tissue. Ultimately, more accurate finite element models and analysis of AAA is still needed, and, more importantly, the development of a universal reliable and consistent rupture risk assessment tool is crucial.

In addition, fluid-structure interaction between the blood and the aortic wall affects AAA growth as well as hypertension, as mentioned previously. Hypertension causes higher blood

pressure against the aortic wall and an increase in heart rate. As a result, blood velocity through the aorta increases due to the elevated heart rate. An increase in blood velocity will alter blood's laminar flow and establishes turbulent flow. Also, the presence of a bulge in the aorta alters the laminar blood flow and creates turbulent blood flow.

Studying fluid-structure flow of turbulent behavior is critical, because turbulent fluid-flow of blood allows for longer interaction time between the blood and tissue wall causing the formation of intraluminal thrombi on tissue wall. A thrombic mass is made up of fatty tissue and, with turbulent blood flow through the aneurysm, the blood will pick up small emboli and carry it downstream to the arterioles and venules. Consequently, blood clots and, eventually, strokes may occur. Thus, in future FEA, it is important to observe laminar vs. turbulent flow and how they affect the calculated biomechanical stress-strain values, and incorporate the fluid-structure interaction with the stress-strain analysis in one FEA study of rupture risk. This will contribute to developing a better prognostic tool [2, 8, 10].

Another biomechanical variable that requires attention is shear stress. Shear stress is affected by altering blood velocity and flow. Shear stress on the inside wall of the aorta increases with an increase in turbulent flow. Elevated shear stress will degrade the intima layer of the aortic wall faster, which destroys the structural integrity and weakens the aortic wall [12]. Thus, the shear stress biomechanical factor needs to be incorporated in the analysis and must be considered in future studies in order to improve the accuracy of rupture criteria [8]. Growth and rupture of AAA are driven by the changes in structure of the arterial wall. However, there is not a precise mechanism that shows how the process occurs [4, 10, 18]. For example, aneurysms with diameters smaller than 5.5 cm may still rupture. It is essential to develop a more precise and accurate rupture

risk criterion that will be used in the development of a prognostic tool that will aid in predicting growth and rupture [3, 4, 29, 58].

**Chapter 6**  
**Limitations**

The kinetics of AAA growth were not modeled in this study based on results obtained from human aneurysmal aortas. Five-month old pig aortas cannot be directly compared to 60-year old human aortas. A relationship between porcine tissue and human tissue needs to be established. Such relationship will account for the unique properties of each tissue. This will be the focus of future studies.

It is important to take into account that aneurysmal development may be preceded by elastin fragmentation, a phenomenon that would likely alter the mechanical properties of the tissue as well. Also, the collagenase utilized does not perfectly imitate in-vivo AAA initiation and growth. Other MMPs and inflammatory proteins are involved in the process, and they degrade collagen and elastin at a different rate. In addition, elastin and all other components of the ECM were intact in these specimens. Even if collagen content was the single most important predictor of aneurysmal rupture, as of now, we do not have a methodology that assesses collagen content in vivo. However, we have many imaging techniques to look at the shape, size, thrombus, calcification, and metabolic activity in an aneurysm.

Biaxial testing data were utilized to calculate and quantify tissue properties in order to apply orthotropic material property assumption in our FEM. However, the aortic tissue is anisotropic in nature. Thus, it is important to account for anisotropic material properties in order to improve upon the accuracy of FEM. Improving the accuracy of FEM will allow for better prediction of rupture sites in the aortic wall.

Many variables are involved in the pathophysiology of AAA. Variables such as aortic diameter, ILT growth, ILT volume, fluid-structure interaction, wall shear stress, elastin, collagen, and smooth muscle degradation, as well as gender, play a vital role in assessing rupture risk in an aneurysm. This study focused on one aspect of the complex pathophysiology of AAA. Given that



collagen is the main protein that supports the tissue's structural integrity at higher stresses, this work will aid in contributing to the ongoing work on predicting rupture of AAA.

## **Chapter 7**

### **Conclusion**

From the results of this study, it can be concluded that an aneurysmal tissue experiences significant changes in its biomechanical properties. When observing alterations in tissue's Type-I collagen microstructure due to time-dependent degradation, the results indicate that critical strain to rupture will be a better indicator for predicting rupture in AAA rather than solely relying on the maximum diameter criteria.

AAA has many risk factors such as smoking, hypertension, gender, and genetics. In fact, the pathogenesis of AAA is not fully dependent on biomechanics. Accurate assessment of AAA relies on the combination of biomechanics, genetics, and external causes or behavior. However, the biomechanics contribute to a big portion of the problem. Thus, the biomechanical behavior, which encompasses stress-strain relationships and fluid-structure interactions, can contribute significantly to answering many questions regarding the growth and rupture prediction of AAA. So, new insights will be provided to the overall solution of AAA pathogenesis.

A variety of studies have conducted significant new research in modeling of AAA and predicting rupture. Technological advancements have been utilized to create many new innovative techniques. Such techniques have facilitated better assessment of rupture risk in AAA patients. Thus, those techniques have allowed for incorporation of factors used to predict rupture in AAA such as gender, age, family history, smoking status, hypertension, aneurysm size, aneurysm diameter, and intraluminal thrombus thickness in the models assessing the risk of rupture [3, 8, 24].

Nonetheless, so far, the maximum diameter is the main rupture criteria used to assess rupture risk in AAA. This study is devoted to the development of a new approach to better predicting rupture in AAA. Moreover, the need for a precise and consistent stress-strain analysis

of AAA is still necessary. It will allow us to reconstruct a three-dimensional solid model and assign more accurate material properties to the model.

Our study elucidates the effect of time-dependent Type-I collagen degradation in AAA rupture prediction and how it can be applied as an accurate biomechanical rupture criterion that considers the aortic tissue's microstructure. Collagenases, a class of protease enzymes, degrade collagen by cleaving specific amino acids. Neutrophil collagenase and cysteine collagenase K, L, and S are collagenases that are usually active in growing and ruptured AAAs [26]. Excessive collagenase activity in media and adventitia layers of the aortic wall results in a destruction of the aortic wall's microstructural integrity and stability [26]. This study investigated the effect on biomechanical relationship of the aortic tissue due to time-dependent Type-I collagen degradation in the tissue. To our knowledge, this study is the first to examine the biomechanical behavior of the aortic tissue of time-dependent degradation of Type-I collagen paired with quantified reduction in Type-I collagen in specimens and applied orthotropic tissue material properties in the FEA.

In the literature, the aortic tissue properties have been reported as being fully anisotropic. One of our previous studies has shown how tissue elasticity, in the longitudinal and circumferential orientations, differs, implying, at least, an orthotropic material property and justifying our assumption of orthotropic behavior in the ABAQUS model. So, our current study has applied an orthotropic material property in the FEA models.

Although assumptions such as orthotropic are not fully accurate in estimation of stress-strain values, the results are still significant when compared to other FEA models in the literature. To our knowledge, this is the first work to divide the aortic tube model into many sections, and assign each section a different tissue property based on experimental values obtained from healthy and time-dependent Type-I collagen degraded biaxial testing. From FEA results shown in Figure

82, It is shown that an aneurysm gradually forms in the tissue region where time-dependent collagen degradation material properties are present, and the potential rupture site is more likely to happen in those regions where structural integrity of the tissue is weakened.

In the literature, many studies performed AAA modeling via conducting finite element analysis on aneurysm constructed geometry from patients' CT scans and analyzed the stress on the scanned aneurysm. This study aimed to contribute to further prediction of future behavior of aneurysmal growth by observing the growth of AAA from an initial stage.

In future studies, the focus on accuracy of the existing biomechanical FEA models will be improved by obtaining more data through intensive testing of abdominal aortic tissue based on degradation of elastin and different proteins that contribute to the structural integrity of the aortic tissue. Conducting various models of fluid-structure interaction in an aneurysm, observing the effects of intraluminal thrombus on peak wall stress, and incorporating shear stress need to be considered in evaluating rupture assessment of AAA [2, 8, 10, 58].

## References

1. Raghavan, M.L., *Cardiovascular Bio-solid Mechanics Section*. p. 3-25.
2. Zelaya, J.E., Goenezen, S., Dargon, P. T., Azarbal, A., & Rugonyi, S., *Improving the efficiency of abdominal aortic aneurysm wall stress computations*. Plos One, 2014. **9**(7).
3. Vorp, D.A., & Vande Geest, J. P., *Biomechanical determinants of abdominal aortic aneurysm rupture*. Arteriosclerosis, Thrombosis, And Vascular Biology, 2005. **25**(8): p. 1558-1566.
4. Vorp, D.A., Raghavan, M. L., & Webster, M. W., *Mechanical wall stress in abdominal aortic aneurysm: influence of diameter and asymmetry*. Journal Of Vascular Surgery, 1998. **27**(4): p. 632-639.
5. Gundiah, N., Babu, A. R., & Pruitt, L. A., *Effects of elastase and collagenase on the nonlinearity and anisotropy of porcine aorta*. Physiological Measurement, 2013. **34**(12): p. 1657-1673.
6. Shang, E.K., Nathan, D. P., Woo, E. Y., Fairman, R. M., Wang, G. J., Gorman, R. C., & ... Jackson, B. M., *Local wall thickness in finite element models improves prediction of abdominal aortic aneurysm growth*. Journal Of Vascular Surgery, 2015. **61**(1): p. 217-223.
7. Vande Geest, J.P., Di Martino, E. S., Bohra, A., Makaroun, M. S., & Vorp, D. A., *A biomechanics-based rupture potential index for abdominal aortic aneurysm risk assessment: demonstrative application*. Annals Of The New York Academy Of Sciences, 2006. **1085**: p. 11-21.
8. Jacopo Biasetti, P.G.S., Jesper Swedenborg, and T. Christian Gasser, *An integrated fluid-chemical model toward modeling the formation of intra-luminal thrombus in abdominal aortic aneurysms*. Front. Physiol, 2012. **3**: p. 266.
9. Rizzo, R.J., McCarthy, W. J., Dixit, S. N., Lilly, M. P., Shively, V. P., Flinn, W. R., & Yao, J. S., *Collagen types and matrix protein content in human abdominal aortic aneurysms*. Journal Of Vascular Surgery, 1989. **10**(4): p. 365-373.
10. Mower, W.R., Quiñones, W. J., & Gambhir, S. S, *Effect of intraluminal thrombus on abdominal aortic aneurysm wall stress*. Journal Of Vascular Surgery, 1997. **26**(4): p. 602-608.
11. Metaxa, E., Kontopodis, N., Vavourakis, V., Tzirakis, K., Ioannou, C. V., & Papaharilaou, Y., *The influence of intraluminal thrombus on noninvasive abdominal aortic aneurysm wall distensibility measurement*. Medical & Biological Engineering & Computing, 2015. **53**(4): p. 299-308.

12. Boyd, A.J., Kuhn, D. S., Lozowy, R. J., & Kulbisky, G. P., *Low wall shear stress predominates at sites of abdominal aortic aneurysm rupture*. Journal Of Vascular Surgery, 2016. **63**(6): p. 1613-1619.
13. Khan, S., Verma, V., Verma, S., Polzer, S., & Jha, S., *Assessing the potential risk of rupture of abdominal aortic aneurysms*. Clinical Radiology, 2015. **70**(1): p. 11-20.
14. Julia Brangsch, C.R., Federico Colletini, Ralf Buchert, René M. Botnar, Marcus R. Makowski, *Molecular Imaging of Abdominal Aortic Aneurysms*. Cell, 2017. **23**(2): p. 150-164.
15. Wilson, K.A., Lindholt, J. S., Hoskins, P. R., Heickendorff, L., Vammen, S., & Bradbury, A. W., *The relationship between abdominal aortic aneurysm distensibility and serum markers of elastin and collagen metabolism*. European Journal Of Vascular And Endovascular Surgery: The Official Journal Of The European Society For Vascular Surgery, 2001. **21**(2): p. 175-178.
16. Gasser, T.C., Auer, M., Labruto, F., Swedenborg, J., & Roy, J., *Biomechanical rupture risk assessment of abdominal aortic aneurysms: model complexity versus predictability of finite element simulations*. European Journal Of Vascular And Endovascular Surgery: The Official Journal Of The European Society For Vascular Surgery, 2010. **40**(2): p. 176-185.
17. Tong, J., Cohnert, T., Regitnig, P., & Holzapfel, G. A., *Effects of age on the elastic properties of the intraluminal thrombus and the thrombus-covered wall in abdominal aortic aneurysms: biaxial extension behaviour and material modelling*. European Journal Of Vascular And Endovascular Surgery: The Official Journal Of The European Society For Vascular Surgery, 2011. **42**(2): p. 207-219.
18. Choke, E., Cockerill, G., Wilson, W. W., Sayed, S., Dawson, J., Loftus, I., & Thompson, M. M., *A review of biological factors implicated in abdominal aortic aneurysm rupture*. European Journal Of Vascular And Endovascular Surgery: The Official Journal Of The European Society For Vascular Surgery, 2005. **30**(3): p. 227-244.
19. Tong, J., Schriefl, A. J., Cohnert, T., & Holzapfel, G. A., *Gender differences in biomechanical properties, thrombus age, mass fraction and clinical factors of abdominal aortic aneurysms*. European Journal Of Vascular And Endovascular Surgery: The Official Journal Of The European Society For Vascular Surgery, 2013. **45**(4): p. 364-372.
20. Raghavan, M.L., Webster, M. W., & Vorp, D. A., *Ex vivo biomechanical behavior of abdominal aortic aneurysm: assessment using a new mathematical model*. Annals Of Biomedical Engineering, 1996. **24**(5): p. 573-582.
21. Wilson, K.A., Lee, A. J., Lee, A. J., Hoskins, P. R., Fowkes, F. R., Ruckley, C. V., & Bradbury, A. W., *The relationship between aortic wall distensibility and rupture of*

- infrarenal abdominal aortic aneurysm*. Journal Of Vascular Surgery, 2003. **37**(1): p. 112-117.
22. Alfaori, Q., *Rupture in Abdominal Aortic Aneurysm*, in *Biomedical Engineering*. 2015, University of Arkansas: Fayetteville. p. 79.
  23. *The Top 10 Causes of Death*. 2012.
  24. Doyle, B.J., *3D Imaging of abdominal aortic aneurysms techniques and applications*. 2010: Hauppauge, N.Y.: Nova Science.
  25. Greenhalgh, R.M., Brown, L. C., & Powell, J. T., *Endovascular Repair of Abdominal Aortic Aneurysm*. New England Journal Of Medicine, 2010. **363**(15): p. 1479.
  26. Abdul-Hussien, H., Soekhoe, R. V., Weber, E., von der Thüsen, J. H., Kleemann, R., Mulder, A., & Lindeman, J. N., *Collagen degradation in the abdominal aneurysm: a conspiracy of matrix metalloproteinase and cysteine collagenases*. The American Journal Of Pathology, 2007. **170**(3): p. 809-817.
  27. Humphrey, J.D., & Taylor, C. A., *Intracranial and Abdominal Aortic Aneurysms: Similarities, Differences, and Need for a New Class of Computational Models*. Annual Review Of Biomedical Engineering, 2008. **10**(1): p. 221-246.
  28. Aggarwal Sourabh, Q.A., Sharma Vishal, Sharma Alka *Abdominal aortic aneurysm: A comprehensive review*. Exp Clin Cardiol, 2011. **16**(1).
  29. Wilson, C., *Abaqus Abdominal Aortic Aneurysm Model*. In NONLINEAR FINITE ELEMENT ANALYSIS OF AN ABDOMINAL AORTIC ANEURYSM, 2008.
  30. Thompson, R.W., Curci, J. A., Ennis, T. L., Mao, D., Pagano, M. B., & Pham, C. N., *Pathophysiology of abdominal aortic aneurysms: insights from the elastase-induced model in mice with different genetic backgrounds*. Annals Of The New York Academy Of Sciences, 2006. **1085**: p. 59-73.
  31. Tsamis A, K.J., Vorp DA., *Elastin and collagen fibre microstructure of the human aorta in ageing and disease: a review*. 2013.
  32. Wilmink, T.B., Quick, C. R., & Day, N. E., *The association between cigarette smoking and abdominal aortic aneurysms*. Journal Of Vascular Surgery, 1999. **30**(6): p. 1099-1105.
  33. Lindeman, J.N., *The pathophysiologic basis of abdominal aortic aneurysm progression: a critical appraisal*. Expert Review Of Cardiovascular Therapy, 2015. **13**(7): p. 839-851.



34. Wanhainen, A., Mani, K., & Golledge, J., *Surrogate Markers of Abdominal Aortic Aneurysm Progression*. *Arteriosclerosis, Thrombosis, And Vascular Biology*, 2016. **36**(2): p. 236-244.
35. Kuivaniemi, H., Ryer, E. J., Elmore, J. R., & Tromp, G., *Understanding the pathogenesis of abdominal aortic aneurysms*. *Expert Review Of Cardiovascular Therapy*, 2015. **13**(9): p. 975-987.
36. A. Abbas, R.A., A. Smith and M. Waltham, *Can We Predict Abdominal Aortic Aneurysm (AAA) Progression and Rupture by Non-Invasive Imaging?—A Systematic Review*. *International Journal of Clinical Medicine*, 2011. **2**(4): p. 484-499.
37. Wilson, K., Bradbury, A., Whyman, M., Hoskins, P., Lee, A., Fowkes, G., & ... Ruckley, C. V., *Relationship between abdominal aortic aneurysm wall compliance and clinical outcome: a preliminary analysis*. *European Journal Of Vascular And Endovascular Surgery: The Official Journal Of The European Society For Vascular Surgery*, 1998. **15**(6): p. 472-477.
38. Gasser, T.C., Nchimi, A., Swedenborg, J., Roy, J., Sakalihasan, N., Böckler, D., & Hyhlik-Dürr, A, *A novel strategy to translate the biomechanical rupture risk of abdominal aortic aneurysms to their equivalent diameter risk: method and retrospective validation*. *European Journal Of Vascular And Endovascular Surgery: The Official Journal Of The European Society For Vascular Surgery*, 2014. **47**(3): p. 288-295.
39. Sonesson, B., Sandgren, T., & Länne, T., *Abdominal aortic aneurysm wall mechanics and their relation to risk of rupture*. *European Journal Of Vascular And Endovascular Surgery: The Official Journal Of The European Society For Vascular Surgery*, 1999. **18**(6): p. 487-93.
40. Molacek, J., Baxa, J., Houdek, K., Treska, V., & Ferda, J., *Assessment of abdominal aortic aneurysm wall distensibility with electrocardiography-gated computed tomography*. *Annals Of Vascular Surgery*, 2011. **25**(8): p. 1036-1042.
41. Martufi, G., Auer, M., Roy, J., Swedenborg, J., Sakalihasan, N., Panuccio, G., & Gasser, T. C., *Multidimensional growth measurements of abdominal aortic aneurysms*. *Journal Of Vascular Surgery*, 2013. **58**(3): p. 748-755.
42. Li, Z., & Kleinstreuer, C., *Effects of blood flow and vessel geometry on wall stress and rupture risk of abdominal aortic aneurysms*. *Journal Of Medical Engineering & Technology*, 2006. **30**(5): p. 283-297.
43. Larsson, E., Labruto, F., Gasser, T. C., Swedenborg, J., & Hultgren, R., *Analysis of aortic wall stress and rupture risk in patients with abdominal aortic aneurysm with a gender perspective*. *Journal Of Vascular Surgery*, 2011. **54**(2): p. 295-299.

44. Tanios, F., Gee, M. W., Pelisek, J., Kehl, S., Biehler, J., Grabher-Meier, V., & ... Reeps, C., *Interaction of biomechanics with extracellular matrix components in abdominal aortic aneurysm wall*. European Journal Of Vascular And Endovascular Surgery: The Official Journal Of The European Society For Vascular Surgery, 2015. **50**(2): p. 167-174.
45. Vorp, D.A., *Biomechanics of abdominal aortic aneurysm*. Journal Of Biomechanics, 2007. **40**(9): p. 1887-1902.
46. Wilson, J.S., Virag, L., Di Achille, P., Karsaj, I., & Humphrey, J. D., *Biochemomechanics of intraluminal thrombus in abdominal aortic aneurysms*. Journal Of Biomechanical Engineering, 2013. **135**(2).
47. Rao, J., Brown, B. N., Weinbaum, J. S., Ofstun, E. L., Makaroun, M. S., Humphrey, J. D., & Vorp, D. A., *Distinct macrophage phenotype and collagen organization within the intraluminal thrombus of abdominal aortic aneurysm*. Journal Of Vascular Surgery, 2015. **62**(3): p. 585-593.
48. Lindeman, J.H.N., Brian A. Ashcroft, Jan-Willem M. Beenakker, Maarten van Es, Nico B. R. Koekkoek, and J.F.T. Frans A. Prins, Hazem Abdul-Hussien, Ruud A. Bank, and Tjerk H. Oosterkamp, *Distinct defects in collagen microarchitecture underlie vessel-wall failure in advanced abdominal aneurysms and aneurysms in Marfan syndrome*. 2009.
49. Urabe, G., Hoshina, K., Shimanuki, T., Nishimori, Y., Miyata, T., & Deguchi, J., *Structural analysis of adventitial collagen to feature aging and aneurysm formation in human aorta*. Journal Of Vascular Surgery, 2015. **63**(5): p. 1341-1350.
50. Carmo, M., Colombo, L., Bruno, A., Corsi, F. M., Roncoroni, L., Cuttin, M. S., & ... Settembrini, P. G., *Alteration of elastin, collagen and their cross-links in abdominal aortic aneurysms*. European Journal Of Vascular And Endovascular Surgery: The Official Journal Of The European Society For Vascular Surgery, 2002. **23**(6): p. 543-549.
51. Canchi, T., Kumar, S. D., Ng, E. K., & Narayanan, S., *A Review of Computational Methods to Predict the Risk of Rupture of Abdominal Aortic Aneurysms*. Biomed Research International, 2015: p. 1-12.
52. Kural, M.H., Cai, M., Tang, D., Gwyther, T., Zheng, J., & Billiar, K. L., *Planar biaxial characterization of diseased human coronary and carotid arteries for computational modeling*. Journal Of Biomechanics, 2011. **45**(5): p. 790-798.
53. Kivikari, J., *Influence of Elastase and Collagenase: ex vivo study on the mechanical properties of porcine aorta by biaxial tensile tests*. 2015. p. 45.
54. Vogel, B., Siebert, H., Hofmann, U., & Frantz, S., *Determination of collagen content within picosirius red stained paraffin-embedded tissue sections using fluorescence microscopy*. Methodsx, 2015: p. 2124-134.

55. Hope, T.A., & Hope, M. D., *Improved risk assessment for abdominal aortic aneurysm rupture: off-the-wall imaging*. Journal Of The American College Of Cardiology, 2011. **58**(24): p. 2531-2532.
56. Chawla, K.K., *Composite Materials Science and Engineering*. 1987: Springer-Verlag New York Inc.
57. Raghavan, M.L., & Vorp, D. A., *Toward a biomechanical tool to evaluate rupture potential of abdominal aortic aneurysm: identification of a finite strain constitutive model and evaluation of its applicability*. Journal Of Biomechanics, 2000. **33**(4): p. 475-482.
58. Polzer, S., Gasser, T. C., Bursa, J., Staffa, R., Vlachovsky, R., Man, V., & Skacel, P., *Importance of material model in wall stress prediction in abdominal aortic aneurysms*. Medical Engineering & Physics, 2013. **35**(9): p. 1282-1289.